2001

Studies of subdwarf B stars

Michael David Reed
Iowa State University

INFORMATION TO USERS

This manuscript has been reproduced from the microfilm master. UMI films the text directly from the original or copy submitted. Thus, some thesis and dissertation copies are in typewriter face, while others may be from any type of computer printer.

The quality of this reproduction is dependent upon the quality of the copy submitted. Broken or indistinct print, colored or poor quality illustrations and photographs, print bleedthrough, substandard margins, and improper alignment can adversely affect reproduction.

In the unlikely event that the author did not send UMI a complete manuscript and there are missing pages, these will be noted. Also, if unauthorized copyright material had to be removed, a note will indicate the deletion.

Oversize materials (e.g., maps, drawings, charts) are reproduced by sectioning the original, beginning at the upper left-hand corner and continuing from left to right in equal sections with small overlaps.

Photographs included in the original manuscript have been reproduced xerographically in this copy. Higher quality 6" x 9" black and white photographic prints are available for any photographs or illustrations appearing in this copy for an additional charge. Contact UMI directly to order.

ProQuest Information and Learning
300 North Zeeb Road, Ann Arbor, MI 48106-1346 USA
800-521-0600

UMI®

Studies of Subdwarf B Stars

by

Michael David Reed

A dissertation submitted to the graduate faculty

in partial fulfillment of the requirements for the degree of

DOCTOR OF PHILOSOPHY

Major: Astrophysics

Program of Study Committee:
Steven D. Kawaler, Major Professor
Scot J. Kleinman
Russell J. Lavery
Curt Struck
Hal Stern
Paul Canfield

Iowa State University

Ames, Iowa

2001

ProQuest Information and Learning Company
300 North Zeeb Road
P.O. Box 1346
Ann Arbor, MI 48106-1346

Graduate College
Iowa State University

This is to certify that the doctoral dissertation of

Michael David Reed

has met the dissertation requirements of Iowa State University

Signature was redacted for privacy.

Major Professor

Signature was redacted for privacy.

For the Major Program

TABLE OF CONTENTS

LIST OF TABLES

LIST OF FIGURES

ABSTRACT

Subdwarf B (sdB) stars are on the extreme end of the horizontal branch. They have extremely thin hydrogen (H) envelopes surrounding an approximately half solar mass ($\sim 0.5 M_{\odot}$) core. Subdwarf B stars are the most common objects detected in color selected sky surveys yet very little is known about their origin or evolution. Following their classification in 1966 by Greenstein, very little progress was made in understanding these apparently common stars. Saffer *et al.* (1994) better defined the class and when pulsators were discovered by Kilkenny *et al.* (1997), it became plausible that we could explore their interiors through asteroseismology.

We concentrate on four stars for which we have acquired sufficient data to resolve the temporal spectra. Our study of these four stars (and sdBV stars as an ensemble), relying on standard stellar models and asteroseismology tools, has produced some new results and pinpointed wide gaps in our understanding of these stars.

We are able to identify specific pulsation modes in the coolest sdBV star, Feige 48. We then match these modes to a stellar model. We also confirm the work of Kawaler (1999) and his model match for PG 1605. We placed firm upper limits on $\dot{\mathrm{P}}/\mathrm{P}$ for an sdBV star (Feige 48), finding a lower limit to the evolutionary timescale of 3.1×10^7 years.

Our *ensemble analysis* of the first 13 sdBV stars determined that log g (as expected) has a much larger effect on sdBV stars than does $\mathrm{T_{eff}}$. With this knowledge, we removed the log g dependence of the pulsation periods and compared the temporal spectra of the 13 sdBV stars. We find that additional parameters (perhaps age or composition) need to be accounted for before we can fully understand the pulsation periods in the majority of the class.

We also developed new tools for use in the asteroseismology of close binaries. Eclipsing binaries can provide a method to uniquely identify modes of pulsation, provided the pulsation

axis is aligned with the rotation axis. We noticed that if the tidal force of the companion is stronger than the Coriolis force, then the pulsation axis may align with the companion (much like the pulsation axis in rapidly oscillating Ap stars aligns with the strong magnetic field in those stars). From simulations, we determined that such a condition will present 3 signatures in the light curves and temporal spectrum, from which it is possible to uniquely identify pulsation modes. From preliminary data on PG 1336, we find strong evidence that this sdBV star in a 2.4 hour binary system has a pulsation axis that points towards the companion.

Studies of sdB stars represent a rapidly progressing field in stellar astronomy. Through sdB stars, we may hope to constrain nuclear physics by measuring evolution rates driven by helium fusion. We may obtain a better understanding of other horizontal branch stars, such as RR Lyrae stars, which are used as standard candles. Such an understanding will filter down through stellar evolution in an increased understanding of giant branch and white dwarf stars. Subdwarf B stars themselves will place constraints on white dwarf evolution as they will evolve to a distinctly lower mass white dwarfs than average.

CHAPTER 1. INTRODUCTION

If astronomy is the oldest of the sciences, then stellar astronomy is the oldest sub field of a science. Stars are potential laboratories for extreme physical conditions unattainable on Earth. Their interiors sample temperatures, pressures, and densities that we cannot hope to duplicate in terrestrial laboratories. However, accessing data from these stellar laboratories is difficult. The only information we get is from their outermost layers through the light we see from them. Furthermore, we cannot directly manipulate the conditions, but must passively observe what Nature provides. Though stars have been studied for millennia, only in the past thirty years have astronomers developed tools to directly study stellar *interiors*.

We face a similar challenge in studying the Earth.Though we are free to explore the surface we are unable to journey to the interior. However, science of seismology has revealed the Earth's detailed structure to its very center. Seismic waves, produced by earthquakes are sensitive probes of Earth's interior conditions such as density, pressure, and compressibility. Similar waves, first seen on the Sun in the 1970s, now give us a detailed picture of the solar interior (Christensen-Dalsgaard & Dziembowski, 2000) through "helioseismology." For some stars that show suitable light variations, astronomers are starting to use "asteroseismology" to give us a limited but direct view of stellar interiors. Already asteroseismology results have refined significantly our current picture of white dwarf evolution, for example (Clemens, 1994a).

Asteroseismology is still a new area of research and its tools are still being developed. In this thesis, I apply current tools of asteroseismology to a recently discovered class of variable stars, the EC 14026 (commonly called pulsating subdwarf B or sdBV) stars (Kilkenny *et al.*, 1997a). These are multi-mode pulsators which are well suited to asteroseismological analysis.

This introductory chapter continues in §1.1 with a brief overview of what we know about

stars and their evolution. Section 1.2, discusses the subdwarf B (sdB) stars and how they fit into the picture of stellar evolution. I next give an overview of their observed seismological properties in §1.3. Section 1.4 concludes this chapter by outlining the goals of this thesis and anticipates the results of my work.

1.1 Evolution of Solar-Type Stars

A useful definition of a star is that it is a gaseous, self-gravitating, quasi-equilibrium body that, sometime during its evolution, generate the majority of its radiant energy via sustained nuclear fusion. Our Sun, the closest example of a star, is merely an average star, burning hydrogen more-or-less consistently over the last 4.6 billion years. It should continue to do so for the next 5 billion years or so. It was not one of the first stars to be created, but rather coalesced out of interstellar gas that had been enriched in heavier elements by previous generations of stars. This brief diversion is by no means a complete picture of stellar evolution. Numerous resources exist which not only provide a more complete picture of stellar evolution, but do so with a precision, eloquence and length I would not dream to put here. Such references include Clayton (1968), Böhm-Vitense (1991), Hansen & Kawaler (1994), and a number of others.

Figure 1.1 introduces the Hertzsprung-Russell diagram (HR); this is a convenient and traditional vehicle for displaying stellar properties. Surface temperature (or a surrogate like color) is the abscissa and luminosity (or its surrogate) the ordinant. The representative HR diagram shows an old population of stars. The main sequence (MS) represents stars in their longest lived phase of core hydrogen fusion. This phase consumes 90% of a star's active (nuclear fusion) lifetime, or about 10^{10} years for stars like the Sun. Eventually the star's core runs out of hydrogen to burn, leaving behind a helium core as the star leaves the MS. For stars with masses less than about eight times that of our Sun, they will proceed to the red giant branch (RGB) as the helium core contracts while the surrounding material (called the envelope) expands. As the core contracts, it releases gravitational energy to support the star, heating the interior until the core becomes hot (and dense) enough to fuse helium into carbon and oxygen. For stars with masses larger than about two solar masses, helium ignition proceeds quiescently,

while for less massive stars, the core first becomes highly compressed and degenerate. In the latter case, this is a somewhat traumatic event as the compressed core undergoes a brief period of runaway thermonuclear fusion known as the *helium flash*. During the flash, some envelope mass may be lost; the post-flash stars have a range of remaining mass.

Whether commencing with a helium flash or quiescently, stars which are burning helium in their core are collectively called horizontal branch stars[1]. For the vast majority of horizontal branch stars, a sufficient envelope remains to maintain hydrogen shell burning during the horizontal branch phase. These stars consume their core helium fuel, then proceed to the asymptotic giant branch, become planetary nebula nuclei in rapid succession (i.e. in $< 1/10$ of their main sequence lifetime) and end their existence as white dwarfs.

1.2 Subdwarf B Stars

Some horizontal branch stars have very thin hydrogen layers and are exceedingly hot; these are the sdB stars. Shell hydrogen burning cannot be supported by such thin envelopes and it is likely they proceed directly to the white dwarf cooling track without reaching the asymptotic giant branch. They represent a small subset of all the horizontal branch stars; approximately 30% of horizontal branch stars are extended horizontal branch stars (Landsman *et al.*, 1998; Yong, Demarque, & Yi, 2000); including sdB and sdO stars, as measured in old open clusters. Their origin remains a mystery as the mass loss process must stop just in time to leave $< 10^{-2} M_{\odot}$ of hydrogen, but not remove it all. Though they are rare, they are also quite luminous, and so are not hard to find.

Prior to spectroscopy by Greenstein (1966), it was suspected that many faint blue stars (now known to be sdB stars) were possibly of an extra-galactic nature. However Greenstein (1966) obtained radial velocities that proved they were within our own galaxy and hypothesized that they are the field counterparts of the extreme horizontal branch (EHB) stars (HB stars with surface temperatures hotter than ~25,000K) detected in some globular clusters. In the early 1980s, the Palomar Green survey (Green, Schmidt, & Liebert, 1986) detected over 500

[1]See Figure 1.1; note also that the horizontal branch does not extend to the blue for stars with solar metallicity, but for lower metallicity only.

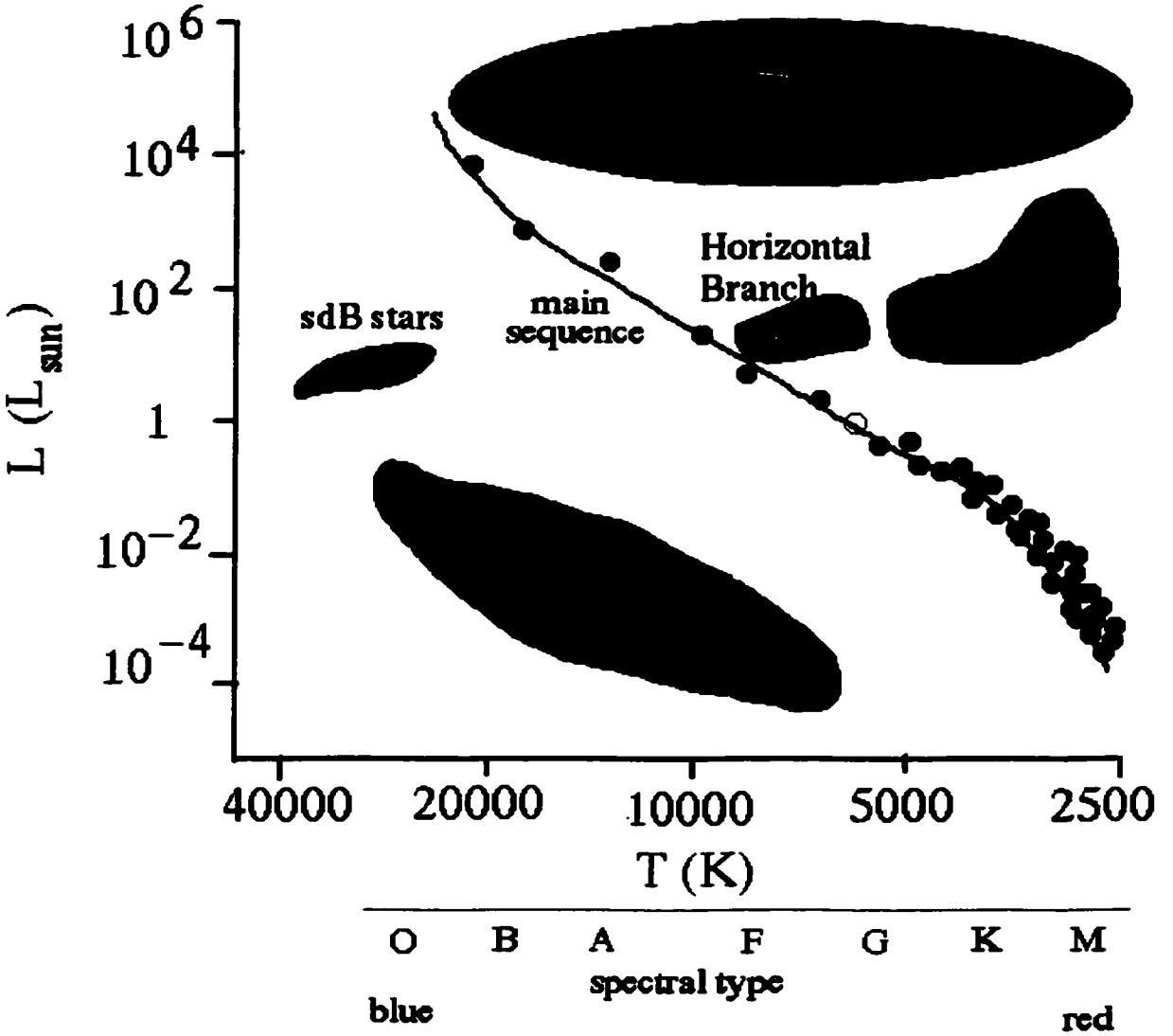

Figure 1.1 A Hertzsprung-Russell (HR) Diagram with various phases of stellar evolution indicated.

sdB stars (representing 40% of all point sources in their sample) in a search for quasi-stellar objects (or quasars). The Kitt Peak Downes survey (Downes, 1984) also detected a large number (~60%) of sdB stars.

More recently, the Edinburough-Cape survey (Kilkenny *et al.*, 1997b) detected large numbers of sdB stars (44.9% of all points sources in their sample), as well as the first pulsating sdB star (Kilkenny *et al.*, 1997a). Subdwarf B stars have also been detected in open and globular clusters (Moehler *et al.*, 2000; Thompson *et al.*, 1999; Liebert, Saffer, & Green, 1994) and are suspected to exist in elliptical galaxies (Brown *et al.*, 2000), indicating that they can be produced in all stellar environments. With such a large sample of sdB stars, it is prudent to understand their physical characteristics and ask what role they play in stellar evolution.

1.2.1 Outside Appearances

Saffer *et al.* (1994) were the first to characterize in detail the observed properties of sdB stars. They obtained medium resolution spectra over a wavelength region containing many hydrogen Balmer lines (3650—5200 Angstroms). Saffer *et al.* (1994) determined the effective temperature (hereafter $T_{\rm eff}$) and surface gravity ($\log g$) by simultaneously least squares fitting the Balmer lines with model atmospheres. Such atmospheric models calculate line shapes using Stark broadening (which reflects the electron density) and Doppler broadening (as a measure of the kinetic temperature). These processes affect the spectral lines differently than rotation (which changes the overall line profile) or magnetic fields (Zeeman splitting tends to broaden and flatten the line core). Matching the observed line shapes to the models provides reasonable constraints on $T_{\rm eff}$ and $\log g$. From their spectroscopic work, Saffer *et al.* (1994) determined that sdB stars have effective temperatures greater than 25,000 K and surface gravities ($\log g$) greater than 5.0. They have atmospheres dominated by hydrogen with observed Balmer lines which often extend to $n = 12$ before the line wings overlap.

Figure 1.2 contains two Hertzsprung-Russell (HR) diagrams. The first shows the position of variable stars of all types (including sdBV stars) for a broad range of temperature and luminosity while the second HR diagram zooms in on the region of sdB stars. The second

HR diagram also contains model results indicating the effects of varying the helium core and hydrogen shell mass. It is clear that changing the core mass, even by a tenth of a solar mass substantially changes where the star appears on the HR diagram. The temperature depends steeply on the thickness of the hydrogen layer, with slight changes (on the order of one thousandth of a solar mass) causing wide variations in effective temperature. Models such as those in Figure 1.2 (and discussed in Chapter 2), indicate that sdB stars consist of an $\approx 0.5M_{\odot}$ helium (He) burning core surrounded by a $\leq 0.02M_{\odot}$ layer of H.

Subdwarf B stars, with their thin ($\leq 0.02M_{\odot}$) hydrogen blankets, will not have significant shell hydrogen burning, and so will (theoretically) proceed directly to the white dwarf (WD) cooling track. Figure 1.3 indicates an evolutionary model for an sdB star with an envelope thickness of $0.0015\mathrm{M}_{\odot}$. In none of the cases with temperature ranges consistent with sdB stars does the model evolve to the AGB. Their current mass limits already mean that they will end up as low mass WDs. The average WD mass is $\sim 0.60M_{\odot}$ while sdB stars only contain $\leq 0.5M_{\odot}$ of material. Thus they can only produce a small fraction of observed WDs, less than one in every 100 white dwarfs was an sdB star. This is consistent with their relative space densities, also (Downes, 1984).

1.2.2 Binarity

Many sdB have companions[2]. Maxted *et al.* (2001) determined that 21 of the 36 sdB stars they observed have radial velocity variations indicative of short period binaries with unseen companions. Including angles for which it is impossible to detect radial velocity variations, they infer a minimum fraction of 60% for sdB stars in short period binaries. Green & Liebert (2000) searched for radial velocity variations in a sample of over 70 sdB stars, from which they conclude that 45% of their sample are short period binaries with unseen companions and an additional 20% are long period binaries with main sequence companions.

A search for composite spectrum binaries by Ferguson, Green, & Liebert (1984), turned up 24 composite spectrum binaries (selected for their colors in narrow band photometry of over

[2]See Appendix A for a complete discussion.

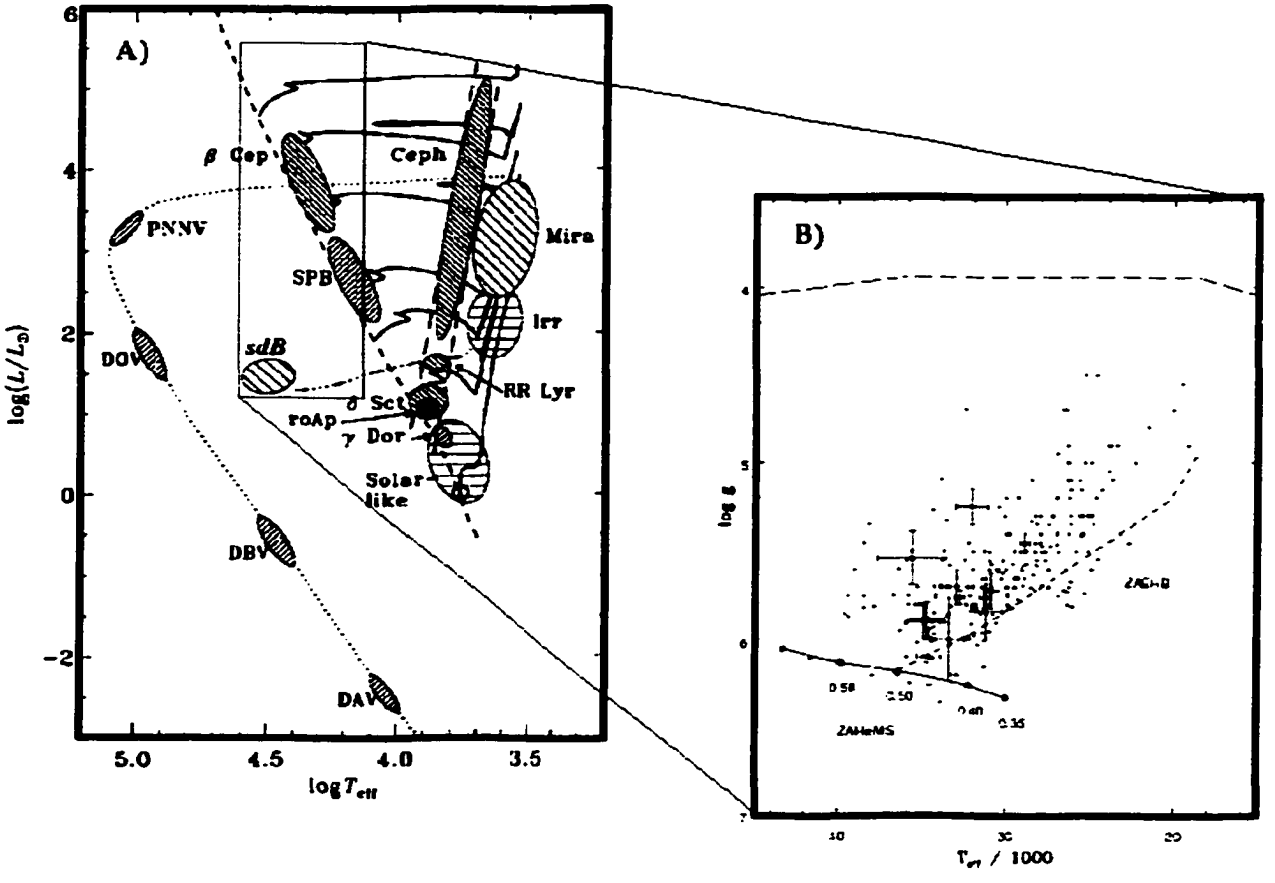

Figure 1.2 H-R Diagrams. A) An HR diagram with variable stars labeled (from Christensen-Dalsgaard & Dziembowski, 2000). The Zero age main sequence is indicated as a dashed line, the white dwarf cooling track as a dotted line and the horizontal branch as a dot-dashed line. B) Close-up of HR diagram as typically seen in studies of sdB stars (surface gravity rather than luminosity). Solid line is the Zero-Age-Helium-Main-Sequence (ZAHB) for core masses provided (in $M_{\odot}$), dotted line is the Zero-Age-Extended-Horizontal-Branch (ZAEHB) and dashed line is the Zero-Age-Main Sequence (ZAMS). Pulsaters are indicated by filled circles with error bars while non-pulsators are shown as triangles. Note that by converting from luminosity to $\log g$, we effective tip the HR diagram by about 60 degrees (best seen by comparing the line for the main sequence in the two plots).

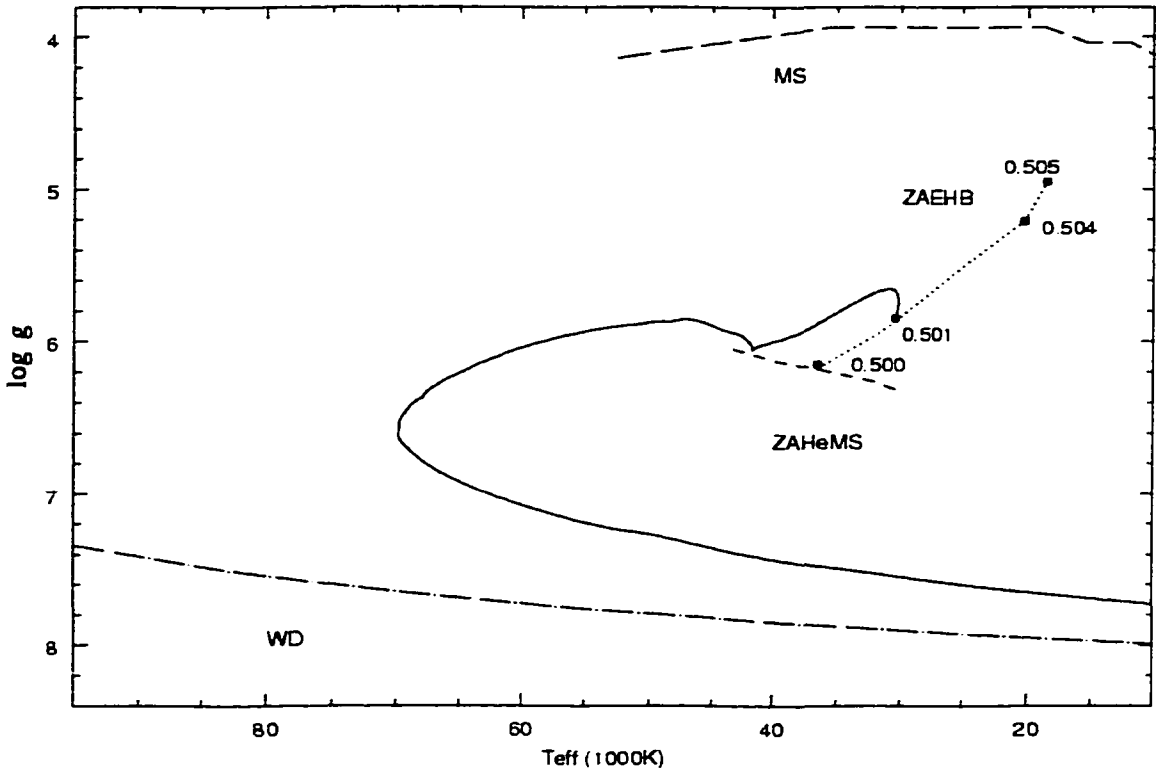

Figure 1.3 Evolutionary diagram of a typical sdB model evolving away from the ZAEHB (solid line). Also shown are the ZAHB, a white dwarf cooling track (for $0.6M_{\odot}$; courtesy of M. Wood), the zero age main sequence (starting from O3; Lange, 1991) and the zero age supergiant sequence (starting from O5; Lange, 1991) (as labeled).

200 stars), from which they infer that $\sim$ 35% of all sdB stars have main sequence companions later than spectral type K5. O'Donoghue *et al.* (1999) detect composite spectrum binaries in 4 of the 9 sdBV stars they observed, a number slightly higher than that of Ferguson, Green, & Liebert (1984), but consistent given their low number of observations.

Ulla & Thejll (1998 and references therein) used infrared observations to find that 39 of 92 sdB candidates have an infrared excess, indicative of a main sequence companion. Appendix A includes our work using the *Two Micron All Sky Survey* (2MASS), where we find that $\sim$40% of sdB stars (from a sample of nearly 500) have an infrared excess indicative of a main sequence companion.

Though there is much work yet to be done in this area, it appears that many sdB stars are in binaries. It is therefore prudent to question what affect this might have on their pulsation properties. We will examine this question in Chapter 3.

1.2.3 Speculation About the Origins of Subdwarf B Stars

A mystery concerning sdB stars is how they arrived at their current location on the HR diagram. After the helium flash, nearly all of the hydrogen envelope must be shed in order to reach the effective temperatures sdB stars have. Saffer *et al.* (1994) suggest three mechanisms for producing sdB stars; these remain under active debate.

1.2.3.1 Single Star Origin

The EHB stars (both sdB and their hotter counterparts the sdO stars) could be anomalously slow cooling post-AGB stars. Though this may be a valid theory for sdO stars (which like AGB stars show a range of core masses), it is an unlikely explanation for sdB stars since the evolutionary timescale for post-AGB stars is inconsistent with the observed space densities. Or, perhaps through some, as-yet unexplained mechanism, the helium flash is sufficient to remove all but a thin layer of the hydrogen envelope (D'Cruz *et al.*, 1996). This may be caused by higher than normal envelope opacity (such as the formation of dust, or other molecules which are able to absorb a wider range of photons). Since sdB progenitors must be at least $\approx 0.8 M_{\odot}$ (to have evolved off the main sequence in less than the age of the Universe), they must eject $> 0.3 M_{\odot}$ of material. We might expect to see this material as an infrared (IR) excess, predominantly around young (close to the zero-age helium main sequence) sdB stars. Though infrared excesses have been detected in some, they usually have been related to companions, rather than to dust or ejected material.

1.2.3.2 Binary Production

Another possibility is that sdB stars are created via close binary evolution. Iben & Tutokov (1986a, 1986b) proposed a process in which the hydrogen envelope is lost to the companion's

gravity prior to the onset of helium fusion. This star becomes a helium degenerate until the companion becomes a red giant, expanding and donating material to the primary, which condenses enough to ignite helium and becomes an sdB star. If this were the case, we could expect to see a multitude of sdB stars in short to intermediate period binaries (which we do; see §1.2.2). More pronouncedly, sdB stars that are merged binaries should show rapid rotation. The accretion of matter from the companion would serve to spin up the sdB, making it a rapid rotater. Observations have failed to support such a theory as most sdB stars appear to be slow rotaters (Heber, Reid, & Werner, 2000).

Another possibility involving binarity is that degenerate helium-helium or helium-carbon/oxygen pairs merge to form a single, helium burning star, which could resemble an sdB star (Iben & Tutokov, 1986b). However, this would again produce a rapidly rotating star. This possibility would also require a substantial fraction of close binary degenerate pairs. Though some (<10) have been detected recently, it is far from sufficient to produce the number of observed sdB stars. Substantial numbers of sdB stars appear to be in binaries (see §1.2.2), ruling out any merger theory for the creation of more than a small fraction of the whole.

1.3 Pulsating Subdwarf B Stars

The first variable sdB stars were discovered by Kilkenny *et al.* (1997) in 1994. Since then, over 20 members have been discovered, with a handful of new members being discovered every year (see Reed, Kawaler, & Kleinman [2000] for a review of the first 13 members). The variable sdB stars range in temperature from 28,000 to 40,000 K and in surface gravity from log g=5.2 to 6.1, so they tend to represent the hotter sdB stars. Nearly all of them lie near the zero-age-extended-horizontal-branch (ZAEHB), indicative of core helium burning, rather than shell helium burning. This is expected as core helium burning can last an order of magnitude longer than shell burning.

1.3.1 Overview of Pulsation Properties

The variations seen in sdB stars, usually seen via white light photometry, have periods from 80 seconds to 530 seconds; most pulsators show periods between 100 and 200 seconds. The largest pulsation amplitude discovered to date is ~3% (~30 mmag) while most pulsations are less than 1% (<10 mmag). Short duration data sets typically detect 2 or 3 pulsation periods, while multi-site or extended observations frequently reveal a host of lower (typically a factor of 5 or so) amplitude modes.

The pulsation frequencies are near values suggestive of the fundamental radial pulsation mode (see §2.2.1), but there are too many pulsations over a small range in frequency for them to be strictly radial. This means non-radial pulsations are required to account for at least some (if not all) of the pulsations.

1.3.2 Pulsating Subdwarf B Stars as Probes of Stellar Evolution and Stellar Systems

If sdB stars do indeed represent a small channel of of white dwarf formation, why are they so important? We cannot identify uniquely the production mechanism of sdB stars. As such, they need to be accounted for if we are ever going to claim a complete knowledge of stellar evolution. Another benefit of understanding sdB stars and their evolution is they provide a window to what occurs at the helium core flash. Accounting for their thin hydrogen envelope will surely shed light on what occurs in most stars as they pass through this poorly understood phase of evolution. Subdwarf B stars are the most common objects (including galaxies, QSOs, etc.) detected in blue all-sky surveys, so understanding their demographics will be required for any statistical characterization of future deep surveys.

Subdwarf B stars have also been detected in globular clusters. Some globular clusters also have an excess of ultraviolet (UV) radiation. It is possible sdB stars emit a significant fraction of this radiation. A similar problem is observed in elliptical galaxies; a larger, but similar environment to globular clusters. Should it turn out that sdB stars are the cause of this UV excess, population synthesis studies, which try to understand stellar populations, will need to

incorporate accurate models of sdB stars (Dorman, O'Connell, & Rood, 1995)

Evolutionary models (introduced in Chapter 2) indicate that sdB stars should have very thin envelopes. If so, they do not possess many of the theoretical problems a thick, hydrogen burning envelope encompasses (such as a hydrogen burning layer). Therefore, they represent a simplified version of horizontal branch stars. Asteroseismology, when it works, can provide tight constraints on the stratification (by composition) of the outer layers of a star. So, the pulsators may allow us to measure the hydrogen layer thickness and directly test these models. By studying sdB stars, we can gain insight into all HB stars, revealing the structure of core helium burning stars. Additional applications may be found in their similarity, and striking difference to RR Lyrae stars; which are important distance indicators for galactic structure studies. RR Lyrae stars are horizontal branch stars with thicker, hydrogen shell burning envelopes. If we understand sdB stars, we better understand the core conditions of RR Lyrae stars.

Stellar models show that core helium burning can provide support against gravity in an sdB star for roughly 10^8 years (Saffer *et al.* 1994). During this time, the core is consuming its supply of helium and producing carbon and oxygen. This changes the mean molecular weight of the core, changes which propagate throughout the star. By observing small changes in sdB stars, such as secular changes in the pulsation periods, it may be possible to place limits on helium fusion via the triple alpha process, something which no Earth-bound lab can do. It is their somewhat simplified structure that again works to our advantage as small changes in temperature or radius can only be attributed to evolutionary changes in density (likely due to composition changes) or structure within the star.

1.4 The Goals of this Work

We would like to use the observed pulsation properties of the sdBV stars to determine their physical structure and by extension, the structure of all horizontal branch stars. We would like to understand how sdB stars in general are produced, where they will evolve to next, and the role binarity plays in this process. Once we understand how sdB stars are formed, we can

determine the role sdB stars play in stellar populations. globular clusters.

These are big issues which require a large amount of effort in theory and various modes of observation. A coherent scenario for sdB formation and evolution can only come from coordinated attacks on various fronts. A key effort will be the determination of the hydrogen layer thickness and evolutionary timescales of these stars and for these, seismological analysis is well suited.

In order to solve these issues, we must have a more complete observational picture of the pulsations and form a link between the observed pulsations and the models from which we derive the physical structure. To do this requires follow-up observations and multi-site campaigns on additional sdBV stars as well as the ability to identify pulsation modes. We can only match theory to observations if we can identify the pulsation mode.

We concentrate on four sdB stars that span a range of evolutionary stage, and periods. They include two obvious binaries (one short period and one long period), one evolved sdB star and another that is the coolest sdBV discovered to date. These stars also span the observed range of pulsation periods. For two of these stars, extensive observations were obtained locally at Fick Observatory as well as with the Whole Earth Telescope (WET).

In this approach to the problem, some milestones included:

- Quantifying the effects of binary motions on pulsation observations.
- Characterizing the fully resolved temporal spectra of two objects for the first time.
- Identifying frequency spacings in one object.
- Establishing relative stability of amplitudes and frequencies of pulsations in three objects.
- Establishing tight upper limits on the rate of change of pulsation period (an indicator of evolutionary timescale) for one object.
- Demonstrating that frequencies and amplitudes of pulsations are not stable on timescales of years in the most evolved sdB star studied.
- Placing interesting constraints on planetary companions to an sdB star.

- Exploring the systematics of pulsation periods versus global stellar properties.
- Developing tools for mode identification through eclipse mapping.
- Showing peculiar phase variations in PG 1336 that did not conform to the standard model of stellar pulsations.
- Simulating the observed phase variations with a model that had the pulsation axis tipped compared to the orbital (and rotation) axis.
- Exploring influence of partial eclipse in the tipped axis model.

This thesis is divided into nine chapters with one appendix. This first chapter has served to provide a framework for the following investigations by outlining our current knowledge of sdB stars and their place in stellar evolution. It also poses the questions which sdB researchers hope to answer, with this thesis providing a trail to follow. Chapter 2 details the observational methods used. It also summarizes the theoretical background within which we interpret the observations. Chapter 3 addresses the complications that arise for pulsators in binaries. Chapter 4 introduces the four stars that we concentrate on. Chapters 5 describes frequency analysis and model fitting for individual stars. In Chapter 6 we look at period stability in an effort to find secular period changes driven by evolutionary changes. Chapter 7 examines the entire pulsation class, looking for trends which may be used to identify pulsation modes. Chapter 8 discusses the case of PG 1336, an sdB in a tight binary that showed lots of surprises. We conclude in Chapter 9 with a summary of the results in this thesis and speculations on what to do next.

In addition, in the appendix I review various methods that may be used to determine the fraction of sdB stars in binaries and extend one method to search for companions with infrared data from the 2MASS survey.

CHAPTER 2. ASTEROSEISMOLOGY METHODS AND TOOLS

Chapter 1 began with the acknowledgment that we do not have easy access to the physics of the interiors of stars. The key to unlocking their interiors has been the discovery (through time series photometry) of normal-mode oscillations in stars. As an example of the power of oscillation analysis, consider an everyday example of normal mode vibrations such as the tones produced by tapping a drinking glass. If I have three opaque glasses, each containing a different amount of water, I can tap the glasses and deduce the level of the water without otherwise examining their contents. On a much larger scale, the monitoring of oscillations of the Earth provides our only view of its interior. It is doubtful that we will ever drill to the center of the Earth to examine, firsthand, the interior of our planet. Yet we assure our children that our planet has a solid iron core, surrounded by a molten iron layer, above which lies a semi-solid mantle and a crust. We can do this because, just like tapping glasses filled with unknown substances, seismologists use earthquakes, which "ring" through the Earth, to study its interior.

The same is true for stars. The vibrations in stars manifest themselves in the form of pulsations, periodic changes in a stars' light. For the pulsations to persist coherently they must oscillate in normal modes. Furthermore, there must be an energy source that can overcome natural dissipation. The art of analyzing these normal modes of oscillation to deduce the underlying structure of the star is known as *asteroseismology.*

Classical (single period) variable stars were first discovered in large numbers in the 19^{th} century; stellar pulsation theory developed throughout the 20^{th} century to explain the periodic light variations. Discovery of multi mode pulsators, and theoretical analysis, blossomed in the second half of the 20^{th} century. Practical application of the theory has been driven by

high quality data that allows extraction of many frequencies and minimize uncertainty due to aliases (daily, monthly, etc., described in §2.1.3). In this chapter, I describe the procedures used to obtain these data, and then outline pulsation theory as addressed by the data in an asteroseismological analysis. The next section discusses the instruments used to obtain the data and the reduction process. Section 2.2 briefly reviews relevant pulsation theory and connects theory to the observations described in §2.1. The point of contact that allows us to constrain stellar physics is the pulsation periods. Section 2.3 outlines construction of evolutionary stellar models and calculations of their normal-mode frequencies. In §2.4 we detail how the observations are compared with the the theory. The last section reviews some successful applications of these techniques.

2.1 Obtaining and Reducing Time-Series Photometry

The stars examined in this thesis have pulsation periods of a few minutes. They are multi periodic, with periods spaced closely together. This makes it important not only to have many integrations per pulsation cycle to measure the periods themselves, but also a long time series to fully resolve the beat cycles of closely-spaced modes. To accomplish this, data have been obtained with photoelectric photometers during single and multi site campaigns. We observe for as long as possible during each night, as well as through an observing season of weeks to months, so as to be able to resolve the complex pulsation spectra.

2.1.1 Photoelectric Photometry

The observations discussed in the remainder of this thesis (unless otherwise noted) were obtained with photoelectric photometers [hereafter just photometers; see Kleinman, Nather, & Phillips (1996) for details of a typical instrument]. Our photometers employ blue-sensitive photomultiplier tubes to count photons over equal time intervals (typically 5 to 10 seconds). The tubes reside behind selectable apertures, typically 0.5—4mm in size (mapping to ~5—40 arcseconds on the sky). The aperture size is selected to minimize the light from the sky and neighboring stars while collecting all the light from the target star (the image size being de-

termined by atmospheric transparency). The main difference between individual photometers is the number of aperture+tube "channels". Single-channel photometers require frequent observations of nearby blank sky to allow for removal of variable sky background. This produces brief gaps in the data as we must physically move the telescope off the target to the sky patch and then re-acquire before observations can continue. So long as this is done infrequently and non-periodically, the impact of the small data gaps for the target is minimal. Single-channel photometers also require guiding external to the photometer, typically via CCD autoguider, to keep the target centered in the aperture. Dual channel photometers allow simultaneous observations of a non-variable comparison star along with the target. This second star can be used to monitor, and sometimes correct for, sky variations (even clouds to some extent). The data stream still must be interrupted occasionally to measure the sky background. Three-channel photometers devote a third channel just to sky observations (Kleinman, Nather, & Phillips, 1996). This additional channel eliminates the need to interrupt data (except once or twice at the beginning and/or end of a run), to correlate channel sensitivity. Two and three channel photometers typically allow internal guiding. A dichroic filter splits the light from the comparison star (channel 2) into blue and red components. The blue light is sent to the blue-sensitive tube while the red component is used for CCD (or occasionally manual) guiding.

At the conclusion of each integration, a single number, the counts as read by an offset voltage across the tube, is stored for each channel. Along with a small header produced at the beginning of each observing run, this is sufficient information to examine how the brightness varies with time (kept as Universal Time) throughout the run.

2.1.2 Data Reduction

The software used for reduction of time series photometry in this thesis is QED, written by Dr. Ed Nather (Kleinman, Nather, & Phillips, 1996). The goal of data reduction is to reproduce the time-varying brightness of the target star as if it was seen from above the Earth's atmosphere. To do this, we begin by constructing a point-by-point record of the sky brightness, to remove this contribution from the star counts. For 3 channel photometers,

a channel is dedicated to the sky, and a complete record is obtained along with the stellar data. For 1 and 2 channel photometers, sample sky measurements have to be interpolated. An average is found for each small group of sky samples and a continuous form of the sky brightness is created by linearly interpolating between averaged sky points.

To correct for atmospheric extinction, we approximate the effect using a single coefficient cosecant function of the air mass ("air mass" is equivalent to the altitude of the target above the horizon). The data are then corrected for extinction and, if necessary, the coefficient is adjusted and refitted until the light curve shows no linear or quadratic trends. Seeing and anomalous atmospheric transparency changes are corrected either by removing a low order polynomial fit to the data, or by dividing through by the (smoothed) data from the comparison star. Bad points (from electronic noise, sky measurements, guiding errors, etc.) are removed by hand, and the mean level of the flattened light curve is removed, leaving only the variations from the mean. ($ma = \Delta I/I$). Finally a barycentric correction is applied to correct for the Earth's motion around the Sun, giving times for the data points projected to the center of the solar system. An example of data obtained with a 3 channel photometer is shown in Figure 2.1 where the "raw" light curve is clearly dominated by clouds (see Kleinman, Nather, & Phillips, [1996] for other examples of the reduction procedure).

2.1.3 The Temporal Spectrum

A Fourier transform of the reduced light curve produces a measure of the amplitude of variation as a function of temporal frequency. In such a "temporal spectrum" peaks correspond to periodic signals (or gaps) in the light curve. In the temporal spectrum, the height of each peak is proportional to the amplitude of the variation from the mean signal. The width of the peak is determined by the length of the data run. An example temporal spectrum is shown in the right hand panel of Figure 2.1. The y axis is "modulation amplitude" (ma, or in this case, milli-modulation amplitude, mma) which is the fractional variation in intensity There are three properties need to measure in the time series for each spectrum peak: period (or frequency), amplitude and phase. The enemy of such measurements are either short run

lengths (making it impossible to resolve the pulsations) or "aliases" which appear in the FT due to incomplete data sampling (an ideal FT would have data sampled from and to infinity). With few exceptions, single site observations will have incomplete data sampling with daily gaps as the star sets below the horizon, or the Sun rises. So when multiple runs obtained over several days at a single site are combined, these "gaps" produce unwanted peaks in the FT at integer multiples of one cycle per day on either side of the stellar periodicity. In this case, the period between gaps is one day so aliases would appear at multiples of 11.57μHz (11.57, 23.15, 34.72μHz, etc.). Such daily aliases are typical of time series data.

A good rule of thumb is if the difference between the two highest amplitude peaks of each alias "pattern" is higher than the noise in that region of the temporal spectrum, then the highest amplitude peak is likely the one caused by the star's variability and not an alias. Another typical rule is to never trust a peak that resides on another peak's alias, unless there is a very compelling reason to do so.

2.1.4 Beating Down Aliases with Multi Site Data

The best method of minimizing sampling aliases is to acquire a continuous time series by obtaining data from sites around the Earth. In doing so, it is possible to get data with few, or even no gaps for days on end. The Whole Earth Telescope (WET) is one such network of astronomers, cooperatively observing targets for (typically) ten days to two weeks from sites around the globe (Nather, *et al.*, 1990). To qualitatively gauge the amount of aliasing in a data set, we compute a "spectral window function". The window function is the FT of a single noise-free sinusoid (of arbitrary but representative frequency) sampled in the same manner as are the actual data. Figure 2.2 shows spectral window functions for three different data samples. The top panel shows the window for the data in Figure 2.1, a single run; the middle panel for multi-night data from a single site (from §4.3); while the bottom panel has data from a multi site WET campaign on HL Tau 76. The central peak is at the frequency of the input sinusoid while all the other peaks are aliases caused by gaps in the data.

Once we have our data collected and reduced, we use a progressive linear least-squares

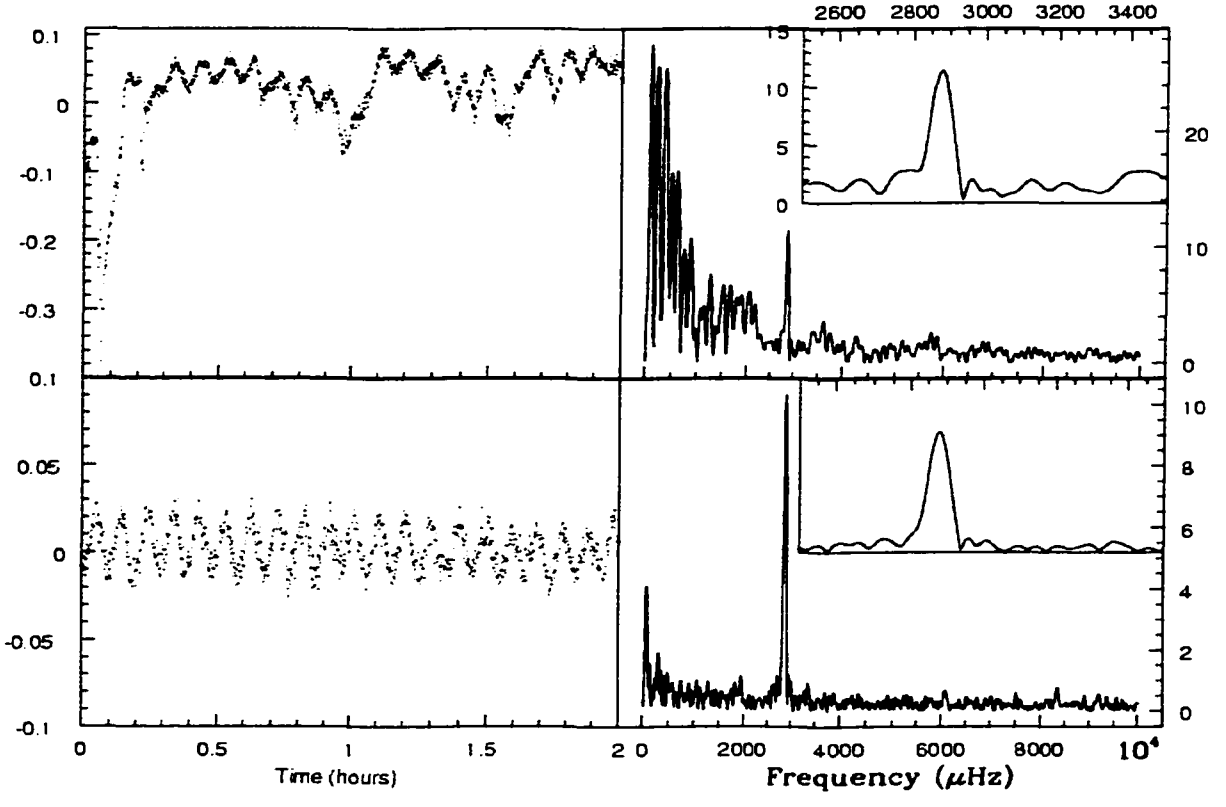

Figure 2.1 Raw (top) and reduced (bottom) photometric data. Left: Light curve (2 hours of a 6 hour run). Right: Temporal spectrum of the 6 hour run. Inset: 1000μHz close-up of the temporal spectrum showing the pulsation.

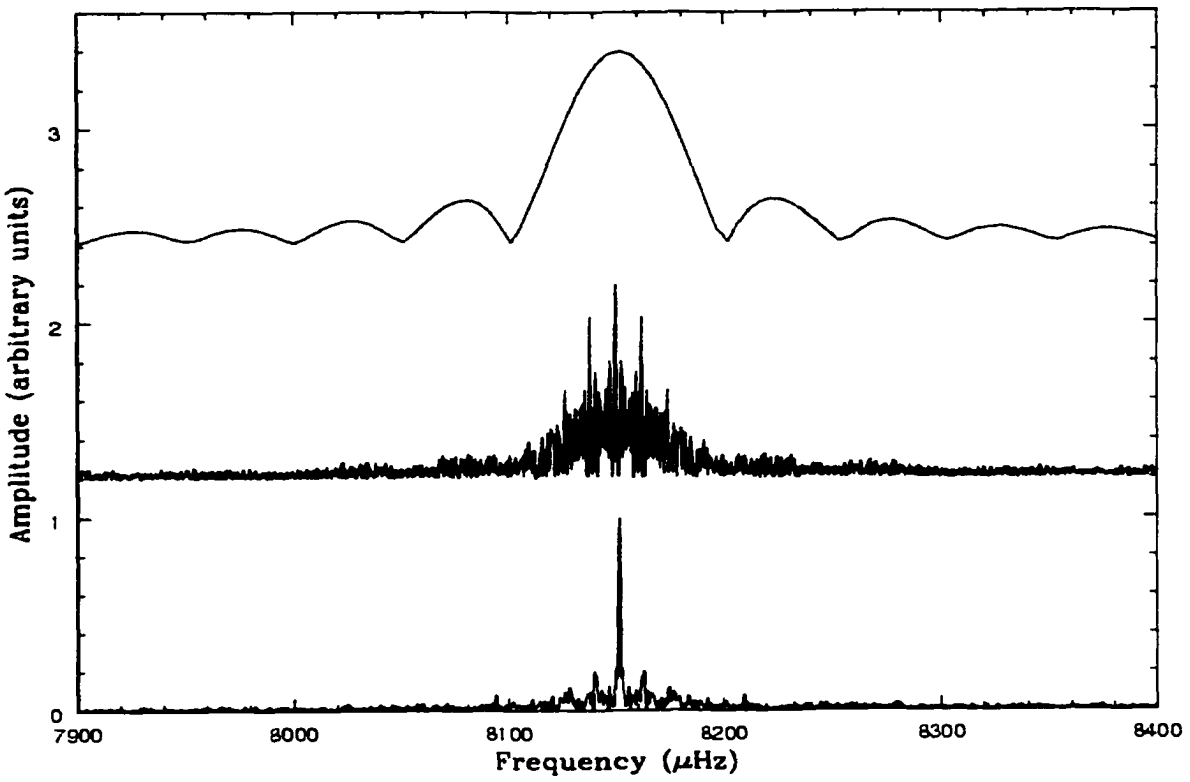

Figure 2.2 Window functions for a single run (top), multi run single site data (from March, 1999 see Table 4.5) (middle) and multi site data for HL Tau 76 (for a list of runs, see http://wet.iitap.iastate.edu/xcov18) (bottom).

(hereafter LSQ) analysis to obtain the periods, phases and amplitudes of all probable modes. We typically begin by attacking the highest amplitude mode (though prewhitening can be done in any order): we fit the time series to a noise free sinusoid to obtain that mode's period, amplitude, and phase. We then subtract the fit sinusoid from the original light curve and recompute an FT to reveal the remaining periodicity. This procedure, known as *prewhitening* continues one peak at a time, with the goal of removing all peaks deemed "real" until all that remains is noise. In such a manner, prewhitening serves to confirm the LSQ fit of the peaks. A bad LSQ fit will poorly prewhiten aliases. Examples will be shown later; but see O'Brien *et al.* (1996) for another example of this procedure.

This procedure has to be used with extreme caution. Prewhitening removes a set of noise-free sinusoids. Pulsations typically have some non-linear effects, such as amplitude variations and nonsinusoidal pulse shapes that are not accounted for. As a result, prewhitening does not completely remove, or over-removes, peaks and aliases. Periods should only be deemed real if they are seen in the temporal spectrum *prior* to prewhitening, as prewhitening does not fully remove aliases. Great care is needed taken to ensure that prewhitening confirms, rather than detects, peaks in the temporal spectrum. At the end of the analysis, we have a list of periods, amplitudes and phases for the dominant pulsation modes in the star. It is this list that provides the contact with theoretical models.

2.2 Pulsation Theory

The variations we see in sdBV stars are relatively small. Since they are small, we can consider the variations that we see as manifestations of small perturbations to the equilibrium structure of the star. In this limit, theoretical modeling of stellar pulsation requires simple linear perturbation theory. We begin with the equations of equilibrium stellar structure, introduce small perturbations to the structural quantities and then solve for the perturbations in terms of the equilibrium structure.

The details of modern pulsation theory are available in a host of textbooks and review articles (see for example Cox, 1980; Unno *et al.*, 1989, or the first comprehensive treatment by

Ledoux and Walraven, 1958). For the purposes of this section, we will merely quote relevant results of the theory in some interesting asymptotic regimes. Later, we will use stellar models and results of perturbation calculations with them for more detailed comparisons with the observations.

Since pulsations are a mechanical process, it is useful to define at this point the free-fall, or dynamical timescale

$$\tau_{\rm ff} \approx \frac{1}{\nu_o} \approx \frac{1}{\sqrt{G\overline{\rho}}} \; : \tag{2.1}$$

where $\overline{\rho}$ is the mean density of the star and ν_o is the corresponding frequency. This represents the global response time of the star to departures from hydrostatic equilibrium. For sdB stars, $\tau_{\rm ff}$ is of the order 100 to 200 seconds.

2.2.1 Classes of Pulsation Modes

The classes of oscillation modes available to stars are differentiated by the restoring force and geometry of the modes. When pressure is the restoring force (p-modes), the oscillations occur with periods that are shorter than or equal to the free-fall time for the star. Another important restoring force is buoyancy. For modes with buoyancy as the restoring force (g-modes), the pulsation periods tend to be much longer than the free fall time. As a terrestrial analogy, sound waves in water represent waves for which pressure is the restoring force. In the oceans, buoyancy is the restoring force for ocean waves at sea. Ocean wave patterns move much more slowly than sound waves in water for the same reasons that g-mode periods are longer than p-mode periods.

2.2.1.1 Radial Pulsations

When p modes are spherically symmetric, they are called radial modes. For normal modes, the oscillations within the star are standing waves, with nodes between the center and the surface. Across a node, the sense of the variation reverses. An n=0 mode, for example, has no nodes (except, trivially, at the center) and is called the radial fundamental. Radial modes with n=1 have a single internal node. In the limit of "large" n, radial pulsation frequencies

obey the asymptotic relation

$$\nu_n = \nu_o (n + \epsilon) \tag{2.2}$$

where ϵ is a small number. ν_o is given by the sound travel time through the star. It is approximately $1/\tau_{\rm ff}$, but more specifically

$$\nu_o = \int_0^R \frac{dr}{c_s} \tag{2.3}$$

where C_s is the local speed of sound. Another thing to note in Equation 2.2, is that if a star undergoes high overtone pulsation (large n), then its temporal spectrum should show a series of peaks which are evenly spaced in frequency.

Stars undergoing radial pulsation typically have n=0 or at most 1. Probably the best known of all pulsators are the Cepheid variables. These radial pulsators typically show the fundamental (n=0) mode, though first overtone Cepheids are fairly common also. Equation 2.1 shows that the Cepheid pulsation periods give us their average densities. Since the density (and luminosity) is a function of radius, and the effective temperatures of Cepheids fall in a narrow range (see Figure 1.2), Equation 2.1 leads to the famous period-luminosity relationship which has been used to calibrate extra-galactic distances. RR Lyrae stars are the horizontal branch equivalent of the Cepheids; pulsating in only one or two radial modes, they provide another standard candle from which astronomers can gage distances.

2.2.1.2 Nonradial Pulsations

The perturbed equations of stellar structure represent the behavior of material under the influence of a central inverse square force (gravity) and gas pressure. As such, general solutions do not require spherical symmetry. A natural way to describe the available nonradial oscillation modes is in terms of an orthogonal set of functions, known as the spherical harmonics. This familiar set of functions (denoted by $Y_{\ell m}$) is the same as used in perturbative quantum mechanics, electromagnetics and other areas of physics. The spherical harmonics describe the angular dependence of the variations via the quantum numbers ℓ and m. The number of nodal lines on the surface is given by ℓ, while m is the number of nodal lines passing through the

poles. Figure 2.3 shows sample patterns from the set of spherical harmonics. As expected there are $(2\ell + 1)$ possible values of m for a given ℓ, with the sign of m signifying the relative phase of the azimuthal pattern.

2.2.2 Asymptotic Properties of Nonradial Modes

In the limit of $n \gg \ell$, non-radial p-mode oscillation frequencies obey some simple asymptotic relations. For p-modes, we have

$$\nu_{n,\ell} = \nu_o \left(n + \frac{\ell}{2} + \epsilon \right) . \tag{2.4}$$

This equation shows that, as with radial modes, overtones are equally spaced in frequency. However, because of the ℓ dependence, the observed spacing may be $\frac{1}{2}\nu_o$ if modes of alternating ℓ are observed. Note also that radial modes correspond to ℓ=0.

The asymptotic relation for g-modes takes a different form. In the same $n \gg \ell$ limit, we have

$$\Pi_{n,\ell} \approx \frac{\Pi_o}{\sqrt{\ell\,(\ell+1)}}\,(n + \epsilon) \tag{2.5}$$

where Π_o is a constant that depends on an integral of thermodynamic quantities over the structure of the star. In sdB stars, it is about 200 seconds. The shortest period $\ell = 1$ g-mode will have a period roughly equal to the free fall time, with the period increasing with overtone n. In the asymptotic limit, g-modes are equally spaced in period for consecutive values of n (Smeyers, & Tassoul, 1987).

Unlike radial modes, the nonradial modes of differing n have very similar thermal and mechanical properties. Thus when stars show nonradial pulsations at all, they frequently show many modes. Since each mode does sample a subtly different part of the star (Christensen-Dalsgaard & Dziembowski, 2000), nonradial pulsators are more revealing of a star's interior than radial modes.

In stars that show nonradial pulsations we can usually identify whether it is a p-mode or g-mode pulsator by considering the pulsation periods themselves. With an estimate of the density of the stars, we can calculate ν_o. If the periods are much longer than $1/\nu_o$, then the pulsations

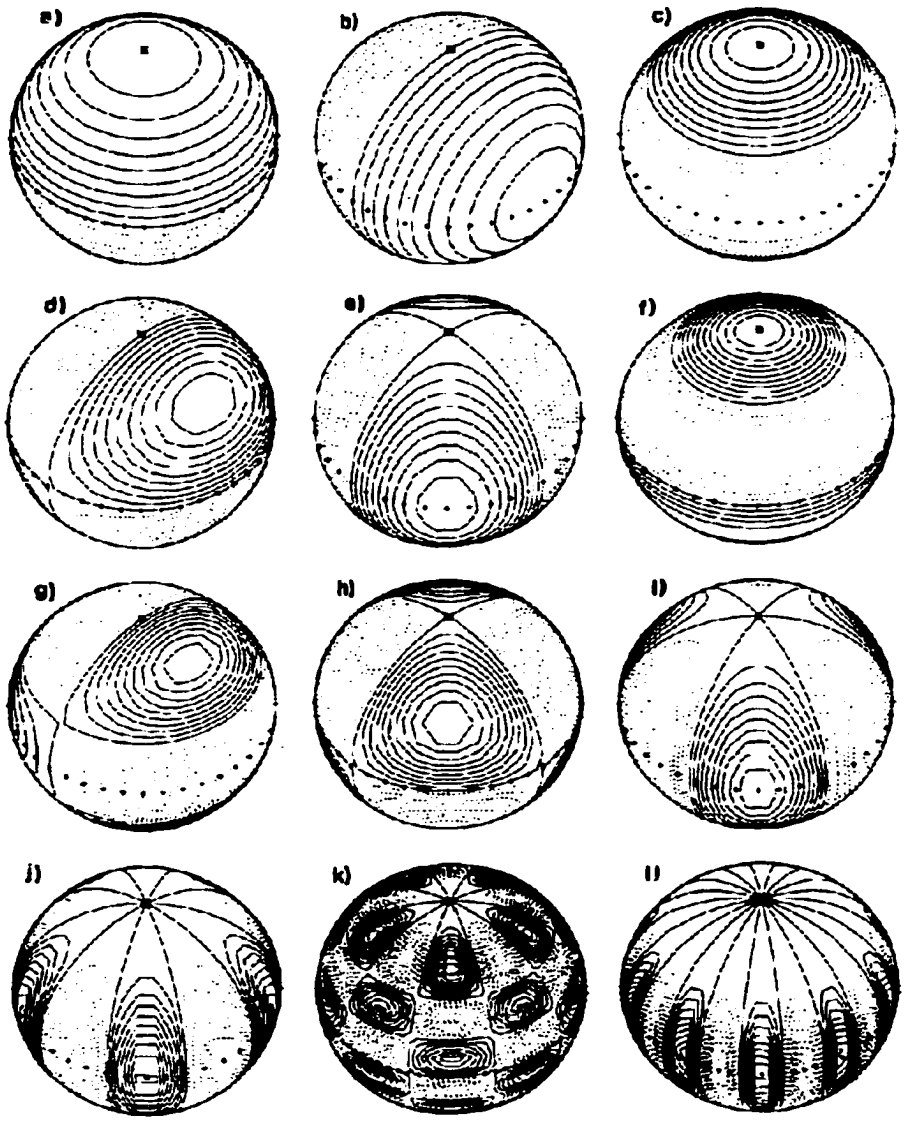

Figure 2.3 The geometric manifestation of pulsations with the following modes: a) ℓ=1, m=0, b) ℓ=1, m=1, c) ℓ=2, m=0, d) ℓ=2, m=1, e) ℓ=2, m=2, f) ℓ=3, m=0, g) ℓ=3, m=1, h) ℓ=3, m=2, i) ℓ=3, m=3, j) ℓ=5, m=5, k) ℓ=10, m=5, and l) ℓ=10, m=10. Cooler regions have solid lines while hotter regions are indicated by dashed lines. The pole is noted by a star and the equator by plus signs. (From Christensen-Dalsgaard & Dziembowski, 2000)

are probably g modes; if the periods are shorter than $1/\nu_o$, then p-modes are indicated. In cases where pulsation periods are comparable to $1/\nu_o$, then either observational constraints on the type of mode (radial versus nonradial) or detailed comparison between model periods and the observed periods is needed to establish the class of pulsation.

2.2.3 Effects of Rotation on Pulsation Frequencies

Equations 2.3 and 2.4 suggest that the pulsation frequencies do not depend on the value of m. Modes propagate around the axis of symmetry with a frequency of ν/m and so produce variations at the same frequency, independent of m. However, if the star departs from spherical symmetry in some way (i.e. by rotating), then modes with different m will be shifted in frequency away from the degenerate value. For example, rotation can separate modes of different m but the same ℓ into $2\ell + 1$ modes[1]. The frequency splitting between peaks of consecutive m is given by:

$$\delta\nu_{n\ell} = \frac{(1 - C_{n\ell})}{\Pi_{rot}} \tag{2.6}$$

so that

$$\nu_{n\ell m} = \nu_{n\ell o} + m\frac{1}{\Pi_{rot}}(1 - C_{n\ell}) \tag{2.7}$$

where Π_{rot} is the rotation period of the star. The number $C_{n\ell}$ is a correction term arising from the Coriolis force. For sdB stars, it is usually a few percent. Thus, rotation can produce $(2\ell+1)$ peaks, for a given value of n and ℓ, that are equally spaced in frequency in the temporal spectrum. An $\ell = 1$ set can become a triplet, an $\ell = 2$ mode a quintuplet, and an $\ell = 3$ mode a septuplet, if modes with all values of m are present.

The observed relative amplitude of modes with different m (assuming the same physical amplitude) will depend on the inclination angle between the pulsation axis and the line of sight; see Figure 2.3. If the star is viewed equator-on, the $\ell = 1$, $m = 0$ and $\ell = 2$, $m = 1$ modes will have equal numbers of bright/dim areas, effectively rendering those modes undetectable in the absence of limb darkening. The same is true for all $m \neq 0$ modes when the rotation axis is viewed pole-on.

[1]By convention (IAU Commission 27), modes with $m < 0$ have decreased frequency while modes with $m > 0$ have increased frequency.

2.2.4 Mode Trapping

The asymptotic equations predict equal frequency (period) spacings for p (g)-modes. However, implicit in deriving those relations is the assumption that the equilibrium models are homogeneous in composition. In practice, sdB stars (and most others) are chemically stratified. At points within the star where composition changes quickly with depth, a corresponding density jump must result to keep the pressure from being discontinuous. If there is a resonance between the radial dependence of the oscillation mode (the "wave" function or eigenfunction) and depth in compositional layer, the eigenfunction can get "trapped" in between (Kawaler & Weiss, 1990; Brassard *et al.*, 1991; Dehner & Kawaler, 1995). Such a trapped mode "feels" a diminished resonant cavity compared to non resonant modes, altering the pulsation period from the asymptotic value. Modes with neighboring n values will feel the transition slightly less as their nodes lie further from the transition region. However, as n increases the nodal spacing will become such that the next nodes will become closer and closer to the transition region, the pulsations will again "feel" a smaller cavity, and the periods will change accordingly. Thus we get an alternating pattern of pulsations that "feel" the smaller cavity with those that do not. This pattern, the *trapping cycle* (Bradley, 1994) and the *trapping period* (which is the number of modes of consecutive n of the trapping cycle), depends on the depth of the transition zone causing the trapping. The deeper the transition zone, the shorter the trapping cycle.

2.2.5 Changes in the Pulsation Period

The pulsation frequencies are extremely sensitive to the conditions (density, pressure,and temperature) of the star. Yet Chapter 1 shows that stars change with time. So must the pulsations. This is a small change as sdB stars are expected to spend $\sim 10^8$ years burning helium in their core (Saffer *at al*, 1994). How a star moves in the HR diagram is directly related to changes in radius. Thus the rate of change of the radius, controlled by nuclear evolution, will drive a change in the period at the same rate. If the star is evolving on a timescale of 10^8 years, then the pulsation period will change by roughly 1 part in 10^8 each year. This change is too slow to measure directly in the pulsation period of the star. However, these gradual

changes in the period will manifest themselves as accumulating changes in the phase of the pulsations. Over many cycles, these changes can become measurable (see §2.5.4).

In the case of sdB stars, as they evolve their radius generally increases, lowering the density of the envelope, and thus lengthening their pulsation period if they are p-modes. As such, we expect $d\Pi/dt$ (also called $\dot{\mathrm{P}}$) to be positive. In Chapter 6, I will provide a detailed look at how $d\Pi/dt$ is expected to change with time in sdBV stars. By analyzing pulsations of evolutionary models, it is possible to constrain the mechanism for driving evolution in sdB stars; helium fusion.

2.3 Detailed Stellar Models

Observed pulsations themselves tell us little about stars without models of the stars to use as interpreters. If I hear a bell ringing in the distance, I can make several bells, of varying size and thickness until my bell rings with the same frequencies as the one in the distance. Now I may assume that my bell shares many properties as the one that I can only hear, but not examine. So it is with stars. We need accurate stellar models that correspond to the observed constraints of T_{eff}, log g, and composition. We then compute their pulsation periods for comparison with the data.

2.3.1 Evolutionary Models

For this work, we generated models using the stellar evolution program, ISUEVO, which is described in detail in Dehner (1996), Dehner & Kawaler (1995), Kawaler & Bradley (1994), and references therein. We created models that span the observed regions (in T_{eff} and log g) of sdBV stars in the HR diagram (Figure 1.2).

ISUEVO is a "standard" stellar modeling code that solves the four equations of stellar structure:

$$\text{Hydrostatic Equilibrium:} \quad \frac{dP}{dM_r} = -\frac{GM_r}{4\pi r^4} \,, \tag{2.8}$$

$$\text{Mass Continuity:} \quad \frac{dr}{dM_r} = \frac{1}{4\pi r^2 \rho} \,, \tag{2.9}$$

$$\text{Conservation of Energy:} \quad \frac{dL_r}{dM_r} = \epsilon - T\frac{ds}{dt} \ , \tag{2.10}$$

$$\text{Thermal Balance:} \quad \frac{dT}{dM_r} = -\frac{GM_rT}{4\pi r^4 P}\nabla \ . \tag{2.11}$$

Symbols in Equations 2.6–2.9 have their usual meanings. The independent variable is M_r, the mass contained within the radius r, Δ is the logarithmic gradient of temperature with respect to pressure, ϵ is the energy production rate and s is the specific entropy.

The evolutionary sequence is advanced in time, beginning with a "seed" model. To create this starting model, we first assume that it is a "Zero Age Horizontal Branch" (ZAHB) star that has just completed the core helium flash (§1.1). Following standard practice, this seed model is presumed to be evolution-independent in that the degenerate helium flash (described in §1.1.1) occurs for a given helium core mass more-or-less independent of the total mass of the star. The helium core mass is solely a function of initial metallicity. We then add an envelope of hydrogen to the core, with the mass of the envelope as a free parameter.

Once the initial model converges, it is evolved through a sequence of discrete time steps. The time step is limited by the condition that the model does not change by more than a small percent anywhere within the model (typically less than 10% in log of radius, pressure, temperature, and luminosity). Evolution away from the ZAHB has a growing convective core, which eventually establishes a region of semiconvection at its outer edge (refer to Figure 1.3). In semiconvection, radiation and convection play comparable roles in transporting energy. This creates some incomplete mixing, establishing a mean molecular weight gradient (normal convection thoroughly mixes the elements, providing a constant mean molecular weight in the convection zone).

As the core converts helium to carbon and oxygen, the star slowly proceeds to lower surface gravity. Once the models have used up all but 20-30% of the core helium (by mass), the star quickly evolves to higher $T_{\rm eff}$. The effective temperature eventually stabilizes and the star evolves to lower log g (larger radius) again as helium shell burning occurs. This is the final phase as an sdB star as it proceeds next to the white dwarf cooling track as helium shell burning is extinguished where it becomes a low mass white dwarf.

Comparison of our evolutionary tracks (such as Figure 1.3) with the model grids of Caloi

(1989) and Charpinet, Fontaine & Brassard (2001) shows close agreement. We note that Charpinet, Fontaine & Brassard (2001) include elemental diffusion and levitation in their atmospheric models while ISUEVO essentially ignores the atmosphere, maintaining the input metallicity.

2.3.2 Pulsation Period Calculation

The stellar models produced by the evolution code provide a complete description of the radial dependence of the structural variables (P, T, and M_r). Through the equation of state, we also obtain the density and other thermodynamic quantities at each shell within the model.

With this "equilibrium" model, we can then calculate the normal mode frequencies for that model. To do so, we use a linear, adiabatic pulsation code that has been applied in a number of other investigations (see Kawaler & Bradley, 1994; O'Brien *et al.*, 1996; O'Donoghue, D. *et al.*, 1998). Further details about the pulsation code used can be found in Kawaler et al. (1985) and Kawaler & Bradley (1994), while the details of pulsation calculations are covered in depth in texts such as Unno et al. (1989) and Hansen & Kawaler (1994). This code solves the perturbed equilibrium equations (in the linear approximation where the perturbations are assumed to be small compared to the values themselves). In this limit, the perturbations can be expressed in terms of one another, and the equilibrium quantities. The details of the techniques for solving the perturbation equations are beyond the scope of this work, so suffice to say that the equations pose an eigenvalue problem. For each eigensolution there is a set of eigenfunctions (that describe the perturbations of the structural quantities as a function of position) and an eigenvalue that corresponds to the frequency of the eigenmode. The set of eigensolutions are indexed by the quantum numbers n and ℓ which were defined above.

We neglect the thermal perturbations by assuming that the pulsation motions are adiabatic; that is, there is no heat lost or gained anywhere in the star over the course of a pulsation cycle. This approximation greatly simplifies the calculation, and provides very accurate pulsation frequencies, though it does not illuminate the question of driving and damping of the pulsations.

The output of the pulsation calculations is a table of pulsation frequencies for p-modes and

g-modes for desired values of ℓ and n. In addition, we use the eigenfunctions to calculate the value of the rotational splitting coefficient $C_{n\ell}$.

2.4 Practical Implications of Pulsation Theory

The last section described the phenomenological aspects of pulsation theory. Yet the theory would be useless were there not observational consequences. In asteroseismology, there is a clear and direct contact between theory and observation in the pulsation periods. This section discusses the observability of the pulsations, the ways we can view the observed periods in light of the theoretical expectations, and limitations of our observational tools.

2.4.1 Observable ℓ Values

To the naked eye, our Sun appears steadily lit from our vantage point on Earth. However, it is also a variable star. Indeed it holds the record for the most pulsation modes observed in a star. It both appears steady, yet pulsates in an abundance of modes because it pulsates in with large ℓ values (see Figure 2.3). As ℓ increases, so do the number of nodal lines, and hence the number of alternating hot/cool or bright/dim regions on the surface of the star increases. In the absence of limb darkening, modes with $\ell \geq 3$ can only be observed if the stellar surface is resolved. Since we can resolve the surface of our Sun, we can observe pulsation modes of large ℓ. However, in every other star, it is difficult to observe modes with $\ell \geq 3$ because of the cancellation effects (Dziembowski, 1977). As such, it is typically irrelevant to match observed periods with model periods of high ℓ value.

2.4.2 Pattern Matching

Equation 2.2 describes how successive overtones of radial modes would appear as peaks equally spaced in frequency in the temporal spectrum. Similarly, Equation 2.3 indicates that nonradial p-modes of successive n or ℓ would also appear equally spaced in frequency (with modes of successive ℓ spaced half the distance of those of successive n). In both cases modes of successive n (but same ℓ) should be spaced in frequency by ν_o while modes of successive ℓ

but same n should be spaced in frequency by $\nu_o/2$. For g-modes, Equation 2.4 dictates that stars of a given ℓ should have equal period spacing with successive n by

$$\Delta\Pi = \frac{\Pi_o}{\sqrt{\ell\,(\ell+1)}}\,. \tag{2.12}$$

In the best case, we would see a sequence of peaks in the temporal spectrum that follow these simple trends, revealing ν_o (in the case of p-modes) or $\Delta\Pi$ (for g-modes). All that remains is determination of ℓ.

Equation 2.5 describes the amount of separation between peaks in the temporal spectrum due to rotational splitting (m degeneracy) Since successive overtones generally have a frequency spacing larger than that of rotational splitting, it is possible to observe successive overtones of triplets (or quintuplets) equally spaced in period for g-modes or frequency for p-modes.

This kind of "pattern matching" analysis can be very useful for identifying pulsation modes. Once the period spacing is found, we can compare it with spacing found in models to determine the global properties of the star- principally, its mass (Kawaler & Bradley, 1994). This method has proved extremely useful in white dwarf and pre-white dwarf stars with periods evenly spaced in both period (due to successive n values) and frequency (as rotationally split modes) (Winget *et al.*, 1991; Kleinman *et al.*, 1998). Rotationally split modes, equally spaced in frequency from each other are seen in the Sun (Christensen-Dalsgaard & Dziembowski, 2000) and roAp stars (Kurtz *et al.*, 1989).

2.4.3 Abundance of Pulsations

Classical pulsators, such as the Cepheid variables described in the introduction typically pulsate in a single mode. Equation 2.1 describes how we can relate even a single pulsation to physical conditions of stars; in this case the average density. However, as described in §2.2.5, modes with nodes placed at different depths within the star "feel" different sized resonant cavities (perhaps due to chemical stratification). Thus, the more observed modes of pulsation, the more interior regions are probed by the pulsations. Thus the stars that are the most sensitive probes of stellar interiors are those with the most pulsation modes.

The richest sdB pulsator shows close to 55 separate periodicities in its temporal spectrum, while others may pulsate in no more than 2 or 3 modes. Over the class, the pulsation periods range from ~90 to 530 seconds with amplitudes typically less than fifteen millimagnitudes. So while the pulsations in our Sun place tight constraints throughout its interior we cannot expect sdB pulsations to be quite as stringent. However, we can still hope to discern some fundamental properties, such as the hydrogen layer thickness and the core composition.

2.4.4 Measuring Evolutionary Changes

Section 2.2.3 discusses how pulsation periods are expected to slowly change over time as the structure of the star changes. We measure this by comparing the observed times of maxima (O) in the light curve to the times of maxima calculated (C) using an assumption of constant period. Any change would then show up in a plot of $(O - C)$ versus time as a phase drift. A constant rate of period change shows up as a quadratic term with time:

$$(O - C) \approx \frac{1}{2}\frac{1}{\Pi_{t_o}}\frac{d\Pi}{dt}(t - t_o)^2 \; [seconds] \tag{2.13}$$

where Π_{t_o} is the period at time t_o (see for example, Kepler *et al.*, 2000a and $d\Pi/dt$ is often referred to as $\dot{\mathrm{P}}$ (P dot).

If the assumed period is incorrect ($\Pi = \Pi_{true} + \delta\Pi$), this will be evident as a linear trend in the (O - C) diagram. If the star is in a binary, its orbital motion may appear in the (O - C) as a periodic (sinusoidal) signal with the amplitude equal to the light crossing time of the orbit (with a dependence on the inclination of the orbit). Chapter 3 will examine how binarity affects the (O - C) diagram.

These changes (evolutionary and perhaps orbital) in (O-C) can be fast enough so as to be measurable in only a few years of observations (see §6.3). This requires that the pulsation period be known to high precision. Enough data must be obtained to secure the pulsation period and phase accurately enough to cover the time between data runs. The accuracy must be such that much less than one-quarter cycle in accrued errors has occurred between runs. If the gap is larger than this, then the number of pulsation cycles will be ambiguous.

Also, it is imperative that the pulsation mode be stable in amplitude over time. If the mode disappears, there is no guaranteeing that it will return with the same phase; though this is possible for modes where the amplitude decreases due to mode beating, only making the mode seem to disappear. For stars where the pulsation appear to be driven stochastically, there is little hope of determining $d\Pi/dt$ ($\dot{\mathrm{P}}$).

The mode also needs to be clearly separated from other modes so that resolution problems are minimal. Shorter time series data sets do not resolve separate, but closely spaced pulsations. As such, the peak in the temporal spectrum can appear to wander (depending on the amplitude stability) in frequency between the two modes, taking the phase with it.

2.5 Successful Applications of Asteroseismology

We know stars pulsate because we can observe them doing so, but we have not yet addressed how to interpret such observations in a meaningful way. We will discuss that now.

As discussed in §2.3 stellar models are crucial in extracting the underlying stellar structure from the observations. To connect the models with observations, we need to measure the stellar pulsation period and, somehow, identify the quantum numbers for the observed modes. Of course the method used to do this depends on the individual or group of stars in question and the available pulsation behavior. The theoretical aspects point to several features to look for in the data (described in §2.4). Here, we give some past examples of successful applications of these techniques of asteroseismology of evolved stars.

2.5.1 A Single, Rich Pulsater

With identified values of n, ℓ, and m in the data, we can convert this into an understanding of the physical nature of the star. For an excellent example, consider the remarkable star PG 1159-035 (hereafter PG 1159), a pulsating pre-white dwarf star. PG 1159 was observed by the WET in 1989 and revealed a rich pulsation spectrum (Winget *et al.*, 1991), a portion of which is shown in Figure 2.4. Three of the many triplets of successive overtone are easily seen in the figure; they provide both a rotation period (from the frequency splitting of the triplets)

and an ℓ identification (from the fact that we see triplets). Quintuplets were also observed, allowing identification of modes with more than a single ℓ value.

Over the course of this single WET run, over 100 separate modes were resolved (Winget *et al.* 1991). With so many identified modes, static and evolutionary models were tightly constrained providing a wealth of physical parameters including $M_{PG\ 1159} = 0.59 \pm 0.01\ M_{\odot}$, and Π_{rot} =1.38 days. From the trapping period, seen in both the $\ell = 1$ and $\ell = 2$ modes, Kawaler & Bradley (1994) were able to determine the helium layer thickness to be $3 \cdot 10^{-3} M_{\odot}$, $\log g = 7.38 \pm 0.1$, $\log L/L_{\odot} = 2.29 \pm 0.05$, and a surface helium abundance of about 30%. Similar analyses have been successful for the DB star GD 358 (Winget *et al.*, 1991; Bradley & Winget, 1994) and for another PG 1159 star, PG 2131 (Reed, Kawaler, & O'Brien, 2000). The work by Reed, Kawaler, & O'Brien (2000) provided an independent check of asteroseismological results using HST photometry, proving the method works.

2.5.2 A Single Star, Viewed Over Several Seasons

Unfortunately, stars like PG 1159 are the exception rather than the rule. Many of the pulsating white dwarfs have complicated pulsation patterns that come and go on timescales of days to years. Fortunately, pulsation theory demands that modes must appear at a limited set of frequencies; they cannot appear at just any frequency. If assembled over a period of years, it may be possible to make sense of the complex pattern and identify modes (Kleinman *et al.* 1998). Figure 2.5 shows how individual pulsation spectra from different times can be combined to present a well-defined pulsation spectrum. Kleinman *et al.* (1998) used this data to place limits on the mass and H layer thickness for the cool DA white dwarf G29-38. Similar techniques produced excellent results for the pulsating central star of NGC 1501 (Bond *et al.*, 1996).

2.5.3 Using an Ensemble of Pulsators to Identify Pulsation Modes

As rewarding as it is to reveal the innards of individual stars, it is important to understand the nature of an entire class of pulsators. In so doing, we can hope to understand stellar

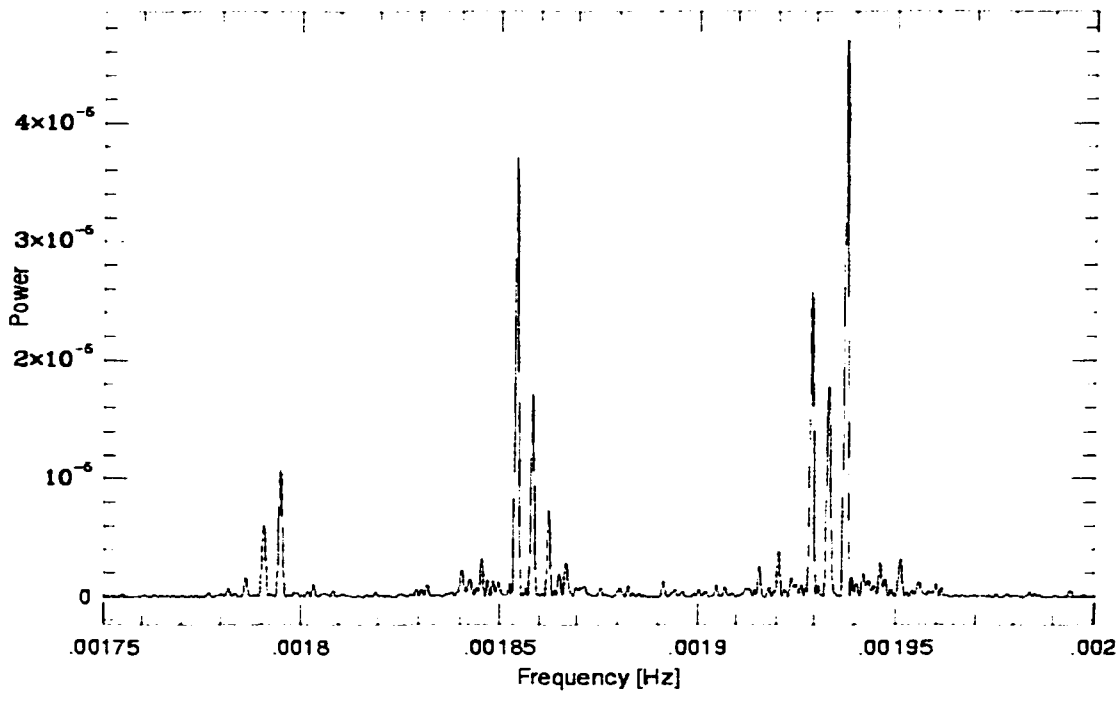

Figure 2.4 A portion of the Fourier transform of PG 1159 data from the 1989 WET campaign. (From Winget *et al.* 1991)

evolution, one class at a time. In addition, individual stars may not have rich enough pulsation spectra to be useful on their own. By combining the spectra from many similar members of the class, correcting for their differences when possible, can produce a "group spectrum" of some use. This work was pioneered by Clemens (1994b) who used the hot ZZ Ceti stars to identify the pulsation modes present in the group. He inverted the problem to determine the properties of individual members. A summary figure is show in Figure 2.6 for his sample of hot DA pulsators. The combination spectrum show period grouping indicative of a fundamental similarity of structure of these stars. If sdB stars have a common underlying structure, then this method should reveal it. It will be attempted in Chapter 7.

O'Brien (1998) used the group properties of pre-WDs to determine the driving region of pulsations, and studied a single member to shed some light on neutrino physics.

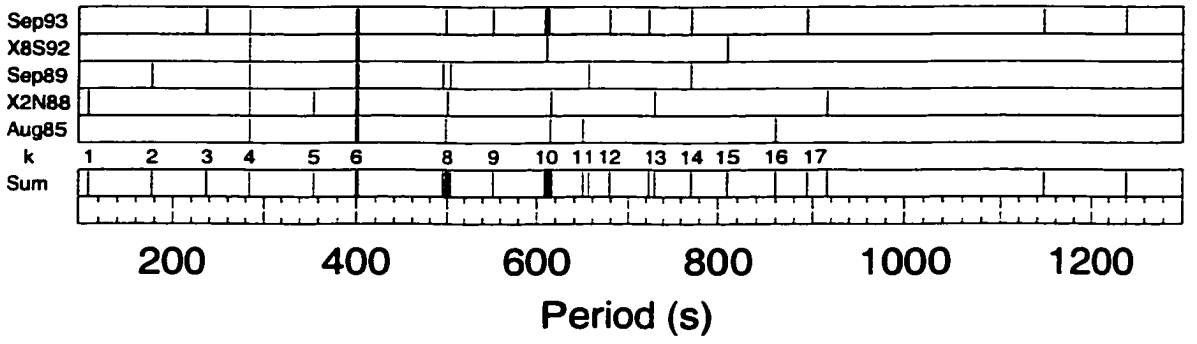

Figure 2.5 Pulsation spectra for G29-38 taken over the years, and summed at the bottom. Note: Linear combinations of modes have been removed. (From Kleinman *et al.* 1998).

2.5.4 O-C

In §2.2.5, I introduced the idea that pulsations can be useful indicators of evolution (manifested as changes in structure) in stars. As stars fuse elements into larger ones, they change their mean molecular weight. Their structure must respond to this change. Likewise, stars that are not undergoing fusion, either just cooling (as in white dwarfs) or deriving their energy from contraction (T Tauri or red giant stars), are continually adjusting their structure to account for temperature or (core) radius changes. These changes are reflected in the pulsations.

Just as changing the liquid level in a glass would change the tone when you tap it, stellar pulsations respond to structural changes due to stellar evolution. In white dwarfs, which are no longer fusing material, there are two dominant processes of structural change; cooling (since we can see them, they are radiating their energy off into space), which increases the degeneracy and contraction, which changes the radius (and thus density) of the star.

Observations have confirmed these predictions in at least one case. Kepler *et al* (2000) began observing G117-B15A, a white dwarf star, in 1975. Over the last 25 years, some of the pulsation periods for G117-B15A have remained steady enough to allow a useful measurement of the rate of period change with time ($\frac{d\Pi}{dt}$ or $\dot{P}$). Their results indicate that the dominant, 215 second pulsation mode is changing at a rate of $(12.0 \pm 3.5) \times 10^{-15} s\, s^{-1}$; in good agreement with theory. By comparing the observed $\dot{P}$ to those predicted by models, they add an additional

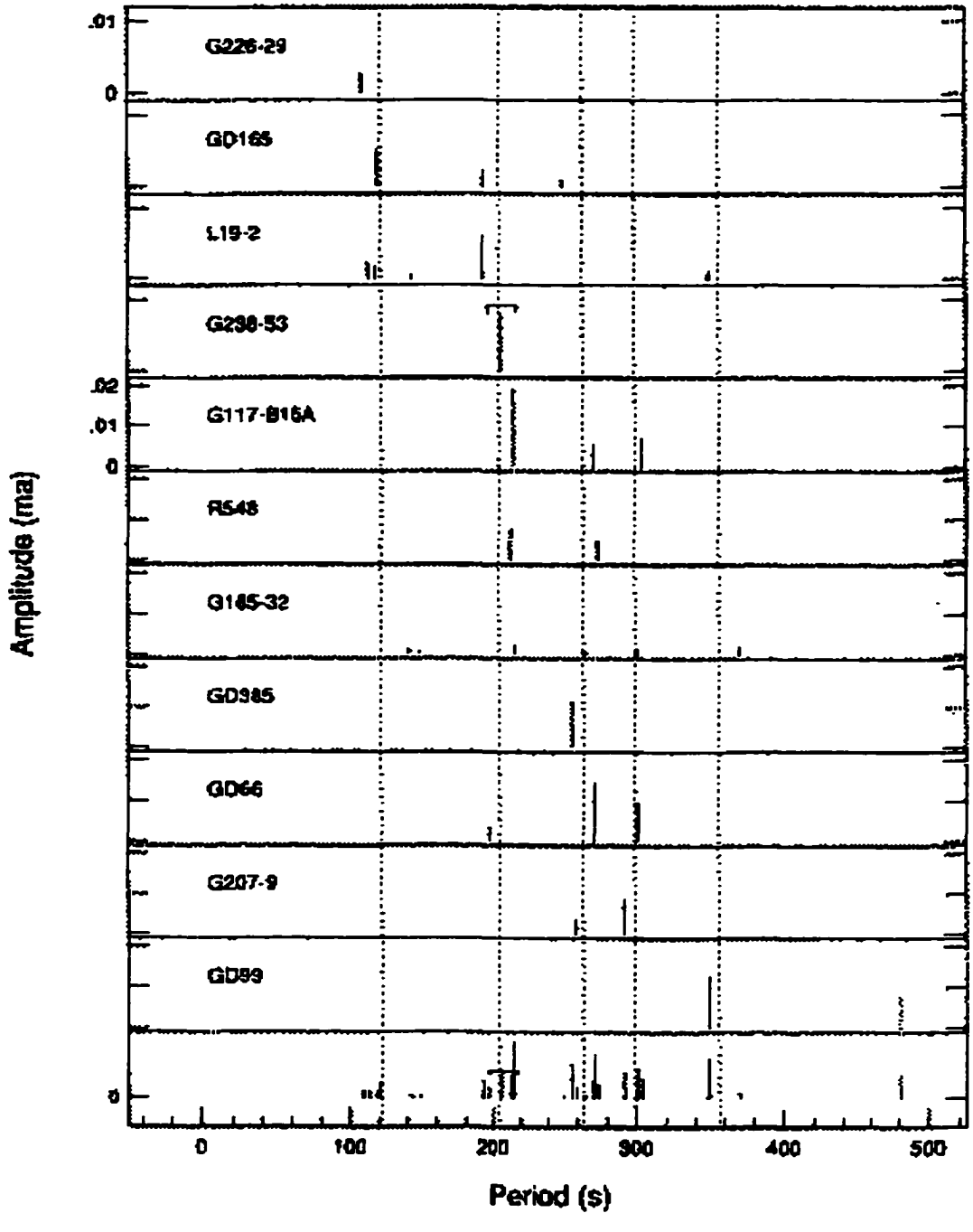

Figure 2.6 Pulsation spectra for individual stars, summed at the bottom. (From Clemens, 1994b)

constraint on the model. This allows them to constrain core composition as well as the overall mass of G117-B15A. In Chapter 6, we will use this technique to place limits on the evolutionary timescale of Feige 48.

2.6 Conclusions

In this section, I described the observational methods and interpretation tools of asteroseismology that I use in my investigations of the sdBV stars. To review, this chapter:

- Provided an overview of how data are obtained using photoelectric photometers.
- Outlined the process of data reduction to produce light curves
- Introduced the temporal spectrum.
- Described the employment of multi site and extended timebase observations to minimize aliasing and increase frequency resolution.
- Outlined pulsation theory and introduced radial modes and nonradial p- and g-modes.
- Discussed the consequences of rotation, elemental stratification, and evolution on the temporal spectrum.
- Described the calculation of detailed stellar models and their pulsation analysis for comparison with observation.
- Showed the close contact between theory and observations: observable frequency and period spacings as indicators of pulsation mode and stellar properties.
- Provided examples of successfully applying pulsation theory to observations to constrain the overall mass, mass composition layers, core densities, and evolution, which can also constrain radius and luminosity.

The rest of this thesis will describe how I investigated sdB stars using the tools discussed in this chapter, and some new tools needed for these stars

CHAPTER 3. SUBDWARF B STARS AS BINARIES

In this chapter, we will apply a perturbation to the tools of asteroseismology outlined in Chapter 2. We will examine the consequences of binarity on pulsations. Though concentrating on sdB stars, the procedures developed here can apply to any pair of stars with similar orbital parameters and pulsation periods. I begin with a review of the frequency and parameters of observed binary sdB stars. Section 3.2 simulates how the observed pulsations are affected by binary motion; Section 3.3 discusses special cases, such as eclipsing binaries or binaries where tidal forces affect the pulsation axis.

3.1 Observed Subdwarf B Stars in Binaries

3.1.1 Methods of Detecting Binary Stars.

As mentioned in §1.2.2, sdB stars are commonly observed in binaries. These binaries are most often detected as composite spectrum binaries, spectroscopic binaries (i.e. radial velocity variations) and/or through infrared color excess. In this subsection we briefly review those three methods.

Subdwarf B stars in composite spectrum binaries show not only the expected hot continuum and Balmer series, but quite often the calcium H and K lines. These latter lines are indicative of a cool companion as they involve metallic ionization states that cannot exist at temperatures common to sdB stars. Composite spectrum binaries do not provide the orbital period of the binary, but do indicate parameters for the companion star (such as $T_{\rm eff}$ and $\log g$).

Radial velocity variations, the hallmark of "spectroscopic binaries," show periodic Doppler shifting. Such binaries can be detected whether spectral lines are seen from the companion or not. Spectroscopic binaries are very useful as they provide the orbital period and velocity

(though the velocity is reduced by the sine of inclination of the orbit). Section 3.2.2 shows how we can use pulsations in sdB stars as a new variation on the "radial velocity" theme.

The last method uses photometry (typically CCD). It is similar to the *composite spectrum* method in that it detects companions via their contribution to the radiated flux of the pair. For sdB stars, this is best done by comparing the observed flux in the blue to that in the infrared. Binaries show up as a "color excess" (typically to an excess of flux in the infrared) as compared to sdB stars with no companions, with the red excess coming form the later-type companion. Since all of the cases discussed here involve infrared imaging, we will refer to such binaries as *infrared excess binaries.* It should be noted that this method provides only the crudest of information (relative flux and color) for the companion. In fact, it does not even guarantee that the pair is a physical binary rather than a superposition of two line-of-sight stars. However, it is a much quicker and easier test to complete for a large number of stars (over which the number of pairs of a chance alignment drops appreciably).

Another method deserves brief mention. In lucky instances, an sdB star may be in an eclipsing binary. Eclipsing binaries occur when the orbital plane of the stars lies along our line-of-sight and the observed flux is periodically diminished as one star passes in front of the other. To date only two binary sdB stars (HW Vir and PG 1336-018) have been detected via this method, which is why we will not include them here, but will briefly mention them as special cases in §3.3. One of them, PG 1336-018, is the subject of Chapter 8.

3.1.2 Binary Frequency of Subdwarf B Stars

One of the first searches for binary sdB stars was conducted by Ferguson, Green, Liebert, & Saffer (1984; who were actually looking for a different kind of binary). From their detection of 24 composite-spectrum binaries, they inferred that ~35% of all sdB stars have main sequence companions between spectral types G8 and K5 (the stars to which their work was sensitive).

O'Donoghue *et al.* (1999) determined that 4 of the first 9 pulsating sdB stars were composite spectrum binaries with F and G type main sequence companions. Their detections are what would be expected for observations of random sdB stars using the results from Ferguson, Green,

Liebert, & Saffer (1984)

Maxted, Marsh, & North (2000) searched for short period spectroscopic binaries over a seven day period in 2000. They infer that 60±8% of sdB stars are in binaries with orbital periods less than ten days. However, none of their spectroscopic binaries were composite spectrum binaries, which means that the companions are not luminous compared to the primaries. Such companions are likely white dwarfs, but may also include some late-type main sequence stars.

Green, Liebert, & Saffer (2000) have searched the largest sample sdB stars for radial velocity variations; they are also the only ones to have obtained data spanning multiple years (typically two). From their work, they find that ~20% of their sample are composite spectrum binaries, with radial velocity variations indicating orbital periods averaging 3 - 4 years. Another ~45% are short period spectroscopic binaries, but not composite-spectrum binaries. The number of short period binaries is in rough agreement with Maxted, Marsh, & North (2000).

Ulla & Thejll (1998 and references therein) searched for infrared excess binaries using 4 different filters. They determined that 44% of their sample (39 of 88 sdB stars) had main sequence companions with spectral types from A to early M. This number is in agreement with that of Ferguson, Green, & Liebert (1984), who had a slightly more selective sample.

Using the *Two Micron All Sky Survey* (2MASS), Reed & Steining (*in preparation*) examined the most complete sample to date: 492 subdwarf B stars. From this sample[1], we determine that 40±4% of sdB stars are infrared excess binaries with main sequence companions between late A and early M. This is in agreement with Ulla & Thejll (1998) and Ferguson, Green, & Liebert (1984).

Four works clearly agree that ~40% of sdB stars have main sequence companions (Reed & Steining, *in preparation*; O'Donoghue *et al.* 1999; Ulla & Thejll, 1988; Ferguson, Green, & Liebert, 1984). However, none of these works can parameterize the distribution of the binary properties (i.e.. period or separation). The only work to address the orbital parameters of sdB+MS stars is Green, Liebert, & Saffer (2000) though they only detected ~20% of sdB+MS pairs. Still, Green, Liebert, & Saffer (2000) agree with the results of Maxted, Marsh, & North

[1]Detailed in Appendix A.

(2000) in that none of the short period spectroscopic binaries in their samples have main sequence companions between A and M. However, Jeffery & Pollacco (2000) observed two pulsating sdB stars and noted that one of them (PB 8783) is a composite-spectrum binary showing possible radial velocity variations with a period between 0.9 and 3 days. This is the only known case of a main sequence star (early than M) in a short period binary.

Based on the radial velocity completed to date, we conclude that ~60% of sdB stars are in short period binaries. From infrared observations (especially our work in Appendix A), we believe that ~40% are in binaries (probably longer period) with a main sequence companion. From this, we should expect that the vast majority (~100%) of sdB stars are in binaries.

3.1.3 Theoretical Considerations

With such a high binary frequency, the role of binarity in *producing* sdB stars has drawn interest of theorists. For example, Sandquist, Taam, & Burkert (2000), using evolutionary models, evolved pairs of stars drawn from a distribution of masses and periods on the main sequence until the more evolved star reached the horizontal branch. They noted that for a range of companion mass and orbital separation, the horizontal branch star was an sdB star produced through enhanced mass loss while a common envelope binary. The post-common envelope sdB typically had a main sequence companion with a mass slightly less then our Sun (with a range from 0.5 - 2.3 $M_{\odot}$) and a separation of 10 solar radii (with a range from 0.15 to 35 $R_{\odot}$), having orbital periods between ~5 hours ~5 days. Thus they were able to produce sdB stars in short period binaries with main sequence companions.

As part of their research, Green, Liebert, & Saffer (2000) suggest two methods to produce sdB stars via binarity. The first would be to have a fairly wide initial orbital separation between two main sequence stars. As the more massive star evolved, it became a red giant. Just as it began burning helium in the core, it went through a period of extreme mass loss enhanced by its companion. What remained was an sdB+MS binary with a long period (on the order of a few years) orbit. In their second scenario, the stars start closer together and the red giant loses its envelope to the companion before helium fusion can occur and becomes a helium white

dwarf. When the companion becomes a red giant, it becomes a common-envelope binary with its helium white dwarf companion. This common-envelope binary is able to eject the envelope after core helium burning commences. The system is left with a sdB+WD in a short period binary. Green, Liebert & Saffer's (2000) scenarios are able to produce sdB stars either with main sequence companions in long period orbits, or with white dwarfs in short period orbits.

3.2 Effects on Pulsation Due to Binarity

Considering the high probability that an sdB star has a close companion (4 of the first 9 pulsating sdB stars discovered are composite spectrum binaries), this section explores what happens to pulsations, as we observe them, of an sdB star in a binary. We now know that it is reasonable to assume that *many* sdB stars are in binaries. The effects examined here are just the consequence of orbital motion on our timing of the observed light variations. We do not address the physical effects of the companion, but will defer that to later in this thesis.

3.2.1 Time Delay and Doppler Shift

As stars orbit each other in a binary, they move around their common center of mass. If the inclination of the orbital axis to our line of sight i is not 0, then the star's distance from us will change. As the star's distance is changed, the time it takes for its light to reach us is changed. This time will increase (decrease) if the star is further away (closer) than the center of mass by the time it takes the light to cross the orbit,

$$t_{delay} = c \cdot R \sin i \tag{3.1}$$

where c is the speed of light and R is the radius of the orbit. This is depicted in Figure 3.1, where points B and D are at the center of mass distance, point A is the closest the star approaches the observer, and point C the furthest away the star gets from the observer.

Thus the time it will take any pulse of light to arrive will be

$$\tau = cd + t_{delay} \sin\left(\frac{2\pi t}{\Pi_{orb}} + \phi_{orb}\right) \sin i \tag{3.2}$$

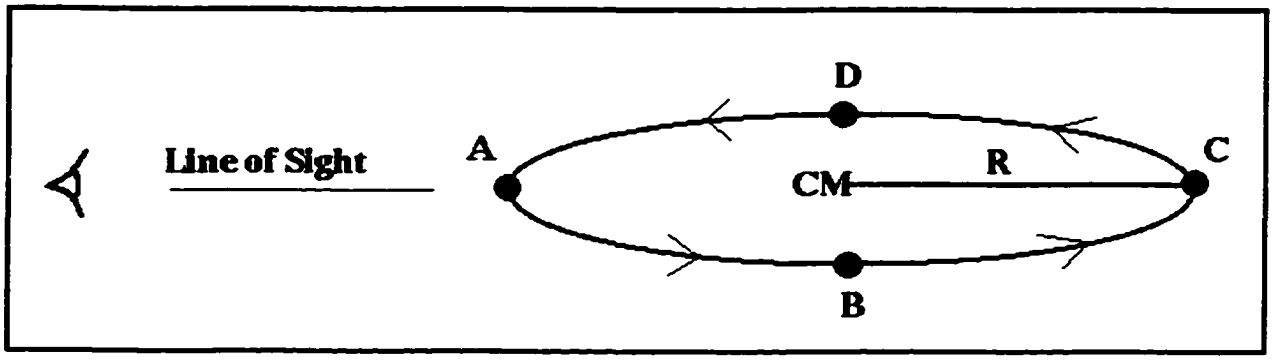

Figure 3.1 Depiction of one orbit in a binary system for an inclination of 90^o as viewed along the light of sight. At point A, the star is closest to the observer, at B, at the same distance as the center of mass and moving away from the line of sight, at C, furthest from the observer, and at D, at the same distance of the center of mass again, but moving toward the line of sight.

where d is the distance from the observer to the center of mass, and ϕ_{orb} is an arbitrarily chosen orbital phase. Since the distance across the binary orbit is much smaller than the distance to the star from Earth, (any periodic signal being sent from such a star would have its arrival time varied by

$$\Delta\tau = t_{delay} \sin\left(\frac{2\pi t}{\Pi_{orb}} + \phi_{orb}\right) \sin i\,. \tag{3.3}$$

To determine what this would do to pulsations, we simulated light curves by taking a sinusoidal variation of the form:

$$\frac{\Delta I}{I} = 1 + A \sin\left(2\pi t f + \phi\right)\,, \tag{3.4}$$

and varying the arrival time of the signal by $\Delta\tau$. This is depicted by a segment of a noiseless simulated light curve in the top panel of Figure 3.2.

Of course what we really wish to know is how the delay time manifests itself in the temporal spectrum. The bottom panel of Figure 3.2 shows the temporal spectrum for six hours of noise-free data; a portion of which is shown in the top panel. The input frequency was 5650 μHz (177 seconds), but is not even the largest peak in the FT. This is an exaggerated example, with $\Delta\tau$=2 minutes in a 30 minute binary, but illustrates the potential effect. For real binaries, the effect will be much more subtle, as we show in §3.2.3.

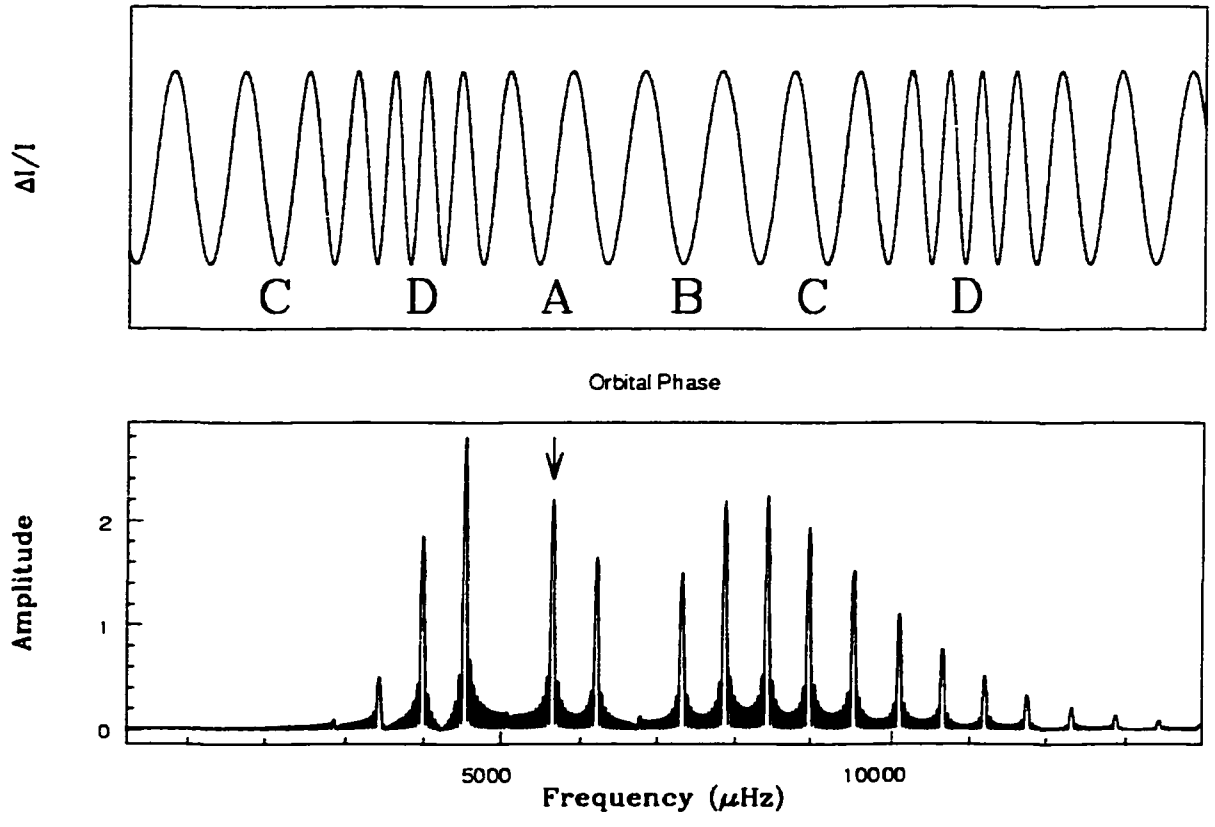

Figure 3.2 Top: One hour segment of a simulated, noiseless light curve. The star is closest to the observer, at B, at the center of mass, and at C, furthest from the observer. Bottom: Temporal spectrum (FT) of the complete (6 hour) simulated data set. Arrow indicates the input peak. Note: $\Delta\tau$ has been exaggerated to make the shifts more easily seen.

One feature that we can expect from such a binary is a discernible Doppler shift of the pulsation frequency. During each orbit, a star would spend roughly equal times moving toward, and then away from the line of sight. If the light curve is broken into segments with travel in the same direction (either toward or away from the observer), then we would expect the peak to be Doppler shifted by v_{rad}/c. To illustrate this, simulated light curves were calculated (again with exaggerated parameter). The simulated lightcurve included $\Delta\tau$=300 (a number an order of magnitude larger than we would expect to observe from these systems) in a 6 hour orbital period. Figure 3.3 shows the resultant temporal spectra. The Doppler shift is detectable in this noise-free simulation, but *only* when a single orbit is examined. When multiple orbits are combined, the peak in the temporal spectrum returns to the input frequency. This is because the pulsation phase is allowed to "reset" at the completion of each orbit. Thus we expect that this will not be a diagnostic for our data.

3.2.2 *O - C*

The light travel time across the orbit can also be recast as a periodic change in phase of a constant period variation (i.e. Equation 3.2). Thus the phase will change periodically on the $O-C$ diagram. This is actually another way of detecting binaries; especially long period (multiple year) binaries for which we can get a good measure of phase as the duration of observing runs is much less than the orbital period. For low eccentricity orbits, binarity will introduce a sinusoidal variation on the phase of pulsations. Such a variation is detectable in the $O-C$ diagrams described in §2.4.4 and shown in Figure 3.4. In the simulation depicted in the figure, the companion is a 1 solar mass star and the orbital period is 24 days. This method can even detect planets (within the restriction of §2.4.4), whose effect on the star would otherwise be too small to measure.

3.2.3 Complicated Light Curves

As shown in Figure 3.2, orbital motion can result in several peaks from a single pulsation frequency. Since the light travel time across the binary orbit is changing in a periodic manner,

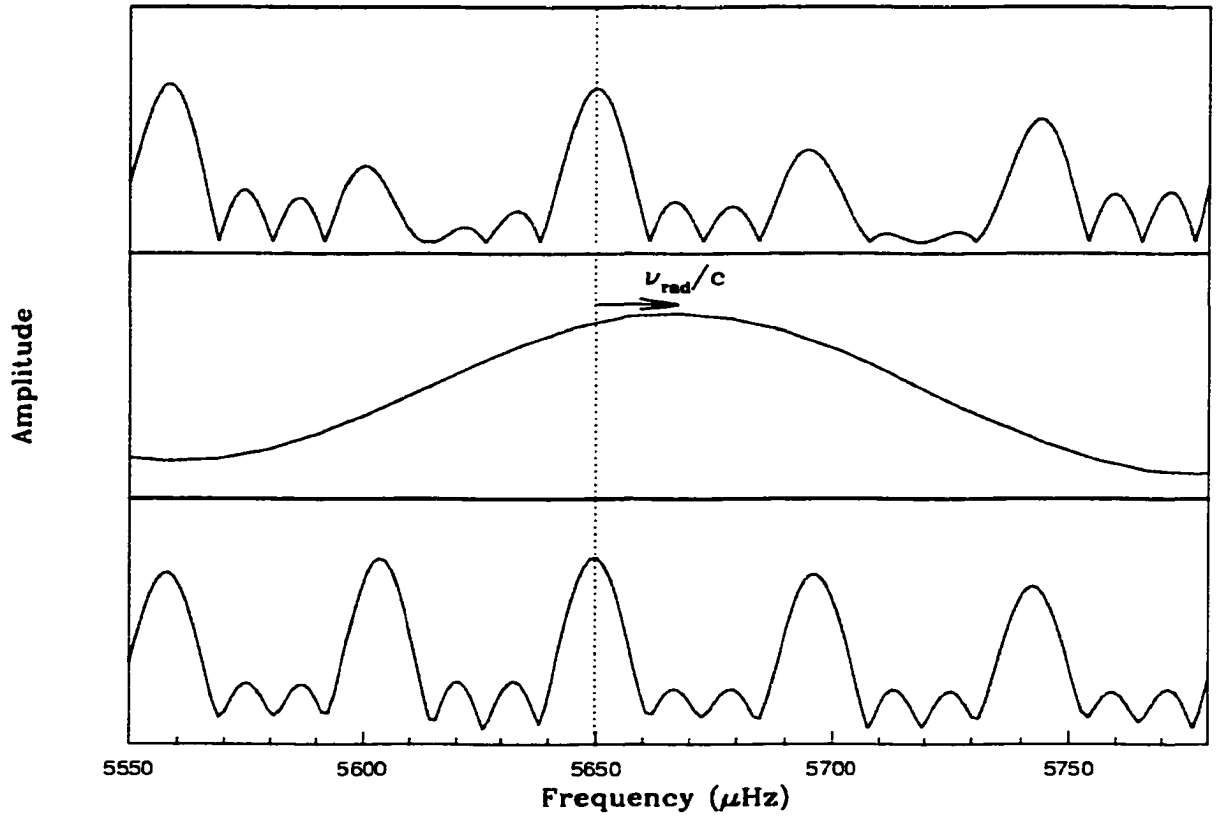

Figure 3.3 Temporal spectra of different groupings of a simulated light curve for a star with a Π_{orb}=6 hours and $\Delta\tau$=300 seconds. Top: FT of the complete 24 hour light curve. Middle: FT of one segment with the star moving away (i.e. near point B in Figure 3.1). Bottom: Segments of multiple orbits with the star moving away from the observer.

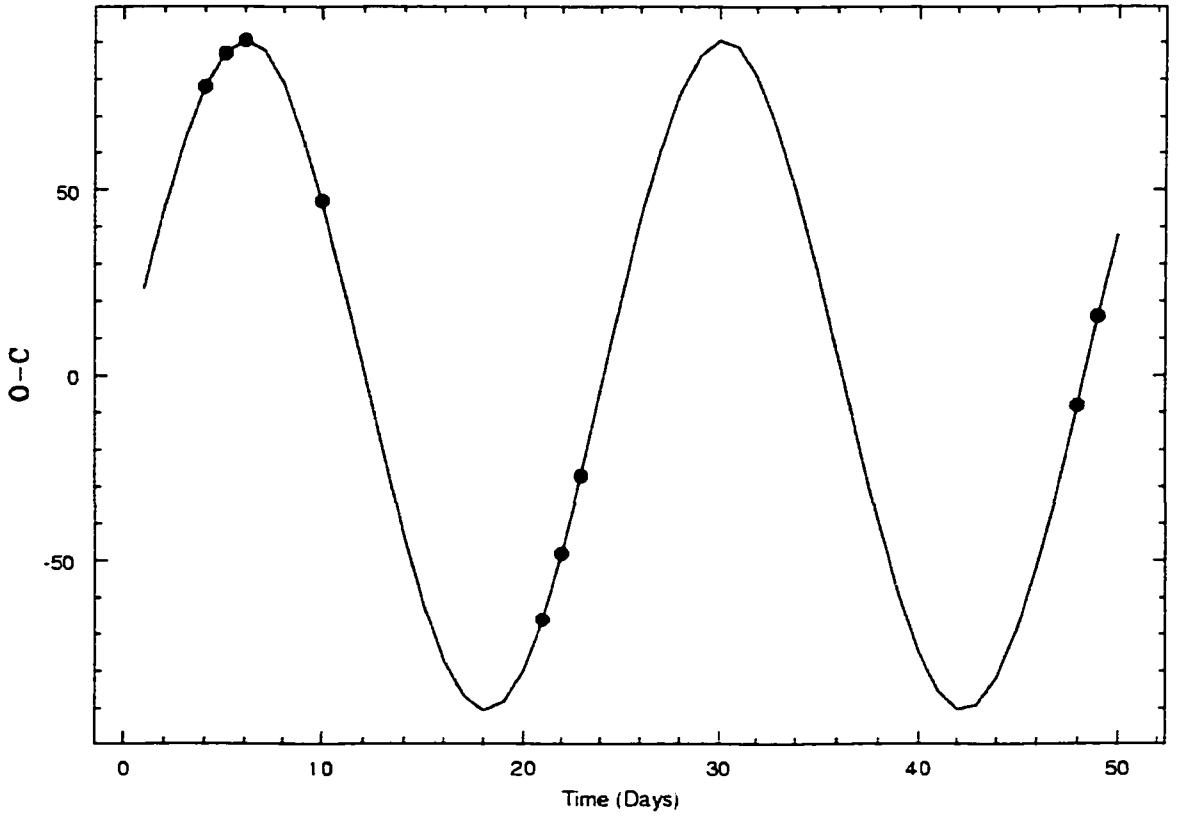

Figure 3.4 Simulated $O-C$ diagram for an sdB pulsator in a 24 day binary with a $1M_{\odot}$ companion. Dots represent "observed" data points.

aliases *can* be produced separated from the real periods by the orbital frequency. As $\Delta\tau$ increases, so does the orbital period. Since these aliases will appear separated from the pulsation frequency as $1/\Pi_{orb}$, as Π_{orb} increases, the separation between the real and the alias peaks diminishes. If the orbital period is much longer than the pulsation period, and exceeds the span of observations, then the aliases lie essentially atop the real pulsation and only a single peak is detected. An orbital period of 6 days produces a $\pm 2\mu$Hz alias; this requires a run of at least five to six days duration to resolve, depending on signal to noise and daily aliasing for single site data.

For short orbital periods (i.e. hours to days), the temporal spectrum will be complicated because of the effects of orbital aliasing. Analytic analysis is possible for these cases, but this problem is well approached through numerical simulations. For the simulations, we assumed an sdB mass of $0.5 M_{\odot}$ and used a range of companion masses and separations based on model results from Ron Taam (private communication); derived for the work of Sandquist, Taam, & Burkert (2000) for theoretical means of producing sdB stars via common envelope evolution on the red giant branch. Figure 3.5 shows the masses and separations used for the simulations plotted over Taam's Monte Carlo results. The binary parameters resultant from the grid are provided in Table 3.1. Column 1 gives our grid number for later reference, columns 2 and 3 provide the companion mass and orbital separation, respectively. Column 4 gives the separation between the input frequency and orbital aliases ($1/\Pi_{orb}$) and the last column gives the light crossing time of the orbit ($\Delta\tau$). Though motivated by Taam's results, this grid represents, in a generic way, the range of binary parameters for sdB stars.

3.2.4 Temporal Spectra of Simulated Data

We consider the case of high inclination to maximize the effect and simplify the discussion; due to geometric considerations (see Figure 2.3 or §6.1.2), at high inclinations the amplitude of the $\ell = 1$, $m = 0$ mode is greatly reduced, whereas the amplitudes of the $\ell = 1$, $m = \pm 1$ modes are maximized. For the relatively short orbital periods of interest, we also assume tidally locked synchronous rotation, so any rotationally split modes will appear close to these aliases (within

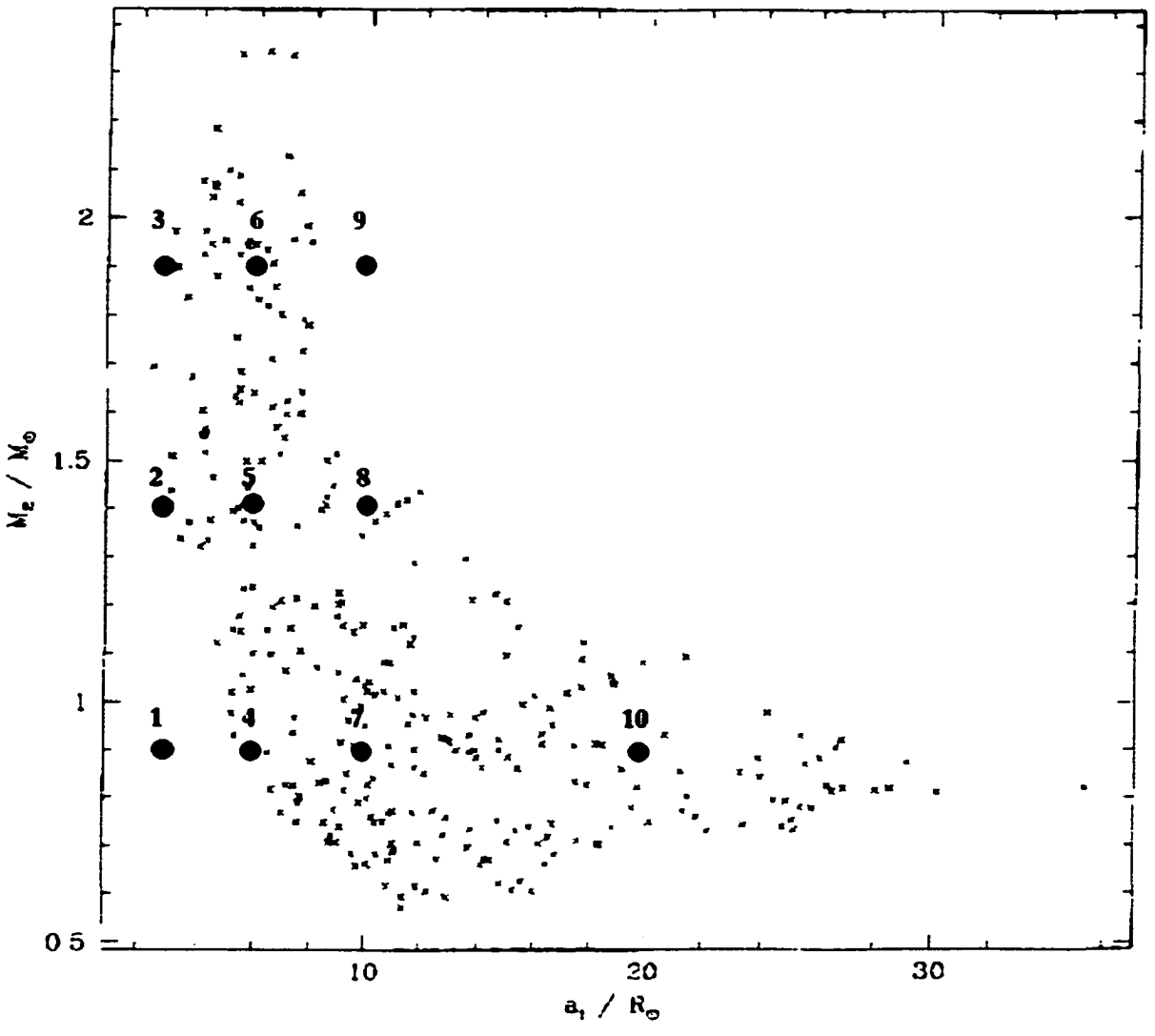

Figure 3.5 Companion parameters (filled circles) plotted over Monte Carlo model results for producing sdB stars through CE evolution. (Courtesy of Ron Taam.)

Table 3.1 Orbital parameters for simulated light curves.

Case	M_2 ($M_\odot$)	a_{sep} ($R_\odot$)	$1/\Pi_{orb}$ (μHz)	t_{delay} (Sec)
1	0.8	3.0	38.7	8.6
2	1.4	3.0	46.8	10.3
3	1.9	3.0	52.6	11.0
4	0.8	6.0	13.7	17.1
5	1.4	6.0	16.6	20.5
6	1.9	6.0	18.6	22.1
7	0.8	10.0	6.4	28.6
8	1.4	10.0	7.7	34.2
9	1.9	10.0	8.7	36.8
10	0.8	20.0	2.3	57.2

Table 3.2 Grouping of data used in simulations.

Group	Run(s)
I	Single 7 hour run
II	7 and 8 hour runs from single site on consecutive nights.
III	7, 8, and 5 hours runs from single site on consecutive nights.
IV	4 days of 2 sight data with ~15 hours of continuous coverage per day
	Multi-site data: From Xcov 18
V	3 consecutive days with 94% coverage
VI	4 consecutive days with 96% coverage
VII	5 consecutive days with 97% coverage
VIII	Entire campaign: 16 consecutive days with ~85% coverage

a few percent; see Equation 2.6). This can make an $m = \pm 1$ pair appear like a quintuplet (including the outer 2 orbital aliases) of each peak and a central peak (see Figure 3.6).

For our simulations, we chose to use realistic sampling times from actual data, but simulated singly-periodic stellar oscillations including Poisson distributed noise appropriate for 1 meter class telescopes. Combination of runs used for sampling times are given in Table 3.2. [2]

As previously described, this effect will be most prominent for high inclinations (increasing $\Delta\tau$) where it is difficult to detect m=0 modes. Therefore we simulated $m = \pm 1$ modes, centered near 175 seconds. The frequencies of the periodic signals (Equation 3.4) are $5714 \pm 1/\Pi_{orb} \mu$Hz along with a reasonable splitting coefficient of 3% according to evolution models (refer to §2.3).

[2]Specific runs for HL Tau76 available at http://wet.iitap.iastate.edu/xcov18/datalog/index.html.

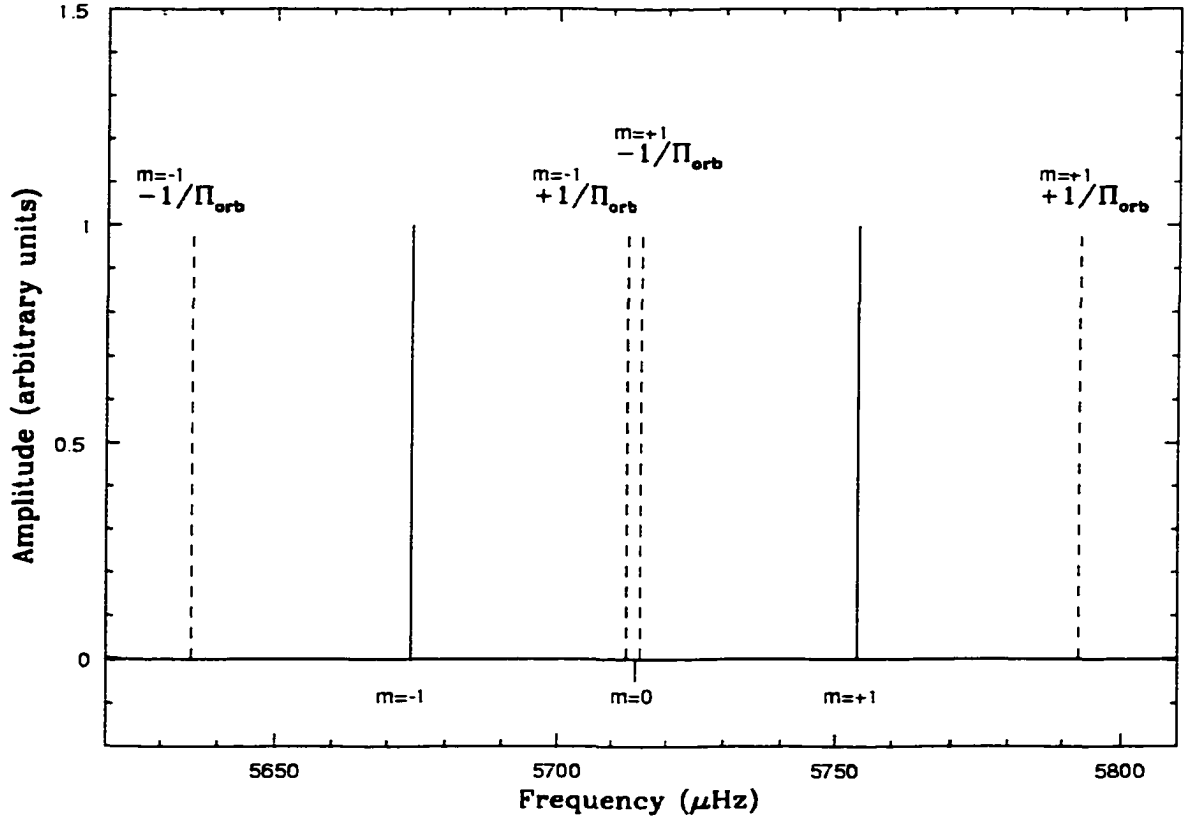

Figure 3.6 Schematic indicating where orbital aliases (dashed lines) will appear when $m = +1$ $[m(+1) = m(0) + \frac{1}{\Pi_{orb}}(1 - C_{n\ell})]$ and $m = -1$ $[m(-1) = m(0) - \frac{1}{\Pi_{orb}}(1 - C_{n\ell})]$ modes (solid lines) are present.

The input amplitude of the simulations are 6 millimags, typical of amplitudes found in sdB pulsators.

Figures 3.7 to 3.11 show the results of our simulations. As expected, if the orbital separation is too small (all the cases for $a_{sep} = 3R_{\odot}$ and most cases for $a_{sep} = 6R_{\odot}$), t_{delay} is small, so the phase is stable enough so that no discernible aliases appear. However, for the larger orbital separations ($a_{sep} \geq 10R_{\odot}$), there can be a significant effect. In Case 10, the aliases (dashed lines) from the two input frequencies (dotted lines) have added together to become a central peak with an amplitude larger than the real variation in the signal. This produces an observed quintuplet. In a traditional asteroseismological analysis, quintuplets would be considered evidence of an ℓ=2 mode, where in fact this is only 2 modes (m=$\pm$1), which can be caused by any $\ell \geq 1$.

Figures 3.7 to 3.11 also make it evident that the *amount* of data plays a key role. For Runs I - III, the daily aliases are so large that the orbital aliases have little or no observational impact. The effect is most prominent in the best overall coverage (Run VIII).

3.2.5 Reducing Data with Orbital Aliasing

To determine how our standard reduction procedure reacts to orbital effects, I reduced individual simulated runs using our standard procedure (as discussed in §2.1). Due to the periodic drift in phase, least squares (LSQ) fitting was seldom successful in recovering the input modes (see Figure 3.12 for an example). After prewhitening the first two input frequencies, peaks typically remained at the original amplitude, shifted by a couple of μHz. There were several cases (especially Case 10VIII) where, after removing the two real periods, there clearly remained a triplet or a quintuplet.

With the presence (real or not) of triplets or quintuplets, the usual interpretation would be rotational splitting, which would then be used to identify ℓ values. Unfortunately, there is no clear signature that points to a binarity-complicated pulsation spectrum. At best, we can conclude that *if* a pulsation spectrum is difficult to fit (using LSQ methods) and/or prewhiten, then binarity *may* be the cause, though intrinsic amplitude variations, frequency variations due

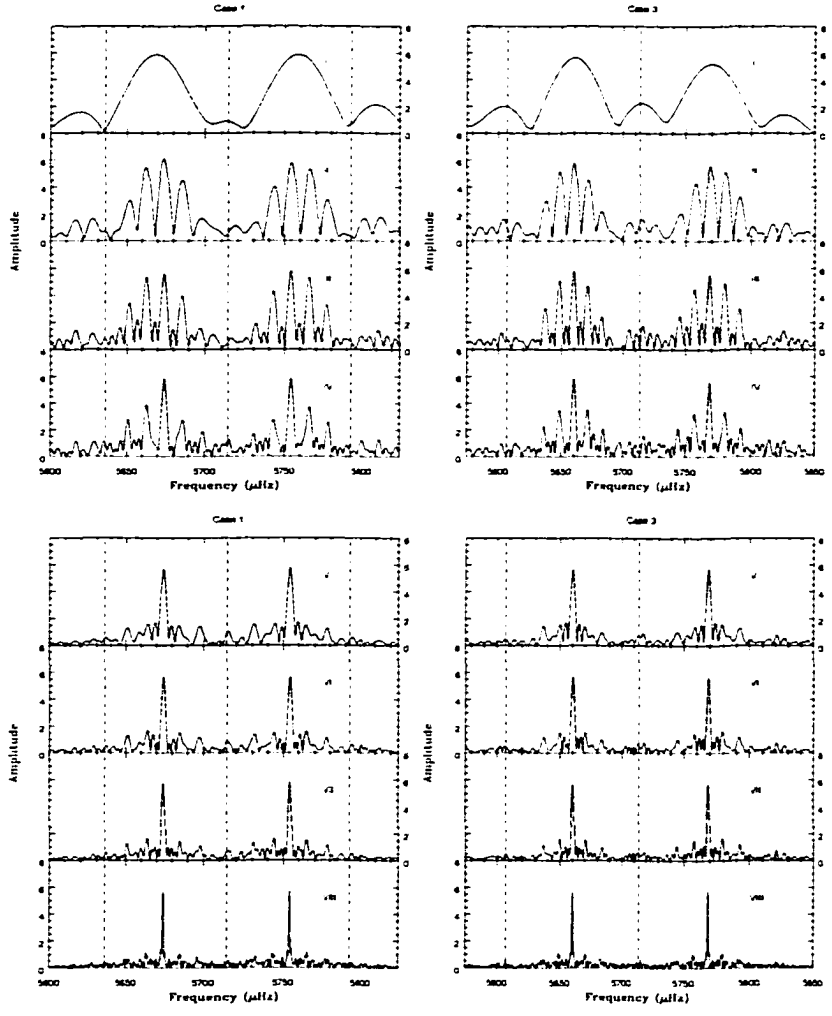

Figure 3.7 Fourier Transform of model light curves for cases 1, left, and 3, right, (a_{sep} = $3R_{\odot}$, M_2=0.8 and 1.9$M_{\odot}$, respectively) as provided in Table 3.1, with numerals corresponding to data sampling in Table 3.2 Dotted lines indicate real pulsation frequencies while dashed lines indicate orbital aliases.

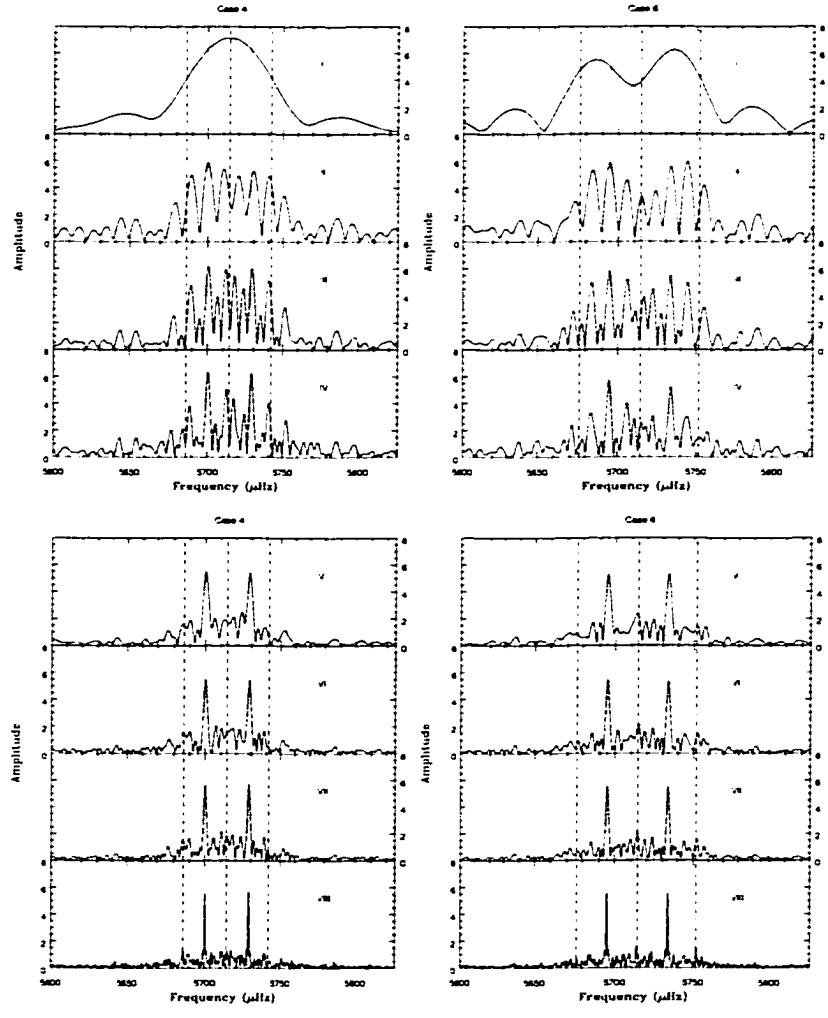

Figure 3.8 Fourier Transform of model light curves for cases 4, left, and 6, right ($a_{sep} = 6R_{\odot}$, M_2=0.8 and 1.9$M_{\odot}$, respectively) as provided in Table 3.1, with numerals corresponding to data sampling in Table 3.2. Dotted lines indicate real pulsation frequencies while dashed lines indicate orbital aliases.

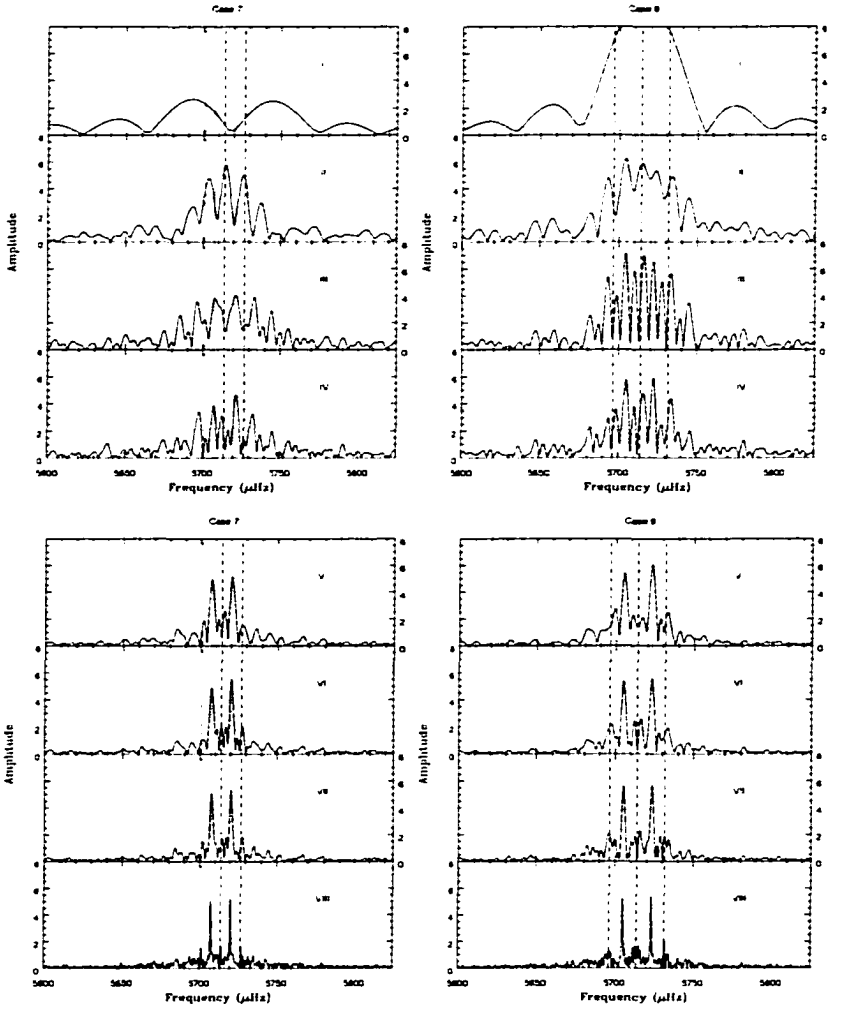

Figure 3.9 Fourier Transform of model light curves for cases 7, left and 9, right (a_{sep} = $10R_{\odot}$, M_2=0.8 and 1.9$M_{\odot}$, respectively) as provided in Table 3.1, with numerals corresponding to data sampling in Table 3.2. Dotted lines indicate real pulsation frequencies while dashed lines indicate orbital aliases.

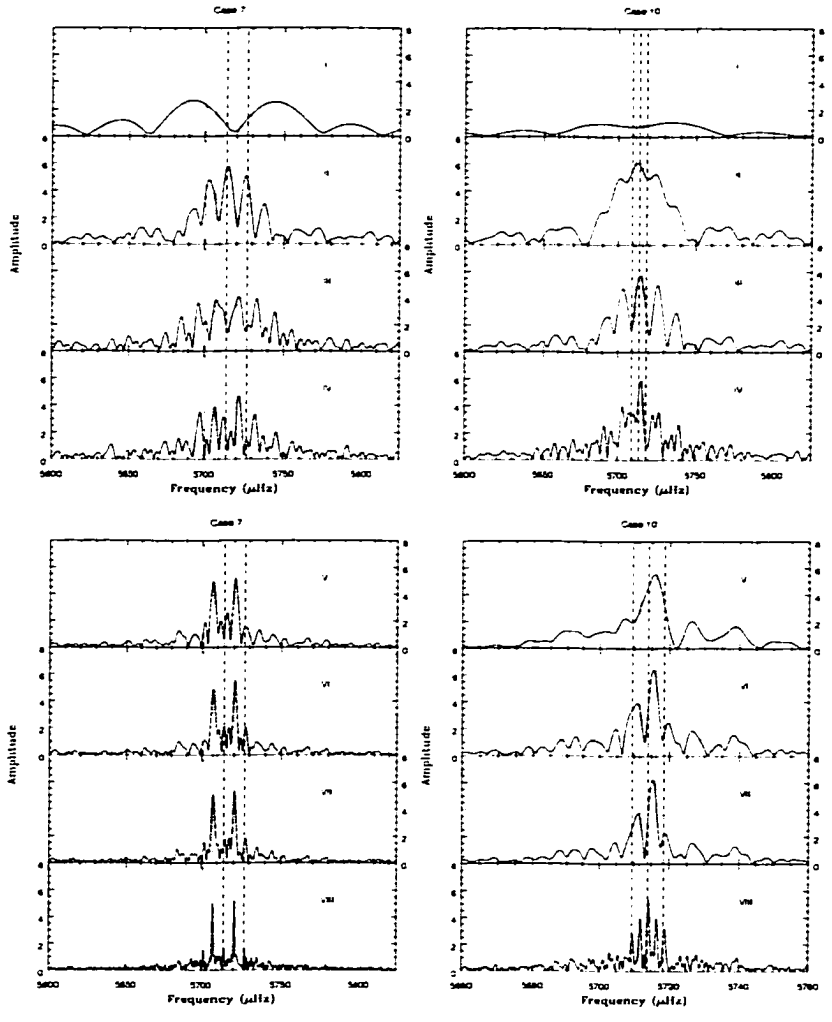

Figure 3.10 Fourier Transform of model light curves of cases 7, left and 10, right (M_2=0.8$M_\odot$, a_{sep}=10 and 20$R_\odot$, respectively) as provided in Table 3.1, with numerals corresponding to data sampling in Table 3.2. Dotted lines indicate real pulsation frequencies while dashed lines indicate orbital aliases.

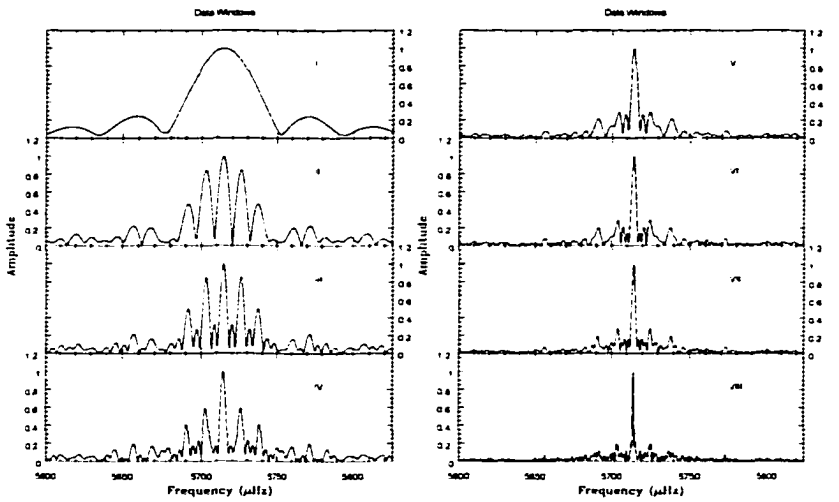

Figure 3.11 Data window functions for a single sine wave for data sampling according to Table 3.2.

to beating periods, or other non-linear effects may also be responsible. Should a complicated pulsation spectrum be detected, investigations into the binary nature of the system *may* be the cure.

3.2.6 Correcting the Lightcurve for Binarity

To determine the orbital period and mass of the companion required to understand a temporal spectrum for a pulsator in a binary, we follow an iterative process, using whatever other information about the target that we have. Since we assume that the primary mass is very close to $0.5M_{\odot}$, the secondary mass and orbital period can be determined from the observed radial velocity variations. With these quantities, the projected light travel time ($\Delta\tau$) across the orbit can be determined. The lightcurve can be corrected by removing a sine wave with amplitude $\Delta\tau \sin i$, with the known orbital period. The orbital phase must coincide for the (arbitrarily set) zero point of the data. Figure 3.13 shows a lightcurve (Case 10VIII) before and after the lightcurve was corrected to account for the changing phase induced by the orbital light travel time.

In this example, we assumed we knew the orbital period and size. In principal, if we have only limits, a multiparameter non-linear χ^2 minimization procedure could determine these

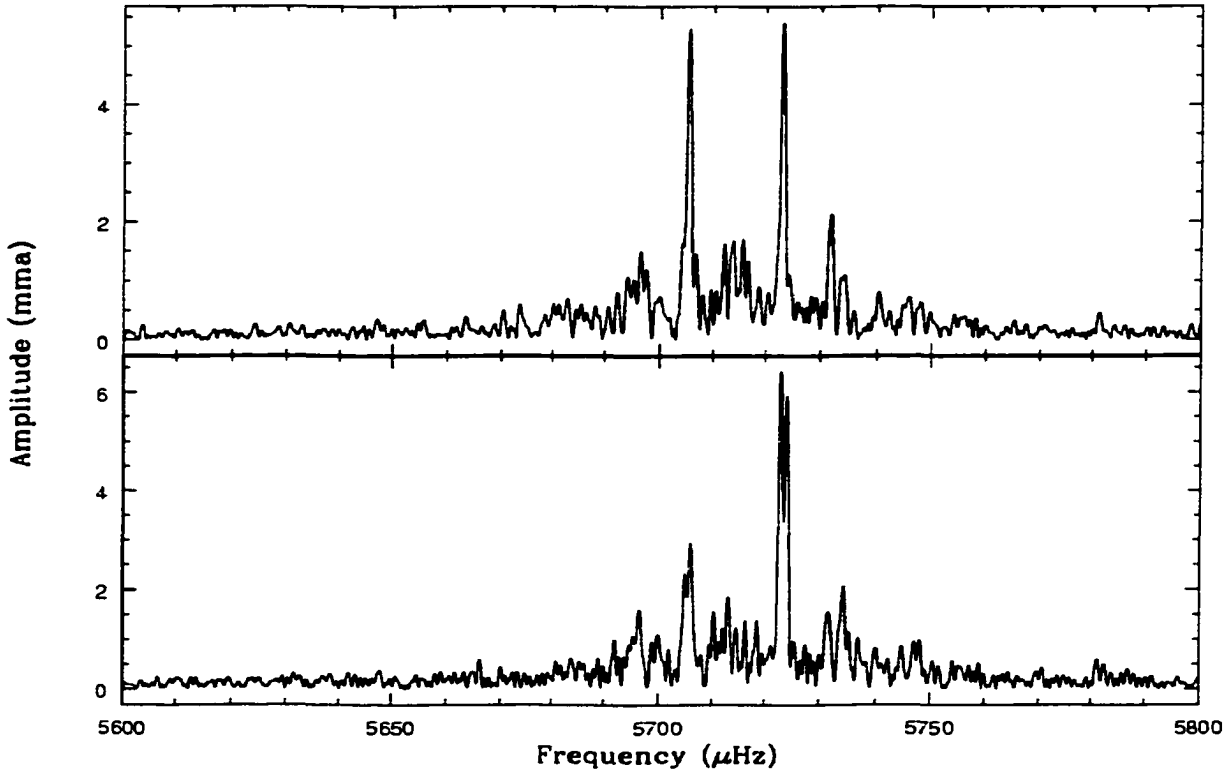

Figure 3.12 An example of complicated data reduction. Top: Temporal spectrum of original simulated data for Case 9 Group VIII. Bottom: The same data fit and prewhitened by the 2 highest amplitude peaks. (Note that the amplitude of one peak actually *increases* after prewhitening!)

parameters.

Table 3.3 summarizes the "geometric" effects and the regimes where they are detectable. In constructing this table, we assume a run of several weeks duration with nightly runs of many hours duration. For short period orbits (<1 week), the only observable effect are the orbital aliases. For medium period orbits (1 week $< \Pi_{orb} <$1 month), a Doppler shift can be detected in the temporal spectrum (if the run happens to occur only when the star is moving towards or away from the observer), and the binary will be observable in the $O - C$ diagram (for data taken over several orbits). For long period orbits (> 1 month but typically on the order of a year or two) the Doppler shift will be detectable and the binary will show up in the $O - C$.

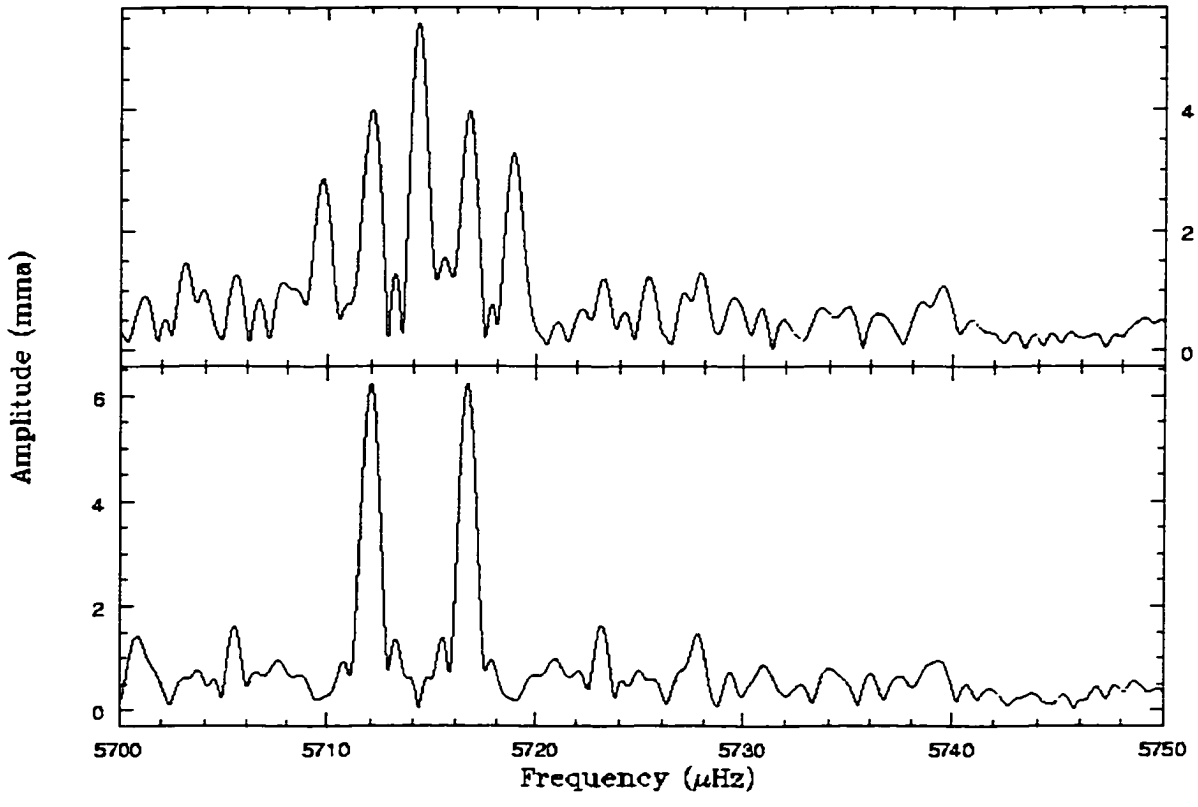

Figure 3.13 Simulated data phase corrected. Top: Original (Case 10VIII) data. Bottom: Same curve corrected for phase only. The two real modes are easily recovered .

Table 3.3 Effects of binarity on pulsation for binaries of various lengths.

Effect	Binary Type		
	Short Period (<1 week)	week – month	Long Period (>1 month)
Doppler Shift	Not noticeable	Yes	Slower velocities, small shift
$O-C$	No	Yes	Detectable
Orbital Alias	Yes	No	No

3.3 Other Possible Manifestations of Binarity

The previous section discussed complication in temporal spectra arising from stars being in close binaries. However, there are additional factors that can affect temporal spectra depending on the specifics of the orbital separation and companion mass.

One of the most obvious signals revealing that two stars are orbiting each other are eclipses. As the fainter star is usually the companion to an sdB star, the sdB star will undergo periodic eclipses if the system is at high inclination. With the pulsation patterns changing in a knowable way, the pulsation amplitude can change through eclipse.

If the orbital separation is small and the companion mass (relatively) large, tidal forces will also become important. In such a case, it is possible for the companion to distort the spherical shape of the pulsator. Such distortions can, in themselves, produce brightness variations at twice the orbital frequency. However, the pulsations themselves may be greatly affected. As described in §2.2, the pulsation axis generally is believed to align with the rotation axis (due to the Coriolis force). However, when tidal forces dominate the Coriolis force, it is possible that the pulsation axis may align itself with the tidal forces[3]. One consequence is that the pulsation axis will be perpendicular to the rotation axis, and actually precess as it follows the companion during each orbit.

These cases are realized in one of the pulsating sdB stars that I studied; see Chapter 8.

3.4 Conclusions

In this Chapter, we explored circumstances under which binarity can affect pulsations. We also determined how binarity would affect the temporal spectrum and how to correct the lightcurves. These findings are listed below.

- Reviewed methods for detecting binary stars.
- Described previous searches for binarity amongst sdB stars.

[3]In an analogous way to the roAp stars, which pulsate along the (inclined) magnetic axis (Baldry, Kurtz, & Bedding, 1998).

- Determined that a significant fraction of sdB stars are in binaries, with orbital periods short enough to be of interest.
- Produced simulations to determine why Doppler shifts are commonly undetected in close binaries via pulsations.
- Described how binarity would show up (and be detected) in the *O-C* diagram.
- Examined temporal spectra for simulated light curves appropriate for sdB stars produced via common envelope evolution.
- Determined that binaries with orbital periods of several days were required before discernible aliases were observed in the temporal spectra.
- Provided a simple method for correcting for periodic phase shifts induced by binarity once the (not so simple) binary parameters are determined.
- Discussed other observational manifestations of binarity on pulsations which may be applicable only to a limited set of binaries.

CHAPTER 4. BACKGROUND AND OBSERVATIONS OF INDIVIDUAL STARS

As we showed in Chapter 1, the class of sdB pulsators display a variety of properties. In this and the remaining chapters, I explore four stars in some detail. Table 4.1 lists their pulsation and physical characteristics. They represent stars that span the range of known pulsating stars; with periods as short as 94 seconds and as long as almost 600 seconds. I chose the sdBV stars with the highest amplitude modes (28 mma) and the lowest amplitude modes (largest peak has an amplitude of 2 mma). Two are apparently single stars, and two are binary stars; one with an F-type main sequence companion, probably in a long period binary, and one with a late M star in a short period binary. One is the coolest sdBV star, another the sdBV star with the lowest surface gravity (indicating that it is the most evolved sdBV star), and two that lie near the zero age extended horizontal branch.

Figure 4.1 shows where the stars studied in this thesis fall on the HR diagram. In this chapter, we will introduce these four stars one at a time. For each star, we will review the available literature on their observed properties, outline the observations that we obtained, as well as data acquired by others that we re-analyzed, and provide temporal spectra with a list of matching periods. We defer further analysis and interpretation of these observations to Chapters 5 through 8.

4.1 PB 8783

PB 8783 was discovered by Berger & Fringant (1984) while searching for faint blue stars at high galactic latitudes. They remark that from their spectra, PB 8783 appears between sdB and HB stars and may be a composite spectrum binary.

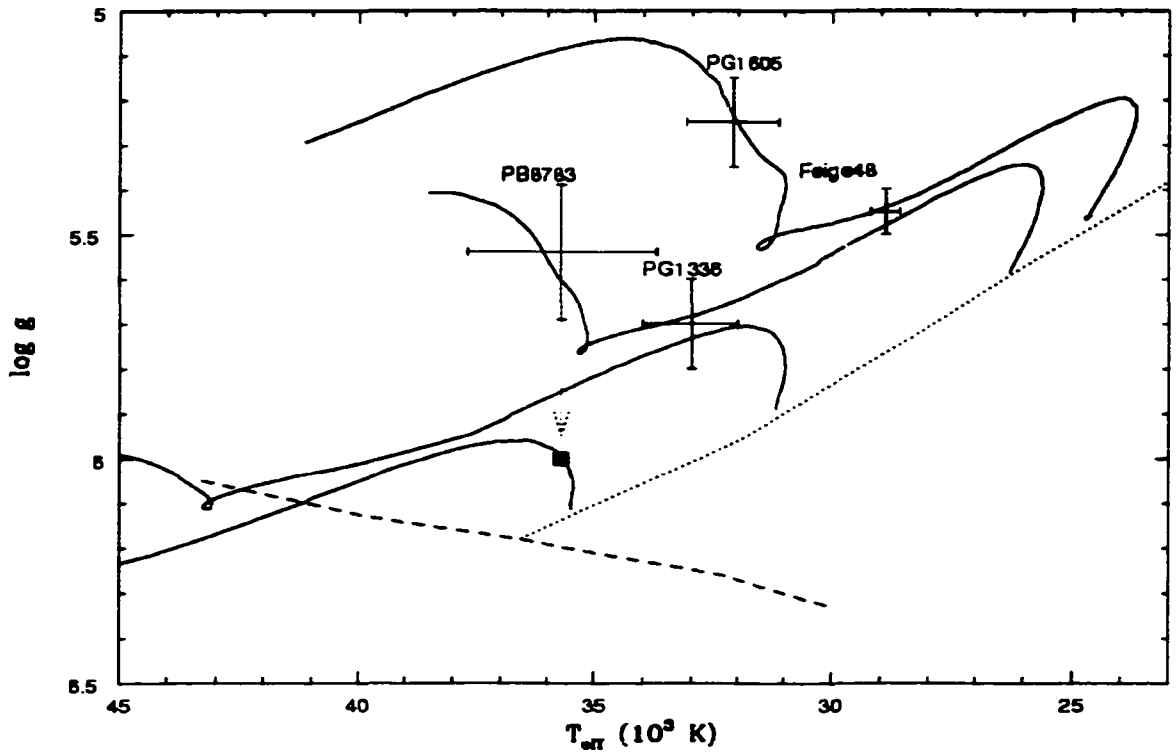

Figure 4.1 HR diagram with errorbars indicated for the four stars discussed in this chapter as well as model evolutionary tracks. Square indicates probable location of PB 8783 as discussed in §4.1. Dotted line is the ZAEHB for a core mass of $0.470M_{\odot}$ and the dashed line is the ZAHeMS.

Table 4.1 Properties of the four sdBV stars selected for study in this work; in order of increase log g.

Star	# of pulsations	Period range (sec)	Largest amplitude (mma)	Binary type	log g	T_{eff} (K)
PG 1605	55+	206–574	27.4	Single	5.25	32 300
Feige 48	5	344–379	6.4	Single	5.5	29 500
PG 1336	22	108–205	4.6	sdB+MS	5.7	33 000
PB 8783	11	94–137	2.1	sdB+MS	~6.0	33 000

A low resolution (3.5Å) spectrum, obtained with multi color photometry by Koen *et al.* (1997) showed strong Balmer lines on a blue continuum as well as the Ca II K line. To fit these two discordant pieces of information, Koen *et al.* (1997) fit the spectrum as a composite of a hot star with a cooler companion. They determined that the sdB star has T_{eff}=33 000K and the companion is a main sequence F star with T_{eff}=7 000K. Assuming that the companion is a main sequence star, Koen *et al.* (1997) isolate the absolute magnitude of the sdB star, which matches previously determined values (Saffer *et al.*, 1994), thus concluding that the pair is a physical binary. Also, from the relative fluxes they are able to determine (assuming an sdB mass of $0.5M_{\odot}$) that R_{sdB}=0.17±0.03$R_{\odot}$, R_{MS}=1.4±0.1$R_{\odot}$, the distance is 800±200 pc and for the sdB star log g=5.70±0.15. Later atmospheric analysis by O'Donoghue *et al* (1998) refined the surface gravity and effective temperature to log g=5.54 and T_{eff}=35 700 K. However, it is suspected that log g for the sdB star has been underestimated due to the contribution to the Balmer lines from the companion and that PB 8783 likely has log g ~6.0 (O'Donoghue *et al.*, 1999), as indicated by the square in Figure 4.1; this is consistent with its pulsation periods (O'Donoghue *et al.*, 1999).

Jeffery & Pollacco (2000) obtained time resolved spectra over a 4 hour period and placed weak but surprising upper limit on the orbital period between 0.8 and 3.2 days via radial velocity variations. However, radial velocity data obtained by E.M. Green (2000; *private communication*) suggest a period between one and two years. This discrepancy remains mysterious.

PB 8783 was discovered to be a pulsating sdB star by Koen *et al* (1997). In their discovery data, taken over an eleven day period, Koen *et al* (1997) detected six low amplitude periodicities between 120 and 135 seconds. It was the target of a multi-site campaign in 1996 (O'Donoghue *et al.*, 1998; who kindly provided their data for this analysis). Over a two week period, they collected data from five sites located around the globe. A light curve of their data is shown in Figure 4.2, and a temporal spectrum in Figure 4.3. Though the pulsations are all low amplitude (less than 3 mma), there are three, comparatively larger amplitude modes, with eight of lesser amplitude. This is typical of sdBV stars. The period, frequency, and amplitude of the eleven separate pulsations determined by O'Donoghue *et al.* (1998) are listed

in Table 4.2.

Table 4.2 The 11 modes detected during the multi-site campaign. (From O'Donoghue *et al.*, 1998) for PB 8783.

Rank	Per	Freq	Amp	Rank	Per	Freq	Amp
n	sec	μHz	mma	n	sec	μHz	mma
9	136.27	7338.40	0.28	1	122.68	8151.63	2.09
2	134.18	7452.52	1.78	6	122.66	8152.56	1.18
7	134.15	7454.42	1.09	10	116.42	8589.72	0.27
4	127.06	7870.32	1.62	11	94.45	10587.21	0.17
5	123.58	8092.08	1.20	8	94.13	10623.24	0.38
3	122.69	8150.68	1.65				

PB 8783 has the shortest pulsation period observed to date (94 seconds) and is also the sdBV star with the lowest amplitude pulsations. The multisite data, provided by D. O'Donoghue (private communication), will be analyzed in the next several chapters.

4.2 PG 1605+072

PG 1605+072 (hereafter PG 1605) was first observed as part of the Palomar Green survey (Green, Schmidt & Liebert, 1984), where it was classified as an sdB star. Low (3.5Å) and intermediate (1.2Å) resolution spectra obtained by Koen *et al.* (1998a) determined that PG 1605 has $\log g = 5.25 \pm 0.10$ and $T_{\rm eff}$=32 100±1000 K. They also determine that any companion to PG 1605 must be later than M0.

A high resolution (0.09Å) spectrum was obtained at the Keck 10 meter telescope by Heber, Reid, & Werner (1999). By simultaneously fitting the Balmer and He line profiles, they determined that PG 1605 has $\log g = 5.25 \pm 0.05$, and $T_{\rm eff}$=32 300±300 K, in good agreement with Koen *et al* (1998a). They were also able to determine a projected rotational velocity of PG 1605 of $v \sin i$=39 km/s which implies a rotation period <8.7 hours.

This makes PG 1605 the sdBV star with the lowest surface gravity, implying that it is the most evolved sdBV star to date. As show in Figure 4.1, the evolutionary model that best describes PG 1605 has ceased core helium burning, and is heading (eventually) to the white dwarf cooling track with helium burning in a shell.

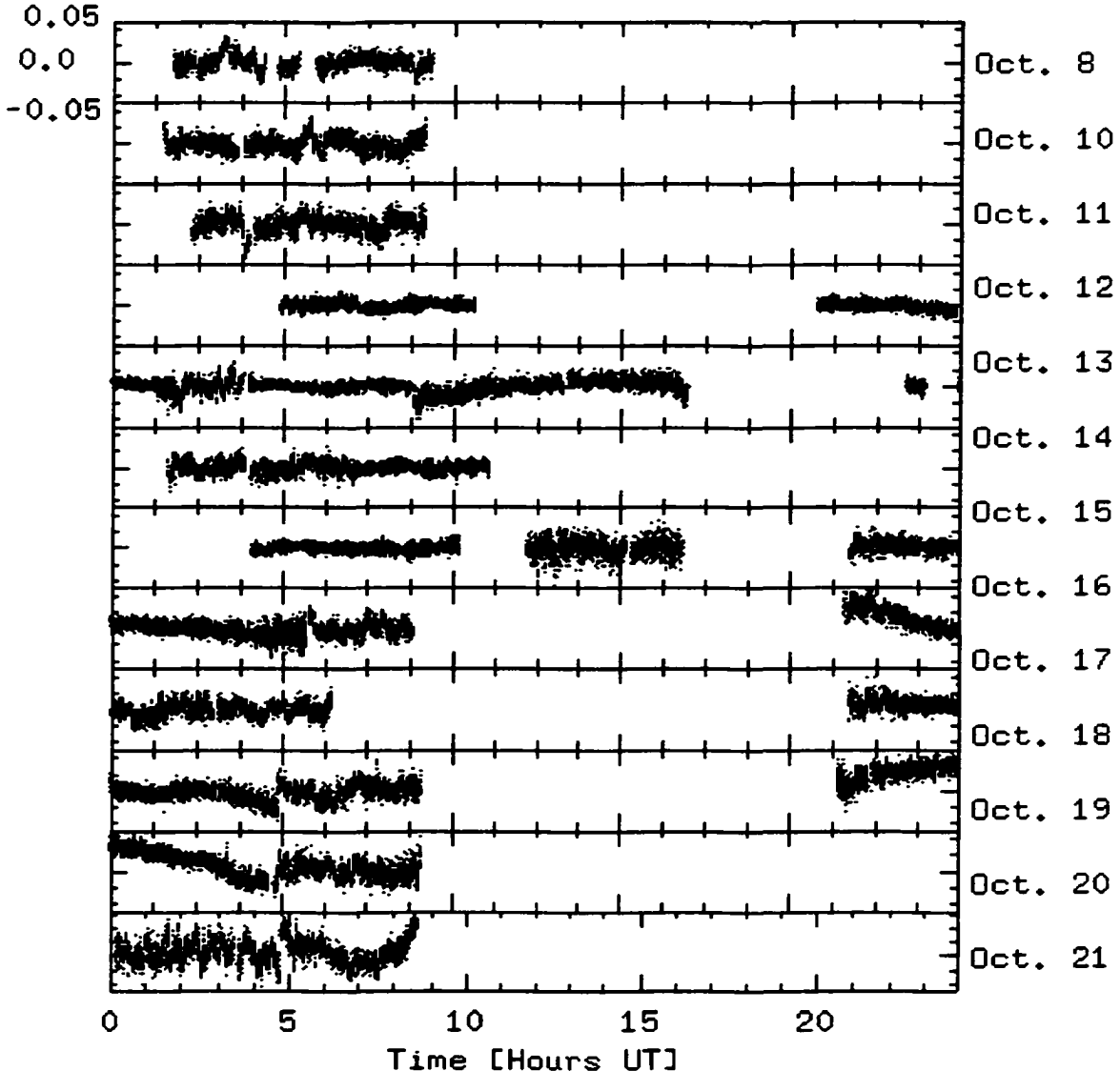

Figure 4.2 Light curve for multisite campaign of O'Donoghue *et al.* (1998) for PB 8783.

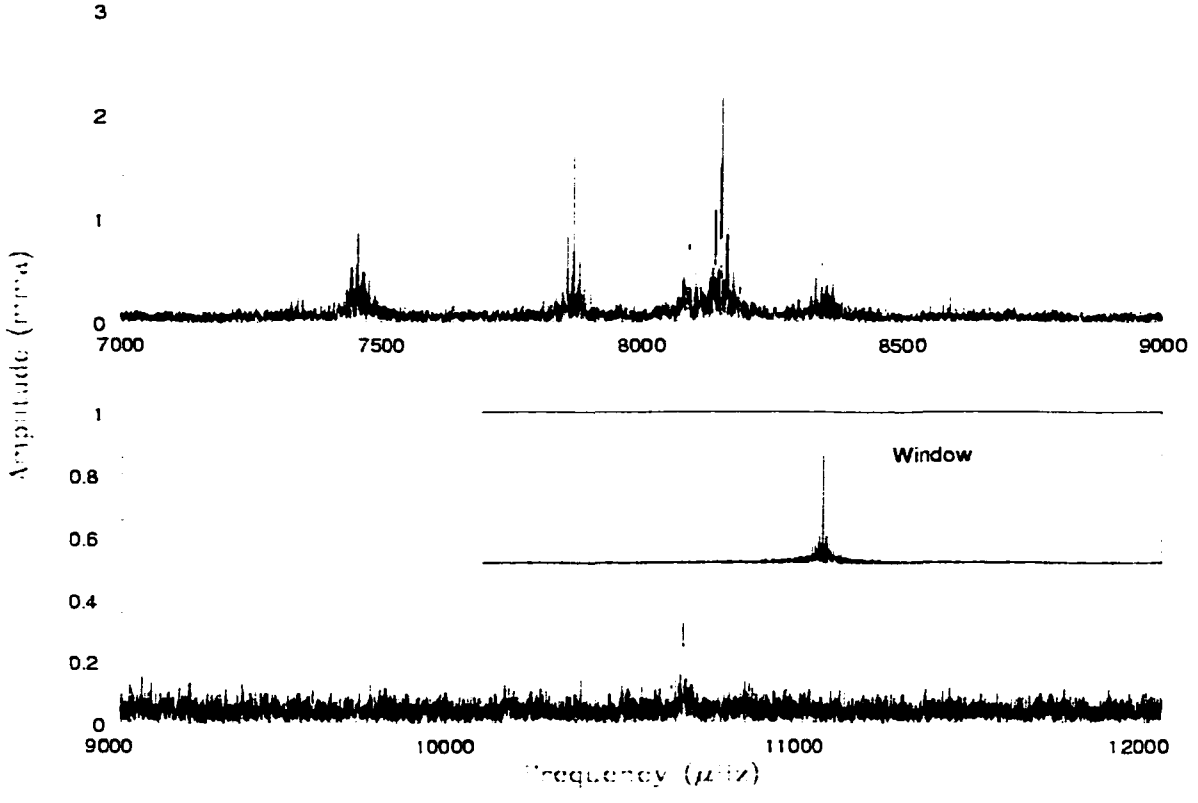

Figure 4.3 Temporal spectrum for PB 8783 from multi site campaign of O'Donoghue *et al.* (1998) for PB 8783.

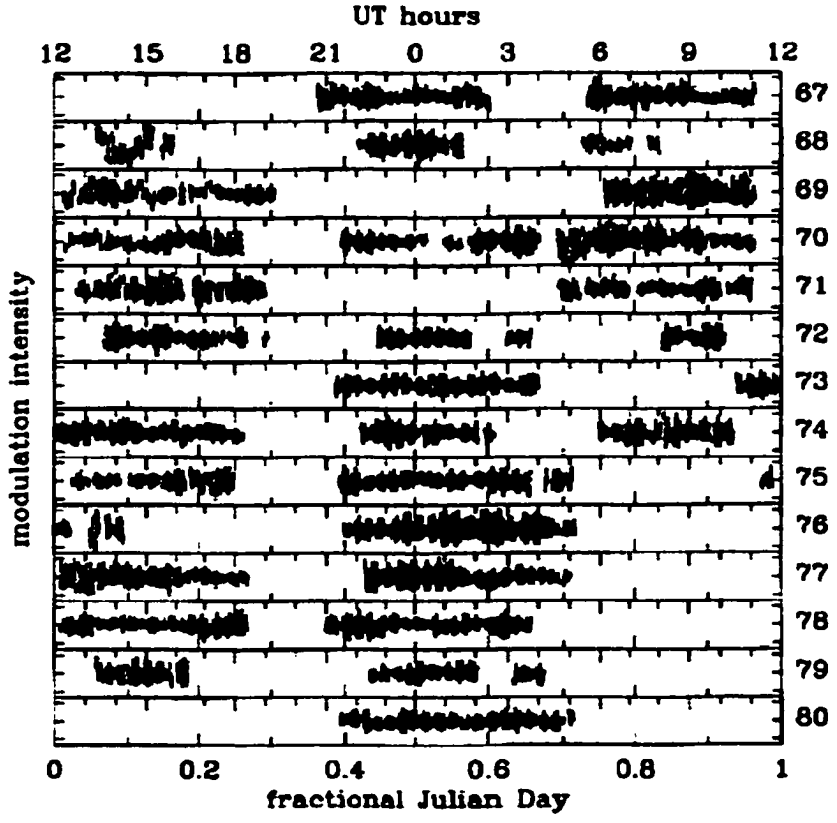

Figure 4.4 Light curve of data obtained during the multi site campaign on PG 1605. Each panel represents one day with dates corresponding to JD 245 0500+. (from Kilkenny *et al.* 1999)

PG 1605 was discovered to be a pulsator by Koen *et al.* (1998a), who detected at least 20 separate periodicities in their temporal spectrum with periods between 200 and 540 seconds and amplitudes up to 64 mma. This was sufficient motivation for Kilkenny *et al.* (1999) to obtain multi site photometry from 5 sites around the globe spanning 14 days (including nearly a month of data from one site)[1]. Figure 4.4 shows the coverage of the ~180 hours of data (43% duty cycle) obtained during the multi site run and Figure 4.5 is the corresponding temporal spectrum.

Analysis by Kilkenny *et al.* (1999) reveal over 50 modes, the ten highest of which are given in Table 4.3. It is clear that the pulsations of PG 1605 span a large range of period. They are

[1]Who also kindly provided their data for re-analysis in this thesis.

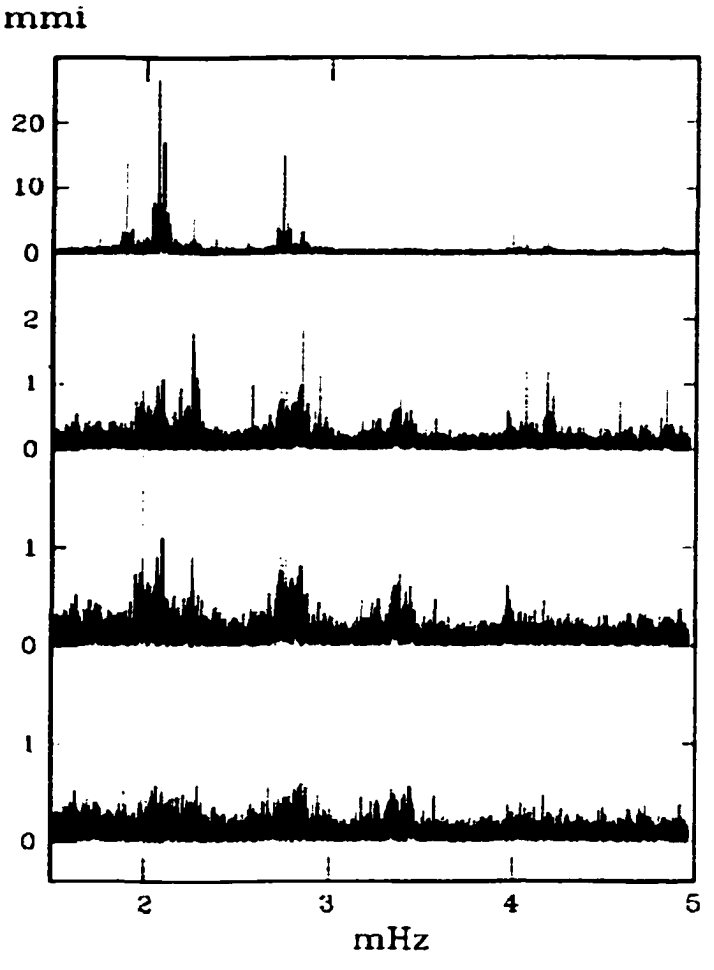

Figure 4.5 Fourier transform of multi site campaign data on PG 1605. Top panel is original temporal spectrum, while subsequent panels are prewhitened by 25, 35 and 55 periodicities. (from Kilkenny *et al.* 1999)

the longest periods detected in an sdBV star thus far, and are also the highest in amplitude.

Table 4.3 The 10 largest amplitude modes of PG 1605 detected during the multi-site campaign. (From Kilkenny *et al.* 1999)

Rank n	Per sec	Freq μHz	Amp mmi	Rank n	Per sec	Freq μHz	Amp mmi
5	528.70	1891.42	13.9	2	475.454	2103.28	15.9
8	503.70	1985.32	3.3	6	440.51	2270.11	1.8
1	481.75	2075.76	27.4	4	364.60	2742.72	15.1
9	479.42	2085.84	3.1	7	351.46	2845.26	3.7
3	475.82	2101.65	15.4	10	250.43	3993.09	3.0

In addition to the aforementioned data, we have obtained over 126 hours of follow up data spanning two more years. In 1999, data were obtained at Fick Observatory, McDonald Observatory, and SAAO as part of an extended two site (North America and South Africa) program. These data were supplemented by three data runs in August, 2000 from Fick Observatory. The specific runs are listed in Table 4.4 and will be discussed in Chapter 6.

4.3 Feige 48

Feige 48 was discovered as part of the Feige survey (Feige, 1958) and categorized as a "faint blue star". It was re-categorized as an sdB star when it was observed as part of the Palomar-Green survey (Green, Schmidt, & Liebert, 1984). In 1997, Koen *et al* (1998b) obtained low (3.5Å) and intermediate (1.2Å) resolution spectra of Feige 48 and determined log g=5.45±0.05 and T_{eff}=28 900±300 K. This makes Feige 48 the coolest sdBV star known to date.

Heber, Reid & Werner (2000) also obtained a high resolution (0.09Å) spectrum of Feige 48 using the Keck I 10 meter telescope. They deduce a slightly higher gravity and effective temperature of 5.5±0.05 and 29 500±300 K, respectively. These are close to the Koen *et al.* (1998b) values (2σ difference)and should be more accurate given Heber, Reid, & Warner's (2000) higher resolution and better signal-to-noise spectra. Heber, Reid & Werner (2000) also place a limit on the rotation rate of Feige 48 of $v \sin i$ <5 km/s. None of the spectroscopic data show indications of binarity, and thus Feige 48 is presumed to be a single star.

Five pulsation periods were detected in Feige 48 by Koen *et al.* (1998b) between 340 and

Table 4.4 Observations of PG 1605

Run	Length (Hours)	Date UT	Observatory	Run	Length (Hours)	Date UT	Observatory
sa-vw195	5.8	5.12.99	SAAO	mdr0496	3.1	6.14.99	Fick 24"
mdr041a	3.1	5.12.99	McD 0.9m	mdr054	1.9	6.15.99	Fick 24"
sa-vw198	6.1	5.13.99	SAAO	mdr055	3.0	6.15.99	Fick 24"
mdr042	7.8	5.13.99	McD 0.9m	mdr056	1.9	6.17.99	Fick 24"
mdr043	7.7	5.14.99	McD 0.9m	mdr057	3.9	6.17.99	Fick 24"
sa-vw200	0.6	5.15.99	SAAO	mdr058	2.0	6.18.99	Fick 24"
mdr044	6.7	5.15.99	McD 0.9m	mdr059	1.7	6.18.99	Fick 24"
mdr045	2.6	5.16.99	McD 0.9m	grr001	4.1	7.20.99	SAAO
mdr046	8.3	5.17.99	McD 0.9m	grr002	1.2	7.21.99	SAAO
mdr047	7.7	5.18.99	McD 0.9m	grr005	4.2	7.23.99	SAAO
mdr048	2.8	5.19.99	McD 2.1m	grr008	1.4	7.24.99	SAAO
mdr050	5.1	5.20.99	McD 2.1m	fvw209	1.8	7.28.99	SAAO
mdr052	6.3	5.21.99	McD 2.1m	fvw210	1.9	7.28.99	SAAO
fm0001	2.2	5.23.99	SAAO	fvw213	1.3	7.29.99	SAAO
fm0002	1.6	5.24.99	SAAO	fvw216	1.3	7.31.99	SAAO
fm3	2.1	5.24.99	SAAO	fvw219	2.9	8.1.99	SAAO
fm4	2.5	5.24.99	SAAO	mdr124	3.5	8.1.00	Fick 24"
mdr0494	0.8	6.14.99	Fick 24"	mdr127	3.0	8.3.00	Fick 24"
mdr0495	0.9	6.14.99	Fick 24"	mdr129	1.3	8.5.00	Fick 24"

380 seconds with amplitudes between 1 and 7 mma. As the coolest sdBV star known to date, it was selected for follow up observations.

I initiated a concerted effort to observe Feige 48 in November of 1998, with a complete list of observations provided in Table 4.5. During a three season program, I was able to obtain nearly 300 hours of data, including 244 hours of single site data (mostly from Fick and McDonald observatories) and 52 hours of multi-site data acquired during Xcov 21[2]. Including the ≈30 hours of data from Koen *et al.* (1998), we have data from January, 1998 (the 1997 Koen *et al.* (1998) data runs were short and not used in our analysis) through April, 2001.

Due to large monthly and annual gaps between observing runs, it was necessary to analyze the data in separate, relatively contiguous subgroups. The dates for the subgroups are given in Table 4.6, the temporal spectra for the groups are plotted in Figure 4.6, and the frequencies determined for several subgroups in Table 4.7.

Though several of the periods are the same in various data sets, it is obvious that some of them differ by a daily alias. Group III comprises the best data set and was therefore our beginning point. Figure 4.7 shows the temporal spectrum and window for Group III data. Frequencies and amplitudes were determined using the least squares (LSQ) method described in §2.1 for the data in Group III. Data from temporally adjacent groups were added one at a time and frequencies and amplitudes were determined again using the previous frequencies and amplitudes as inputs to the LSQ fitting. The "bootstrap" method continued until a satisfactory fit was determined for all the data. Over such a long data set, one has to be concerned with monthly or yearly aliases present in the data. In this case, these are dealt with the same as daily aliases, by checking to see the LSQ fit did not skip over to the next highest peak in the temporal spectrum comprised of the runs in question. Though there is still a chance that some modes may be off by an alias, the periods, frequencies and amplitudes in Table 4.8 represent our best solution.

[2]A complete list of collaborators can be found in Reed *et al.*, 2001.

Table 4.5 Observations of Feige 48

Run	Length (Hrs)	Date UT	Observatory	Run	Length (Hrs)	Date UT	Observatory
mdr006	2.2	11.22.98	McDonald 0.9m	mdr118	3.3	3.5.00	Fick 24"
mdr009	2.6	11.23.98	McDonald 0.9m	mdr119	3.8	5.4.00	Fick 24"
mdr012	2.6	11.24.98	McDonald 0.9m	mdr120	6.0	5.5.00	Fick 24"
mdr017	2.8	11.26.98	McDonald 0.9m	suh-101	6.0	11.2.00	Suhora 0.6m
mdr018	6.0	3.06.99	McDonald 2.1m	suh-102	2.9	11.3.00	Suhora 0.6m
mdr021	5.5	3.09.99	McDonald .1m	suh-103	1.4	11.5.00	Suhora 0.6m
mdr023	4.1	3.10.99	McDonald 2.1m	suh-104	9.7	11.5.00	Suhora 0.6m
mdr24a	6.0	3.11.99	McDonald 2.1m	suh-105	4.6	11.7.00	Suhora 0.6m
mdr29a	8.7	3.15.99	McDonald 2.1m	suh-106	3.2	11.8.00	Suhora 0.6m
mdr030	1.5	3.17.99	McDonald 0.9m	jxj-125	2.5	11.26.00	BAO 0.85m
mdr033	2.0	3.19.99	McDonald 0.9m	jxj-128	3.2	11.27.00	BAO 0.85m
mdr035	6.0	3.20.99	McDonald 0.9m	suh-107	8.8	12.21.00	Suhora 0.6 m
mdr039	5.3	3.23.99	McDonald 0.9m	suh-108	3.4	12.22.00	Suhora 0.6 m
caf48r1r2	7.5	4.12.99	Calar Alto 1.2m	mdr145	8.0	1.18.01	Fick 24"
suh-75	1.7	4.13.99	Suhora 0.6m	mdr146	8.2	1.20.01	Fick 24"
caf48r3	9.3	4.13.99	Calar Alto 1.2m	mdr147	3.6	1.21.01	Fick 24"
mdr091	4.0	12.10.99	Fick 24"	mdr148	9.2	1.22.01	Fick 24"
mdr093	6.2	12.13.99	Fick 24"	mdr149	9.5	1.24.01	Fick 24"
mdr095	2.4	12.14.99	Fick 24"	mdr150	9.2	1.25.01	Fick 24"
mdr096	4.9	12.16.99	Fick 24"	mdr151	7.3	2.1.01	Fick 24"
mdr098	2.1	2.8.00	McDonald 0.9m	asm-0086	4.4	4.19.01	McDonald 0. 9m
mdr100	1.3	2.8.00	McDonald 0.9m	sara0082-6	3.7	4.21.01	SARA 0.9m
mdr103	4.6	2.10.00	McDonald 0.9m	tkw-0065	7.3	4.22.01	McDonald 0 .9
mdr108	2.7	2.12.00	McDonald 2.1m	sara0086-6	6.8	4.24.01	SARA 0. 9m
mdr110	1.0	2.12.00	McDonald 2.1m	IAC80A08	0.8	4.25.01	Teide 0.8m
mdr111	3.3	2.28.00	Fick 24"	sara0088-6	7.0	4.25.01	SARA 0.9m
mdr112	3.7	3.1.00	Fick 24"	IAC80A09	6.1	4.26.01	Teide 0.8m
mdr113	4.0	3.2.00	Fick 24"	sara0089-6	5.4	4.26.01	SARA 0.9m
mdr114	1.5	3.3.00	Fick 24"	suh-102	3.9	4.29.01	Suhora 0.6m
mdr115	6.3	3.4.00	Fick 24"	suh-103	0.6	4.30.01	Suhora 0.6m
mdr116	2.6	3.4.00	Fick 24"	suh-104	0.1	4.30.01	Suhora 0.6m
mdr117	6.0	3.5.00	Fick 24"	IAC80A17	6.1	4.30.01	Teide 0.8m

Table 4.6 Subgroups used in pulsation analysis for Feige 48.

Group	Inclusive dates.	JD2450571+
I	1/28/98 - 2/1/98	0-274
II	11/22/98 - 11/26/98	566-570
III	3/6/99 - 4/13/99	672-710
IV	12/10/99 - 12/16/99	950-956
V	2/8/00 - 3/5/00	1010-1037
VI	5/04/00 - 5/05/00	1097-1098
VII	11/02/00 - 12/22/00	1277-1328
VIII	1/18/01 - 2/1/01	1354-1368
IX	4/19/01 - 4/30/01	1447-1458

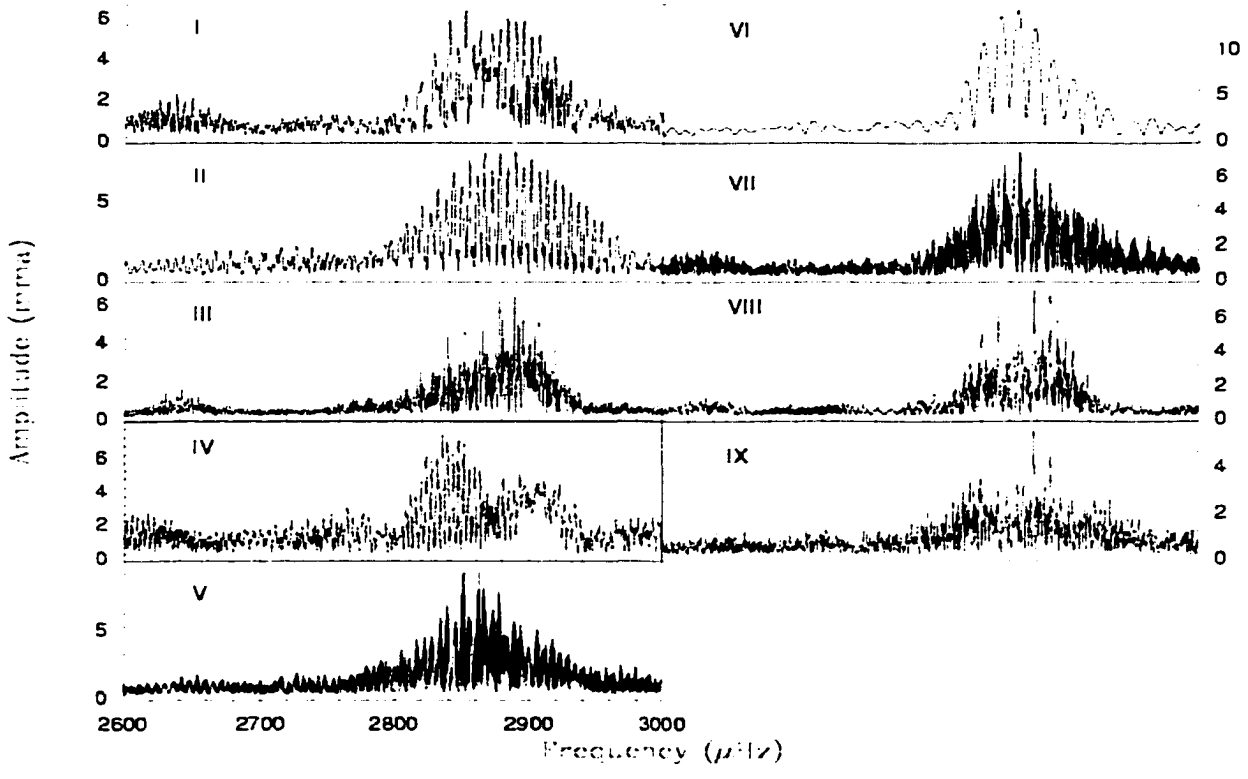

Figure 4.6 Temporal spectra of Feige 48 for the groups provided in Table 4.6.

Table 4.7 Comparison of frequencies (in μHz) detected in various runs for Feige 48. Formal LSQ errors are provided in parentheses.

Group	f_1	f_2	f_3		f_4	f_5
III	2641.978(13)	2837.534(11)	2850.833(4)		2877.157(3)	2906.275(4)
I	2636.96(15)		2850.53(4)	2874.40(23)	2877.31(5)	2917.70(7)*
II	2648.04(24)	2827.16(9)*		2865.63(9)*	2894.74(9)*	
V		2849.208(8)*	2851.365(3)		2877.154(4)	2917.913(7)*

*Indicates modes offset by approximately the daily alias (11.56 μHz).

Table 4.8 Best solution using all the data for Feige 48. Formal LSQ errors in parenthesis.

No.	Period (sec)	Frequency (μHz)	Amplitude (mma)
f_1	378.50293(6)	2641.98750110(35)	1.17(6)
f_2	352.40988(4)	2837.60489893(33)	1.27(6)
f_3	350.77481(2)	2850.83203154(7)	6.15(6)
f_4	347.56503(1)	2877.15939843(7)	6.40(6)
f_5	344.08276(1)	2906.27758187(10)	4.32(6)

4.4 PG 1336-018

PG 1336-018 (hereafter PG 1336) was classified an sdB star in the Palomar-Green survey (Green, Schmidt, & Liebert, 1984). Photometric observations discovered that PG 1336 was an eclipsing binary with an orbital period of 2.4 hours (Kilkenny *et al.*, 1998). PG 1336 is not a composite spectrum binary, but is a spectroscopic binary with a velocity amplitude of 73±3 $km \cdot s^{-1}$. From Balmer line fitting, Kilkenny *et al.*, (1998) determined that the sdB star in PG 1336 (hereafter called the primary) has $\log g = 5.7 \pm 0.1$ and T_{eff}=33 000±1000 K. Radial velocity variations determined (assuming the mass of the primary to be $0.5M_{\odot}$) the mass of the secondary to be $0.15M_{\odot}$; thus the companion is most likely an M5 main sequence star. Eclipse light curve analysis shows that the primary and secondary are of nearly equal size (0.19 and 0.205 $R_{\odot}$ respectively), but the secondary is quite cool (~3 000 K) compared to the primary, so contributes little to the integrated flux[3].

PG 1336 represents an sdBV star of average $\log g$ and T_{eff}, but in a short period binary. The

[3]Since $L \propto T^4$, the companion to PG 1336 should contribute 1/10 000 as much light as the sdBV primary star.

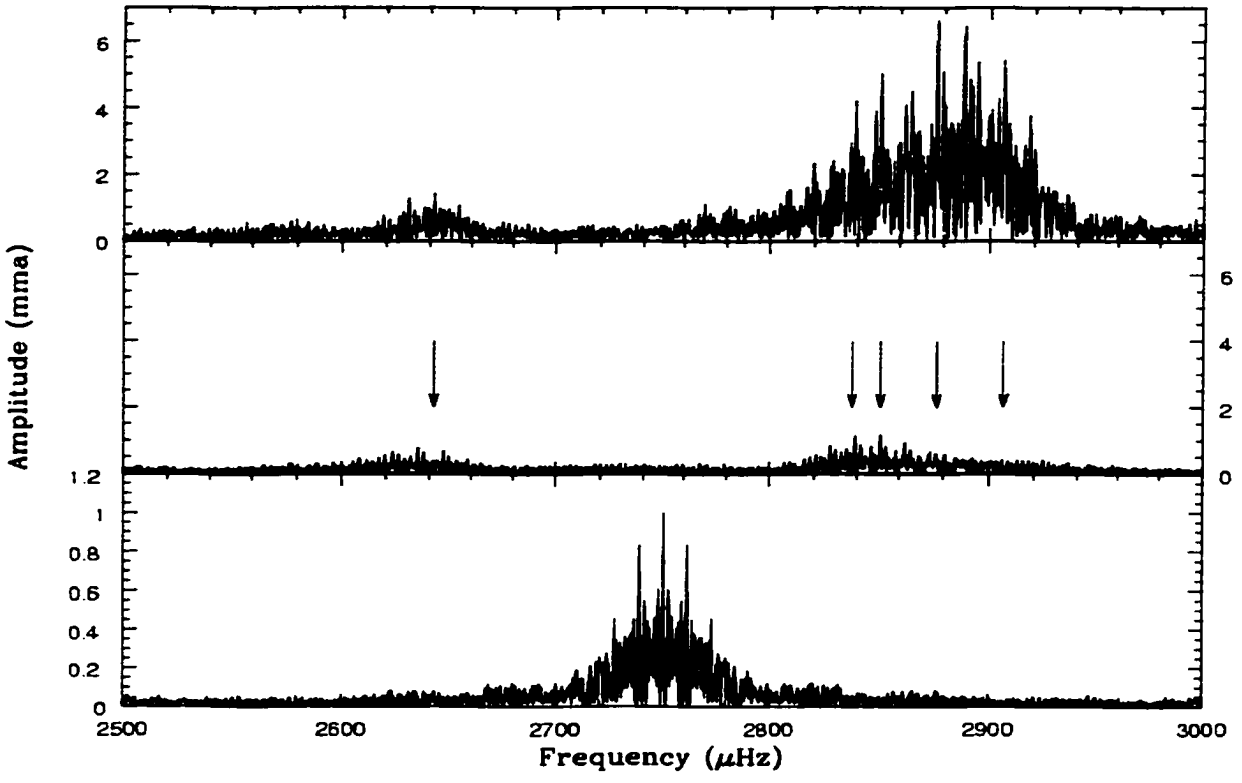

Figure 4.7 Top panel: Temporal spectrum of Group III data of Feige 48. Middle panel: Same spectrum prewhitened by 5 frequencies listed in Table 4.8 (indicated by arrows). Bottom panel: Data window.

formation of such short period binaries requires that the stars have been through a common envelope phase. When the primary went through its red giant stage, the secondary was inside of its radius, so they shared the envelope mass between them. This makes the timescale for circularization of the orbit and tidal locking very short, on the order of a couple decades (Kilkenny, Marang, & Menzies 1994).

PG1336-018 was discovered to be a pulsating sdB star by Kilkenny *et al.* (1998), who report detecting two separate pulsations around 5440 and 7080 μHz. The pulsation amplitudes are $\sim$10 and $\sim$5 mma respectively with other lower amplitude pulsations indicated in the temporal spectrum. A portion of a lightcurve is shown in Figure 4.8 with obvious features of interest in this binary including primary and secondary eclipses, a strong reflection effect, and the

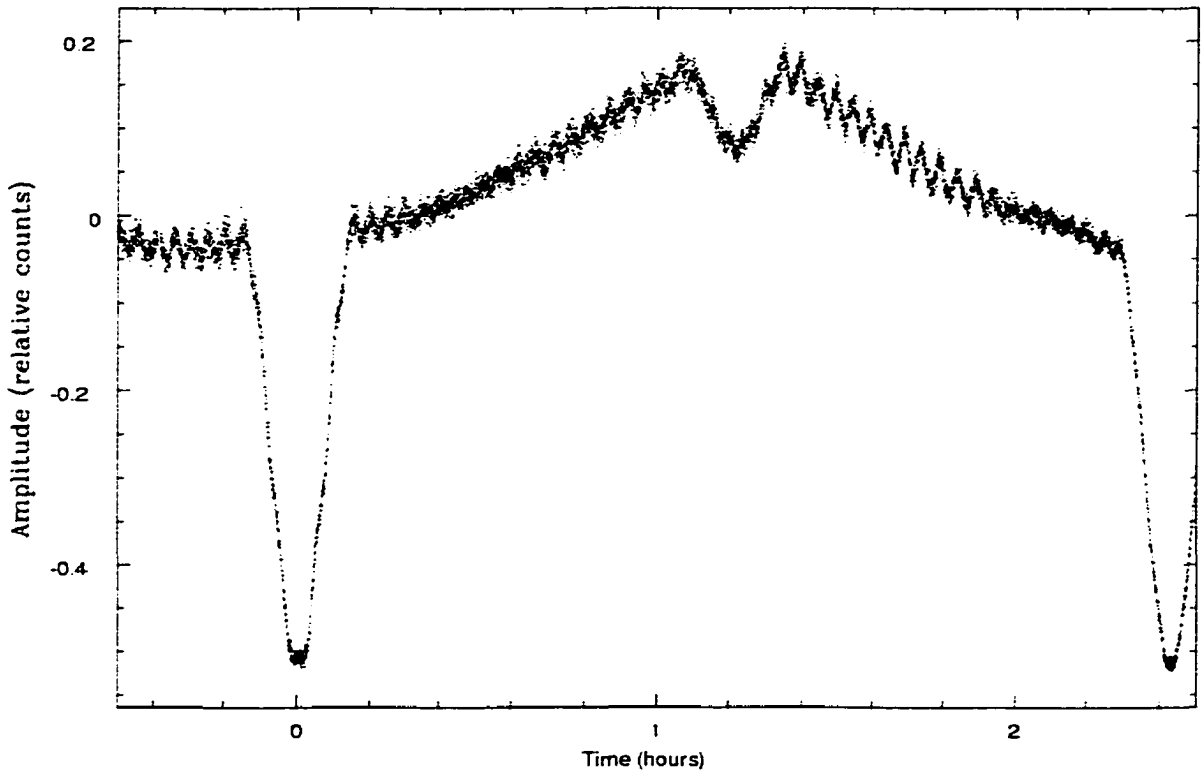

Figure 4.8 A sample portion of the lightcurve for PG 1336 showing primary and secondary eclipses as well as the reflection effect and pulsation.

pulsations themselves.

4.4.1 Xcov 17 Observations

PG 1336 was the co-primary target (along with BPM 37093) for the WET campaign Xcov 17, held in April 1999 (the original PI, Dave Kilkenny, was kind enough share PI responsibility with me). In addition to the WET campaign, pre-WET data were obtained over a 15 day period from McDonald Observatory in March, and a run was obtained from the Nordic Optical Telescope on May 2, 1999. Since there were two primary targets for this WET run, some thin spots in coverage occurred. Due to a lack of sites between McDonald Observatory (Texas) and B.A.O (China) in longitude, a 3 hour coverage gap appeared in every 24 hour cycle. This gap would normally have been covered by Siding Spring and Mount John observatories, but

these sites were dedicated to the southern primary target. During the 14 day period of Xcov 17, 172 hours of coverage were obtained, representing a duty cycle of $\approx$ 47%. Including the pre-WET observations, we obtained 206 hours of coverage, or an overall duty cycle of $\approx$ 43% (for a complete list of data runs, see Reed *et al.*, 2000). Though many hours of data were collected during the WET run, the longest continuous coverage was only 14 hours.

Data acquisition and reduction followed the procedures outlined §2.1 with the following modification: Due to a strong reflection effect, and an eclipse (primary or secondary) every 1.2 hours, the program that converts data timings to barycentric timings was modified by Darragh O'Donoghue to remove eclipses, based on the ephemeris of Kilkenny *et al.* (1998), and fit 2 sinusoids to remove the reflection effect. Corrected light curves for Xcov 17 data are shown in Figure 4.9 while the light curves for the pre and post-Xcov 17 runs are shown in Figure 4.10.

The temporal spectrum is provided in Figure 4.11 along with the data window. As the window shows, the temporal spectrum is complicated by daily aliases (11.6μHz from each peak) and by aliases from the eclipse extraction (114.58μHz from each peak). Twelve periods in the temporal spectrum were fit using the LSQ techniques described in §2.1, with four additional periods found by visual inspection of the temporal spectrum. Table 4.9 provides a complete list of periods and amplitudes as reported in Reed *et al.* (2000).

4.4.2 Xcov 21 Observations

After some tantalizing results from Xcov 17 (see Chapter 8), PG 1336 was again observed from April 16 to May 3, 2001 as the primary target for Xcov 21. In this case, the data were optimized to extract and analyze pulsations during primary eclipse. By using shorter integration times on larger telescopes, we were able to better remove the eclipse shape while maintaining high signal-to-noise, as will be shown in Chapter 8.

The data runs are listed in Table 4.10 while the reduced lightcurves are shown in Figure 4.12. As can be seen in the figure, the coverage for Xcov 21 was far superior to that of Xcov 17, with ~440 hours of data representing a duty cycle of ~62% for the main part of the run (April 17-30).

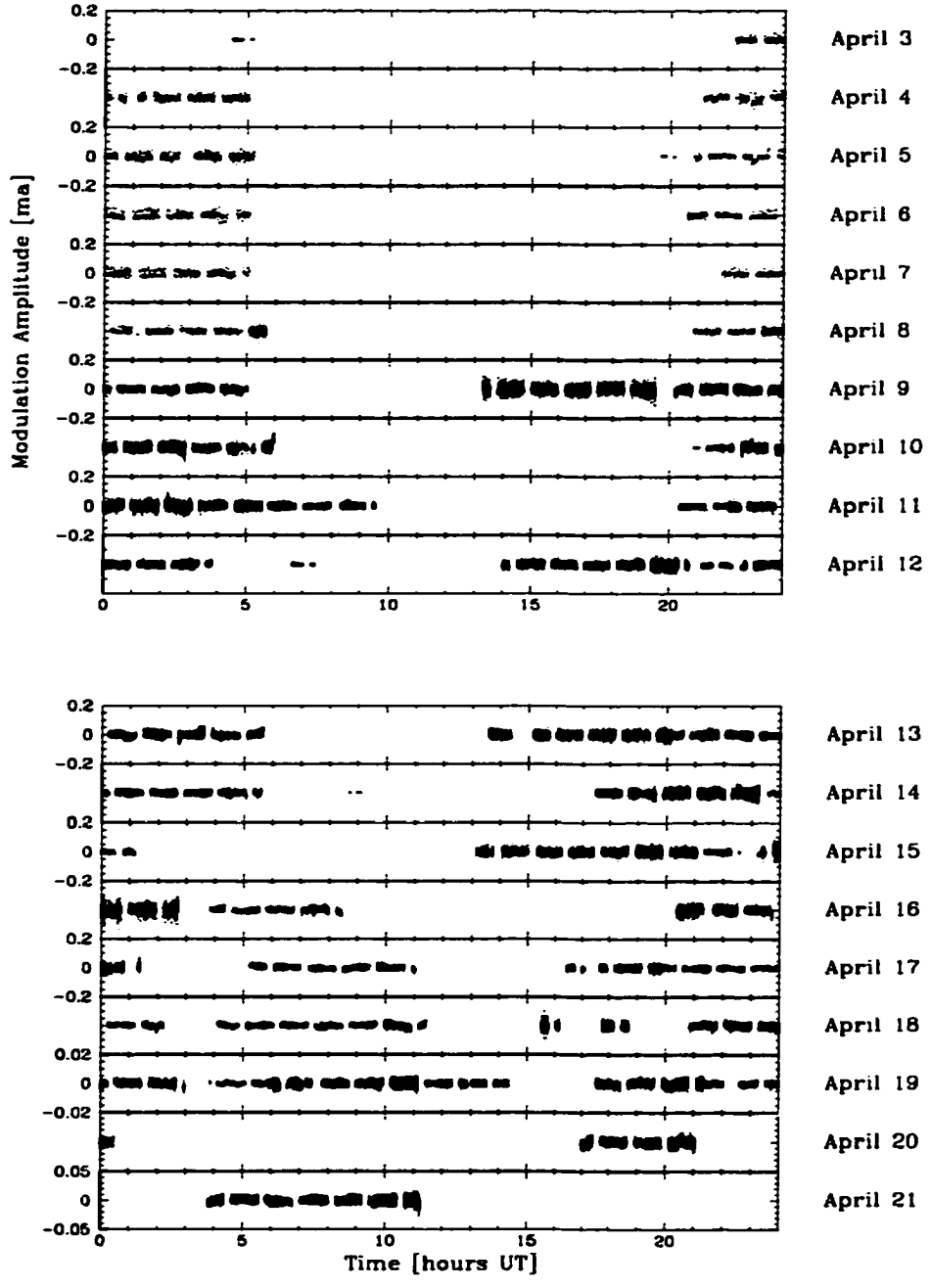

Figure 4.9 Light curve for data obtained during Xcov 17

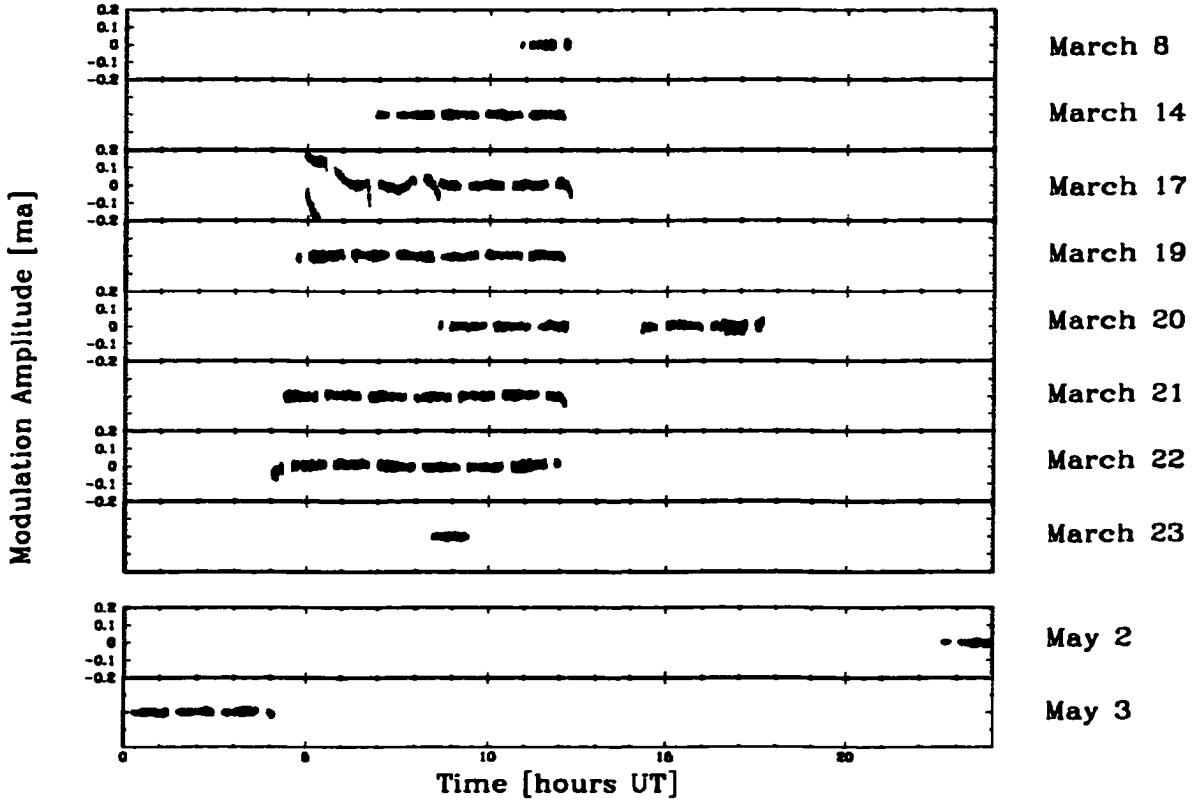

Figure 4.10 Light curve for pre and post-WET (Xcov 17) data

The data were reduced as previously described. The temporal spectrum of the data is shown in Figure 4.13 and the frequencies fit with LSQ and prewhitened are given in Table 4.11. Pulsations previously detected in Xcov 17 are considered identical to those determined during Xcov 21 if their frequencies were the same to within their LSQ errors, and are labeled the same as in Table 4.9. New frequencies detected in Xcov 21 are indicated as gn; where n=1 is the shortest period mode not detected in the Xcov 17 data. The frequencies are very similar to those seen in Xcov 17 with the notable exception of the 5958 μHz mode. This mode is of interest because it is exactly twice the orbital frequency higher than another large amplitude mode, $f1$. Several new, low amplitude modes were also detected in this data set as a consequence of it being superior to the Xcov 17 data set.

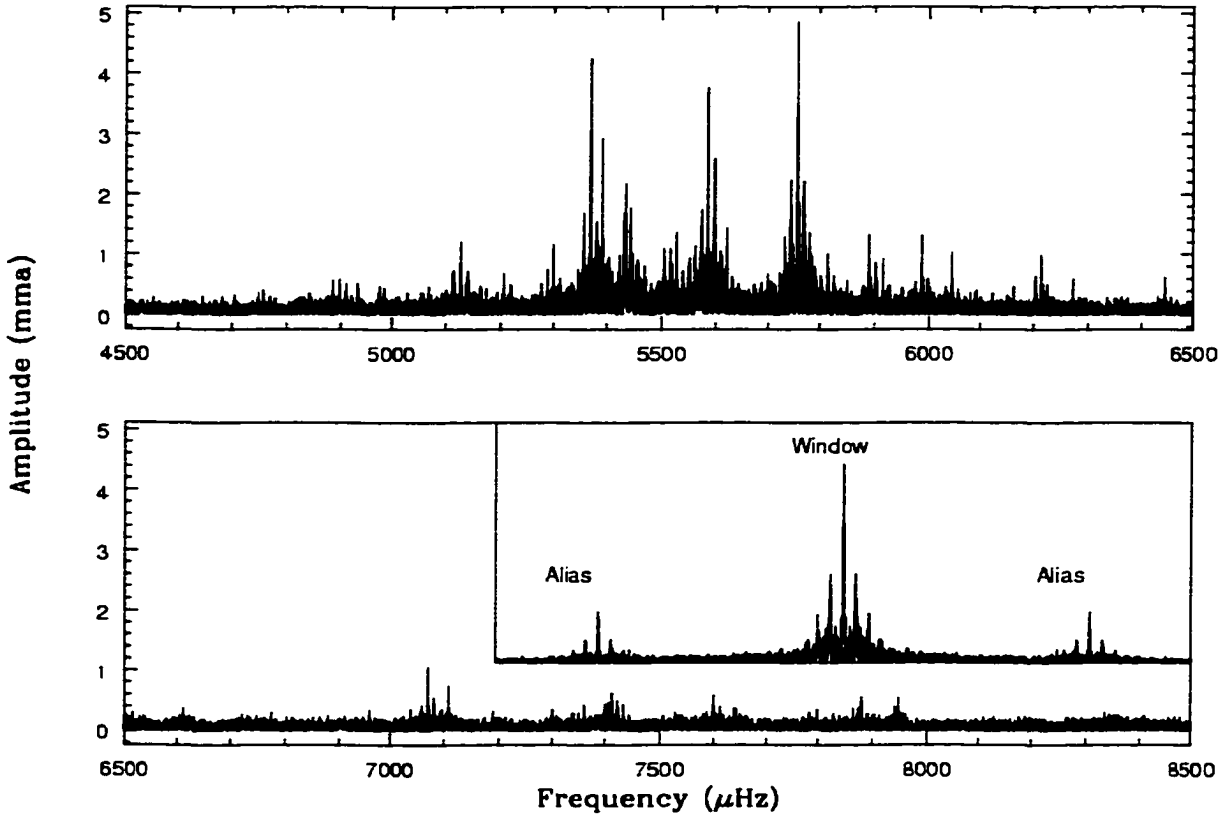

Figure 4.11 The temporal spectrum for Xcov 17 on PG 1336 with the eclipses removed. Inset is the spectral window with the orbital aliases indicated.

4.5 Conclusion

This section introduced four stars that were studied in this thesis. We have reviewed the observations, lightcurves and temporal spectra for the four stars. All of these stars have been the target of multi site campaigns (though Feige 48 was a tertiary target for Xcov 21, and as such, did not receive much attention) and we feel that the pulsations extracted from the temporal spectra represent a sufficiently secure analysis with which we can now explore their physical properties.

We will briefly summarize the properties of the four stars and their data that make them worthy of this thesis.

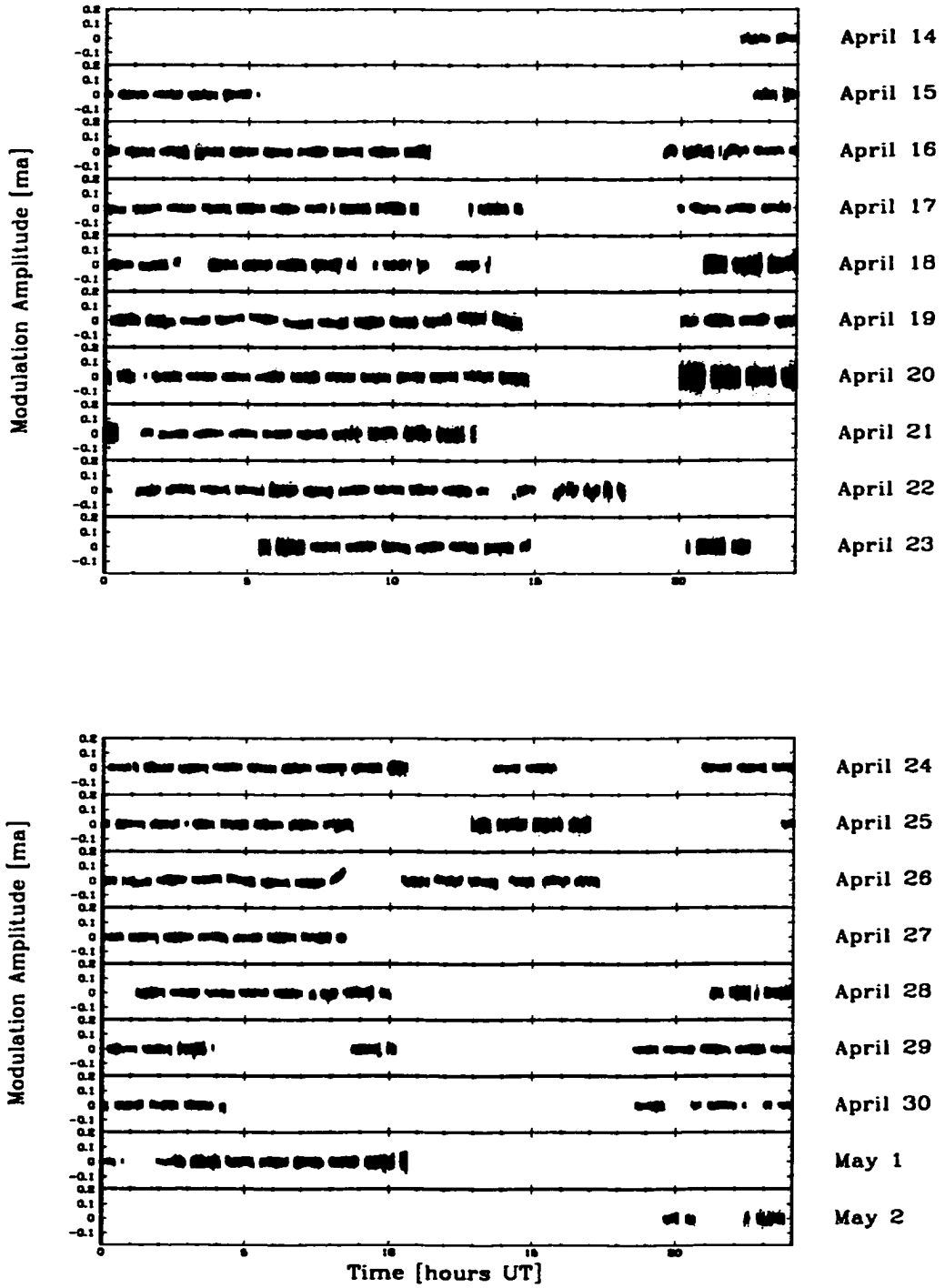

Figure 4.12 Light curve for data obtained during Xcov 21

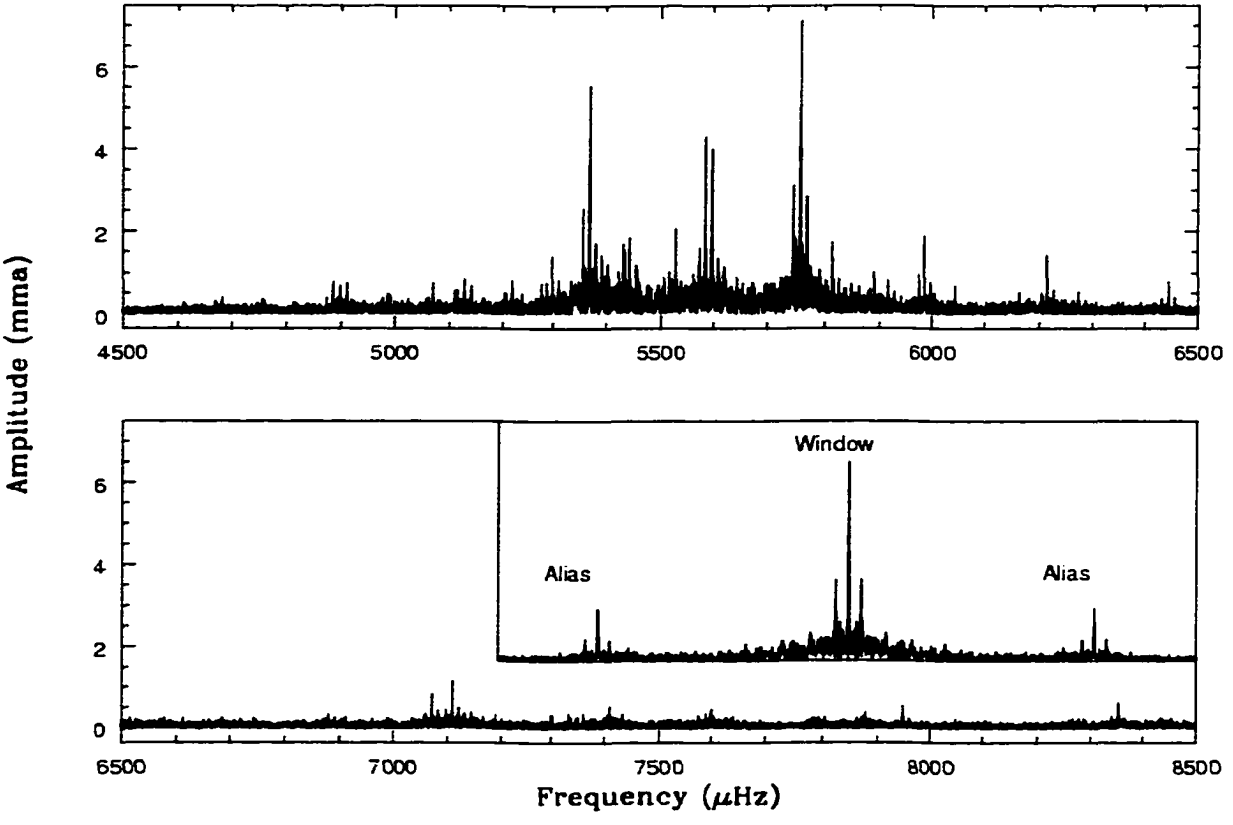

Figure 4.13 Temporal spectrum of Xcov 21 data for the lightcurves in Figure 4.12. Inset is the data window with the orbital aliases indicated.

Table 4.9 Period list for PG 1336 from Xcov 17 (Formal LSQ errors are in parentheses).

Mode	Period (sec)	Frequency (μHz)	Amplitude (mma)	Notes
$f1$	186.24146(7)	5369.374(2)	3.655(7)	1
$f2$	185.45663(14)	5392.096(4)	2.437(7)	1
$f3$	184.05275(20)	5433.225(8)	1.315(6)	2, 3
$f4$	183.97798(17)	5435.433(5)	2.093(7)	1
$f5$	183.67796(19)	5444.311(6)	2.076(7)	2, 3
$f6$	181.63(2)	5505.5(6)	0.842(15)	4
$f7$	179.03049(9)	5585.641(3)	4.085(7)	1
$f8$	173.6923(13)	5757.302(2)	4.790(7)	1
$f9$	173.58926(18)	5760.725(6)	1.643(7)	1
$f10$	169.7361(57)	5891.5(2)	1.24(3)	4
$f11$	141.42079(20)	7071.110(1)	1.027(6)	1
$f12$	140.67685(30)	7108.49(2)	0.680(6)	1
$f13$	131.57953(40)	7599.97(2)	0.439(6)	1
$f14$	126.8874(16)	7881.0(1)	0.55(1)	4
$f15$	125.8099(31)	7948.5(2)	0.57(2)	4

1) Fit using least squares program and effectively prewhitened.
2) Fit using least squares program, but ambiguous prewhitening.
3) Period lies on top of an alias but amplitude is significantly higher than alias.
4) Not fit with least squares program.

PB 8783:

- Pulsating sdB star near the ZAEHB with an F-type main sequence companion; probably in a long period orbit.
- The target of a 5 site campaign in 1996 which resolved the temporal spectrum.
- Eleven pulsations detected between 94 and 137 seconds.
- Largest amplitude mode detected is only ~2 mma, making PB 8783 the lowest amplitude sdBV star known.
- At 94 seconds, PB 8783 has the shortest period pulsations detected to date.

PG 1605:

Table 4.10 Observations of PG 1336 from Xcov 21.

Run	Length	Date	Observatory	Run	Length	Date	Observatory
	(Hrs)	(UT)					
IAC80A01	6.6	4.14.01	IAC 0.8m	sjk-0413	9.4	4.22.01	Hawaii 0.6m
asm-0083	7.5	4.15.01	McD 0.9m	luap23a	4.0	4.23.01	Itajuba 1.6m
adg-0500	6.1	4.15.01	Lemmon 1.5m	tkw-0067	1.6	4.23.01	McD 2.1m
IAC80A02	6.0	4.15.01	IAC 0.8m	sjk-0414	9.3	4.23.01	Hawaii 0.6m
asm-0084	7.7	4.16.01	McD 0.9m	ap2301q1	3.4	4.23.01	Stromlo 1.9m
adg-0501	6.9	4.16.01	Lemmon 1.5m	sara0084-6	5.4	4.23.01	SARA 0.9m
wet01-01	3.3	4.16.01	Naini Tal 1.0m	tkw-0069	2.1	4.24.01	McD 2.1m
IAC80A03	7.5	4.16.01	IAC 0.8m	luap24a	2.2	4.24.01	Itajuba 1.6m
asm-0085	5.1	4.17.01	McD 0.9m	mdr165	5.7	4.24.01	CTIO 1.5m
adg-0502	4.2	4.17.01	Lemmon 1.5m	tkw0070a	4.6	4.24.01	McD 2.1m
adg-0503	3.1	4.17.01	Lemmon 1.5m	luap25a	3.2	4.24.01	Itajuba 1.6m
sara00808[1]	6.6	4.17.01	SARA 0.9m	NOT-kd24a	3.9	4.24.01	NOT 2.6m
sjk-0407	5.0	4.17.01	Hawaii 0.6m	ap2401q1	3.1	4.24.01	Stromlo 1.9m
sa-mk130	6.5	4.17.01	SAAO 1.0m	iac80a06	5.2	4.24.01	IAC 0.8m
IAC80A04	7.6	4.17.01	IAC 0.8m	jxj-0140	5.4	4.24.01	BAO 0.85m
ap1701q1	0.4	4.17.01	Stromlo 1.9m	sara0087-7	1.5	4.24.01	SARA 0.9m
ap1701q2	2.5	4.17.01	Stromlo 1.9m	jxj-0139	4.0	4.25.01	BAO 0.85m
ap1701q3	2.5	4.17.01	Stromlo 1.9m	mdr168	2.9	4.25.01	CTIO 1.5m
loiano-0417-1	2.9	4.17.01	Loiano 1.52m	geb0001	3.5	4.25.01	McD 2.1m
loiano-0417-2	2.9	4.17.01	Loiano 1.52m	suh-100	4.7	4.25.01	Suhora 0.6m
pg0417ol	4.8	4.17.01	OHP 1.93m	NOT-kd25a	4.0	4.25.01	NOT 2.6m
sjk-0408	4.7	4.18.01	Hawaii 0.6m	lu-ap26a	3.0	4.25.01	Itajuba 1.6m
mdr152	7.9	4.18.01	CTIO 1.5m	mdr171	7.3	4.26.01	CTIO 1.5m
obj01	3.7	4.18.01	Itajuba 1.6m	notkd26a	1.4	4.26.01	NOT 2.6m
adg-0504	5.2	4.18.01	Lemmon 1.5m	notkd26b	2.8	4.26.01	NOT 2.6m
pg0418oh	4.7	4.18.01	OHP 1.93m	ap2601q1	7.3	4.26.01	Stromlo 1.9m
lo0418	6.5	4.18.01	Loiano 1.52m	ap2601q2	0.3	4.26.01	Stromlo 1.9m
mdr154	7.2	4.19.01	CTIO 1.5m	sara0090-6	1.2	4.26.01	SARA 0.9m
lo0419	4.6	4.19.01	Loiano 1.52m	lu-ap27a	2.7	4.27.01	Itajuba 1.6m
luc01	2.1	4.19.01	Itajuba 1.6m	mdr174	7.4	4.27.01	CTIO 1.5m
luc02	0.6	4.19.01	Itajuba 1.6m	IAC80A10	1.5	4.27.01	IAC 0.8m
sa-mk134	6.7	4.19.01	SAAO 1.0m	IAC80A11	2.4	4.27.01	IAC 0.8m
sjk-0409	9.1	4.19.01	Hawaii 0.6m	suh-101	6.3	4.27.01	Suhora 0.6m
turkey01	4.2	4.19.01	Tubitak 1.5m	mdr177	6.3	4.28.01	CTIO 1.5m
mdr156	5.0	4.20.01	CTIO 1.5m	IAC80A12	5.2	4.28.01	IAC 0.8m
mdr157	1.2	4.20.01	CTIO 1.5m	iac80a13	8.7	4.28.01	IAC 0.8m
luc01-ap20	2.1	4.20.01	Itajuba 1.6m	geb0003	8.3	4.28.01	McD 2.1m

Table 4.10 (Continued)

Run	Length	Date	Observatory	Run	Length	Date	Observatory
	(Hrs)	(UT)					
lo0420a	2.1	4.20.01	Loiano 1.52m	IAC80A14	1.7	4.29.01	IAC 0.8m
pg0420oj	4.8	4.20.01	OHP 1.93m	IAC80A15	1.9	4.29.01	IAC 0.8m
sjk-0410	9.1	4.20.01	Hawaii 0.6m	eddar01	2.5	4.29.01	Moletai 1.6m
luc01-21	2.0	4.21 .01	Itajuba 1.6m	geb-0004	2.2	4.29.01	McD 2.1m
mdr159	6.8	4.21.01	CTIO 1.5m	geb-0005	2.2	4.29.01	McD 2.1m
sjk-0411	7.0	4.21.01	Hawaii 0.6m	xgh-0483	4.0	4.29.01	SAAO 1.9m
pg0421oh	4.2	4.21.01	OHP 1.93m	iac80a16	7.8	4.29.01	IAC 0.8m
mdr162	4.7	4.22.01	CTIO 1.5m	notkd30a	1.9	4.30.01	NOT 2.6m
lu-ap22	6.5	4.22.01	Itajuba 1.6m	notkd30b	4.3	4.30.01	NOT 2.6m
ap2201q1	3.9	4.22.01	Stromlo 1.9m	geb-0006	6.0	5.01.01	McD 2.1m
lo0422	1.7	4.22.01	Loiano 1.52m	notke01a	3.2	5.01.01	NOT 2.6m
IAC80A05	7.1	4.22.01	IAC 0.8m				

- Most evolved sdBV star discovered to date.
- Not a spectroscopic, composite-spectrum, or photometric binary, with a limit on any companion later than M0. This appears to be a single star.
- The target of a 5 site campaign in 1997, spanning nearly a month of single site data which resolved the temporal spectrum.
- Over 55 separate pulsations detected between 206 and 574 seconds, making PG 1605 the richest sdBV star detected to date.
- PG 1605 has the longest period pulsations of any sdBV star detected to date.
- PG 1605 has the largest amplitude pulsations detected in an sdBV star to date.

Feige 48:

- Coolest sdBV star discovered to date.
- Not a spectroscopic, composite-spectrum, or photometric binary. Feige 48 appears to be a single star.

Table 4.11 Period List for PG 1336 from Xcov 21. Formal LSQ errors in parenthesis.(f denote modes also detected in Xcov 17 data, g denotes modes observed only in Xcov 21.)

Mode	Period (sec)	Frequency (μHz)	Amplitude (mma)
$g1$	204.70410(80)	4885.100(19)	0.79(4)
$g2$	195.65236(107)	5111.106(28)	0.54(4)
$g3$	191.60600(71)	5219.043(19)	0.79(4)
$g4$	186.69102(62)	5356.444(18)	0.88(4)
$f1$	186.24173(14)	5369.366(4)	4.60(5)
$f2$	185.44533(37)	5392.425(11)	1.46(4)
$g5$	185.21156(51)	5399.231(15)	1.04(4)
$f3$	184.05231(43)	5433.238(13)	1.25(4)
$f4$	183.97876(37)	5435.410(11)	1.44(4)
$f5$	183.67847(32)	5444.296(9)	1.83(4)
$g6$	181.58026(61)	5507.207(19)	0.83(4)
$f7$	179.03017(16)	5585.651(5)	3.64(4)
$g7$	178.61920(25)	5598.502(8)	2.35(5)
$f8$	173.69290(7)	5757.288(2)	7.20(4)
$f9$	173.58807(33)	5760.764(11)	1.57(4)
$f10$	169.73700(56)	5891.467(19)	0.78(4)
$g8$	169.02914(52)	5916.140(18)	0.85(4)
$g9$	162.23607(100)	6163.857(38)	0.40(4)
$f11$	141.41908(40)	7071.182(20)	0.77(4)
$f12$	140.68283(59)	7108.188(30)	0.51(4)
$g10$	140.66499(30)	7109.089(15)	1.13(4)
$g11$	134.93613(51)	7410.914(28)	0.55(4)
$f13$	131.56981(52)	7600.528(30)	0.50(4)
$g12$	126.92213(55)	7878.847(34)	0.44(4)
$f15$	125.80743(49)	7948.657(31)	0.49(4)
$g13$	119.70439(29)	8353.912(20)	0.75(4)
$g14$	108.45930(18)	9220.048(15)	1.00(4)

- Observed over a three year period including some multi site data obtained during Xcov 21 in April, 2001.
- Five pulsation frequencies are detected in the temporal spectrum between 344 and 379 seconds with amplitudes between 1 and 7 mma.

PG 1336:

- Pulsating star of average log g and T_{eff} in a short period (2.4 hour) eclipsing binary with a late-type (~M5) main sequence secondary.
- Secondary is substantially cooler than the primary, so contributes little to the integrated flux.
- Light curve shows primary and secondary eclipses as well as a strong reflection effect and obvious pulsations.
- Presumed tidally locked system, providing a known rotation period.
- Was the target of two WET runs (Xcov 17 and 21) in April, 1999 and April, 2001, both of which resolved the temporal spectrum.
- Pulsates in at least 22 modes between 108 and 205 seconds with amplitudes between 0.4 and 7.2 mma.

CHAPTER 5. PATTERN ANALYSIS

Chapter 4 introduced the four stars that will be analyzed in the rest of this thesis. It described the observations and provided a list of pulsation periods observed in each star. We now apply the first of the tools described in §2.4, pattern matching techniques, to the observed pulsation periods. This technique uses the pulsation periods, or frequencies, and their separations to identify pulsation modes (i.e. p- or g-modes and the quantum numbers ℓ and n). The identification of pulsation modes serves as a contact point between observations and theory. We calculate a range of evolutionary models that match the physical characteristics (log g and T_{eff}) of the star. Once modes are identified, we select the most appropriate model by comparing the model frequencies, given the mode constraints to the frequencies identified in the observations. In this manner, we can determine the best match stellar model, and therefore, the structure of the sdB star.

We address the stars in the same order as they were introduced. We begin with PB 8783, the sdBV star that likely has the largest surface gravity, and is in a binary with an F-type main sequence star. We first examine its temporal spectrum for equally spaced modes, then apply what we modeled in §3.2.4 to look for the signature of binarity on PB 8783's pulsations. This is a good case for detecting effects of binarity on pulsations *if* the binary period is under one week (as claimed by Jeffery & Pollacco, 2000) as it has the most massive companion detected to date (with a light crossing time [t_{delay}] midway between cases 7 and 10 in §3.2.4).

PB 1605 is an apparently single sdBV star. It does not appear to be a composite spectrum or photometric binary (Koen *et al*, 1998a; Heber, Reid, & Werner, 1999). However, it is the sdBV star with the lowest log g and longest pulsation periods (both correlated with the density of the star). Also, it is the first sdBV star to have preliminary mode identifications

made (Kawaler 1999).

Feige 48 is another sdBV star that is apparently single based on spectroscopic measurements (Heber, Reid, & Werner, 2000). Feige 48 is the coolest sdBV star detected to date, with log g (and pulsation periods) intermediate between PG 1605 and the majority of the class (which has log g closer to the ZAEHB). Prior to this study, Feige 48 only had limited discovery data (Koen *et al*, 1998b). In this chapter, we will examine the periods determined from our extensive observations.

PG 1336 is our sdBV star in a short period binary (Kilkenny *et al.* 1998). It is also the star for which we have the most observations. PG 1336 has been observed during two WET campaigns recording over 650 hours of data. Each campaign has revealed a rich temporal spectrum. In section 4, we will examine those spectra, searching in particular for evenly spaced pulsations as a means of mode identification.

5.1 PB8783

As described in §2.2.3, rotation can split a nonradial mode into its $(2\ell+1)$ components evenly spaced in frequency; indicating the ℓ value of the pulsation if all m modes are present. We first examine the frequency separations between observed modes and look for patterns. The "splittings" or distances between each mode in the temporal spectrum are given in Table 5.1 (in both seconds and μHz).

The data show splittings in two groups. There is a triplet near 122 seconds in period. The two spacings on the triplet are $\sim$0.94μHz. If this is an ℓ=1 triplet, then the splitting implies a rotation period of 12.3 days. However from the 14 day run, the data have a 1/T resolution of 0.8μHz (with an LSQ uncertainty of 0.1μHz) so the triplet is barely resolved. This is also little longer than the 12 day beat period. We note that two other modes are separated by 2$\times$0.95=1.9μHz; perhaps being a triplet with a missing central peak Additionally, O'Donoghue *et al.* (1998) hint that there is significant leftover power in the temporal spectrum. Since PB 8783 has such low amplitudes, it makes it impossible to identify any modes past the 11 provided in Table 4.2 with the current data. Though it is possible that there are other

Table 5.1 Separations of the 11 modes in Table 4.2 for PB 8783.

Rank n	Per sec	Freq μHz	Amp mma	$\Delta\Pi$ sec	Δf μHz
9	136.27	7338.40	0.28		
				2.09	114.12
2	134.18	7452.52	1.78		
				0.03	1.9
7	134.15	7454.42	1.09		
				7.09	415.9
4	127.06	7870.32	1.62		
				3.48	221.76
5	123.58	8092.08	1.20		
				0.89	58.60
3	122.69	8150.68	1.65		
				0.01	0.95
1	122.68	8151.63	2.09		
				0.02	0.93
6	122.66	8152.56	1.18		
				6.24	437.16
10	116.42	8589.72	0.27		
				21.97	1997.49
11	94.45	10587.21	0.17		
				0.32	36.03
8	94.13	10623.24	0.38		

multiplets in PB 8783, it will require a longer multi site campaign (to resolve the pulsations) with larger telescopes (to increase the signal-to-noise of the data).

5.1.1 Complications Due to Binarity

As mentioned in §4.1, Jeffery & Pollacco (2000) obtained high-speed spectroscopy of PB 8783 (1998) and provide an upper limit to the binary period of 0.8 - 3.7 days, depending on inclination. If true, this would imply orbital aliases due to delays in pulsation phases (see §3.2.4) at separations of between 23 and 4μHz. No such splittings are observed. However, since PB 8783 represents the best (and to this point only) candidate for observational manifestations of binarity in the temporal spectrum due to phase delay, we decided to dig deeper in the data of O'Donoghue *et al.* (1998). If we assume the highest possible inclination without an eclipse

($\sim$ 80°) then the Jeffery and Pollacco (2000) upper limit to the orbital period of 3.2 to 3.7 days with a secondary mass of 1.8 to 1.2$M_\odot$ (as derived from the depth of the Ca absorption lines in the composite spectrum) produces an orbital light crossing time of 63 and 56 seconds respectively (for $i = 80°$). Using the multi-site data, we created two sets of artificial lightcurves for the highest amplitude modes. We considered a single mode and a rotationally split doublet. For each, we applied the orbital constraints above. The process of producing simulated lightcurves proceeded as in §3.2.4: the data timings were taken from the actual data while the periodic signals (ΔI/I) were derived from Equation 3.4, with Poisson distributed noise appropriate for the 1 meter class telescopes used. We produced simulated lightcurves for a single peak centered at 8151 μHz and for simulated $m = \pm 1$ modes at $8151 \pm (1/\Pi_{orb})$ μHz.

Figure 5.1 shows the Fourier transforms of the resulting simulations. The top panel shows the spectral window, the middle two panels show simulated data (for a single mode, and for rotationally split $m = \pm 1$ modes), and the bottom panel is the FT of the data from O'Donoghue *et al.* (1998). For the panels showing the simulations, the left plot is for one extreme, $M_2 = 1.8 M_\odot$, P_{orb}=3.2d while the right plot is for the other, $M_2 = 1.2 M_\odot$, P_{orb}=3.7d. The data look nothing like these simulations, suggesting that the assumed orbital period is not within a range to which the data are sensitive (between 1 and 12 days).

From our simulations, we can conclude that either the inclination is small (meaning a shorter period if the velocity variations of Jeffery and Pollacco [2000] are correct) or the period is significantly longer. If the period is shorter, than the light travel time across the orbit will be reduced (t_{delay} from Equation 3.1), so the phase lag ($\Delta\tau$ from Equation 3.3) will not produce noticeable extra peaks in the temporal spectrum. If the period is longer (as indicated by data from E.M. Green; private communication) then it is consistent with the evolutionary description by Green, Liebert, & Saffer (2000; described in §3.1.3) and again, there will be no observed orbital aliases in the temporal spectrum.

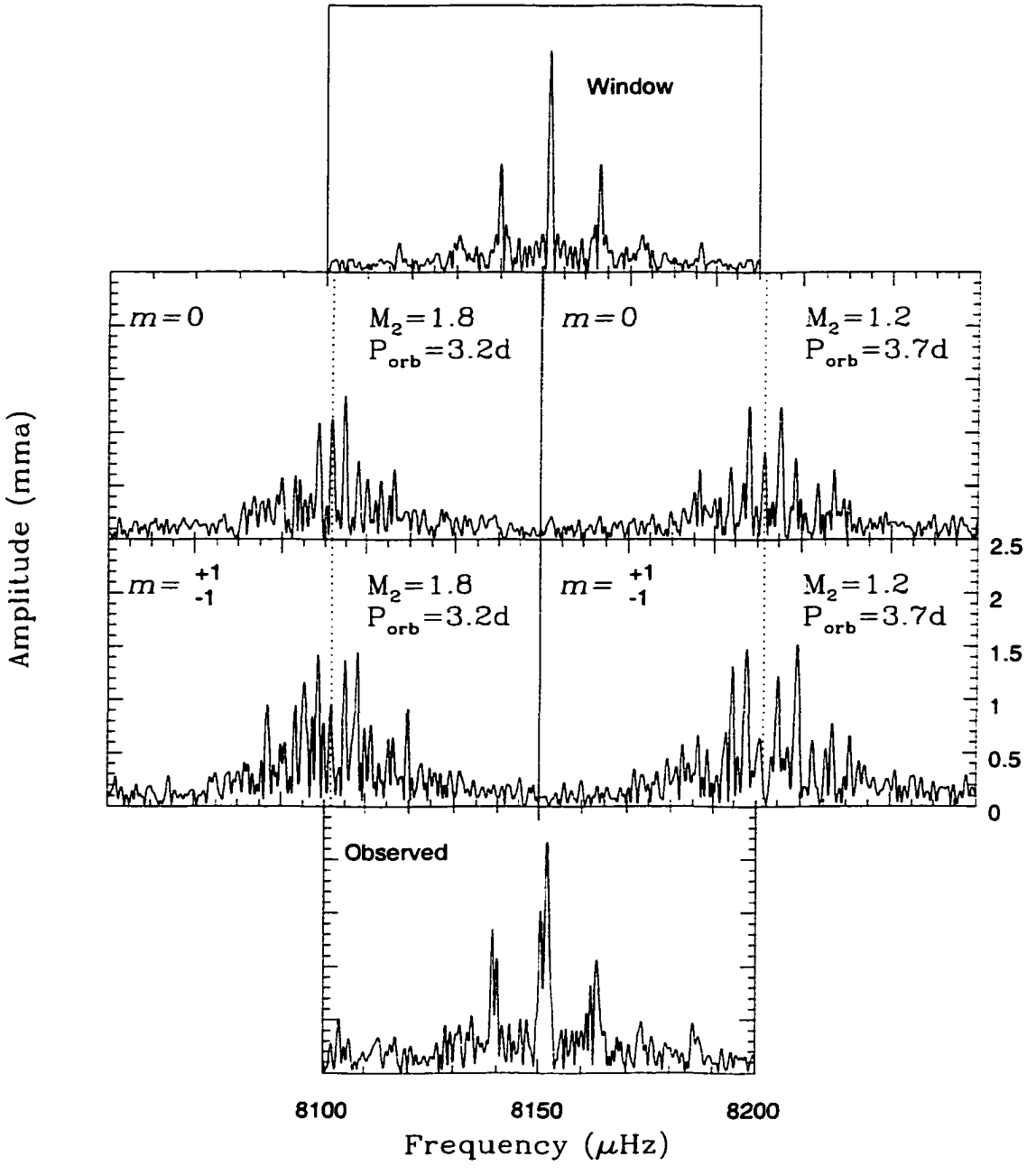

Figure 5.1 Comparison of simulated data to observed data for PB 8783. Top Panel: Unperturbed data window. Middle Panels: Simulated data as labeled. (Dashed line indicates position of observed pulsation frequency.) Bottom Panel: Observed temporal spectrum (from O'Donoghue *et al.*, 1998).

Table 5.2 Comparison between Model and Observed modes in PG 1605. (From Kawaler, 1999).

Period [s]		Mode		
Star	Model	n	ℓ	m
528.7	531.3	7	1	+1
481.8	482.8	7	1	0
440.5	442.3	7	1	-1
475.8	471.8	13	2	0
364.6	364.2	4	1	0

5.2 PG1605

PG 1605 has the lowest log g of any sdBV star to date; the low log g, coupled to the T_{eff}, means it is the most evolved sdBV star. In such an evolved state, the stellar radius is relatively large and stratification is greater than on the ZAEHB. This structure is ideal for trapping modes (see §2.2.4), not through a composition transition, but through the natural density gradient. Assuming that PG 1605 has such trapped modes, resulting in a mixture of p and g modes, Kawaler (1999) was able to match all five high-amplitude modes as listed in Table 5.2.

Kawaler's (1999) best-fit model has a mass of $0.4740 M_{\odot}$, an H shell of $0.004 M_{\odot}$, $T_{\rm eff} = 31,500K$, $\log g = 5.33$, and a radius of $0.157 R_{\odot}$, all within agreement of spectroscopic results (Heber, Reid & Werner, 1999). However, to match the observed pulsations, PG 1605 must have a fairly high rotation velocity (130 km/s unprojected). This rapid rotation was confirmed by Heber, Reid, & Werner (1999) who measured $v \sin i$ of 39 km/s, making PG 1605 one of the fastest rotating sdB stars seen. An inclination of 17° is needed to be consistent with the observed splitting. The relative amplitudes of the m=0 (27.4 mma) and $m = \pm 1$ modes (13.9 and 1.8 mma respectively) are consistent with a relatively low inclination. At such an angle, $m \neq 0$ modes are affected by geometric cancellation (see Figure 2.3 or §8.2), but not knowing the intrinsic amplitudes means that this does not rule out Kawaler's (1999) model. Another pulsation (364.6 seconds) is identified by Kawaler (1999) as an ℓ=1, m=0 mode. Assuming that Kawaler (1999) is correct and the corresponding $m = \pm 1$ modes exist in the star, there

should be pulsations detected around 341 and 391 seconds. In fact, there *are* pulsations at 339.82 and 391.25 seconds (Kilkenny *et al.* 1999); very close to where they should be based on Kawaler's (1999) model, though they are of comparatively low amplitude (1.1 and 1.3 mma respectively).

5.3 Feige 48

Feige 48 shows five distinct pulsation modes in its temporal spectrum. There is a group of four modes near 350 seconds and a single mode at 378.5 seconds. The three shortest period modes also have the highest amplitudes, over three times higher than the two longer period modes.

Keck spectra obtained by Heber, Reid & Werner (2000), limit the rotation velocity of Feige 48 to $v \sin i \leq 5$ km/s. We can limit the rotational splitting if we assume $i = 90°$, $v < 5$ km/s, and $R = 0.15 R_{\odot}$ (Feige 48 has already left the ZAHB, so is probably at least twice that size). These parameters give a rotation period of 1.5 days and a frequency splitting of 8μHz.. This is close to a splitting observed in the data of 13 μHz ($f_3 - f_2 = 13.3$). There are also two other, nearly equal splittings of $f_4 - f_3 = 26.3$, and $f_5 - f_4 = 29.1 \mu$Hz in the data. To make these larger splittings match the constraints on rotation velocity ($v \sin i < 5$ km/s), we could reduce the angle i.

The most obvious assumption (based on §2.2.3) is that f_3, f_4, and f_5 is a rotationally split triplet with ℓ=1, m=-1,0,+1. Another choice is ℓ2, with either m=-2,0,+2 or m=-1,0,+1. Since $f_3 - f_2 = 13.3 \sim 26.3/2$, we could also assume that f_2, f_3, and f_4 are three parts of a quintuplet (ℓ=2 mode). Allowing all of these ℓ and m combinations, we searched models of appropriate log g and $T_{\rm eff}$ for a match to the observed periods.

We found only one model that fit any of these possibilities and was in the error box for log g and $T_{\rm eff}$. Small changes in the age of this model produce substantial changes in the model pulsation periods, destroying the fit to the observations. Likewise, a change in envelope layer thickness quickly ruined the fit to the observed pulsation periods. A comparison between the observed and best-fit model periods is shown in Table 5.3 while Table 5.4 compares the physical

Table 5.3 Comparison of observed pulsation periods with best-fit evolutionary model of appropriate T_{eff} and log g for Feige 48.

	Δf	Frequency	Period (sec)		Model		
Number	μHz	μHz	Star	Model	n	l	m
1		2641.99	378.5				
	195.61						
2		2837.60	352.4	352.3	0	0	0
	13.23						
3		2850.83	350.8	350.9	1	1	-1
	26.33						
4		2877.16	347.6	347.4	1	1	0
	29.12						
5		2906.28	344.1	344.3	1	1	+1

parameters to those observed. In fact this model fits surprisingly well: the model periods are within 0.2 seconds of those observed, we fit 4 of the 5 observed modes, the model temperature agrees to within 150 K, and log g agrees to within 0.02 of the measured values, well within the errors. The model does not explain one mode. It's possible this mode is a higher order ℓ value (which we are not looking for, nor expecting to see), or a trapped mode (which is not expected from our model).

Our model has a rotational splitting of 27.7μHz which implies a period of 0.4178 days (10.0 hours). With a radius of 0.198$R_{\odot}$, this model would have an equatorial rotation velocity of 24 $km \cdot s^{-1}$. To match the constraints of Heber, Reid, & Werner (2000) requires $i = 12^{o}$. If we use the value determined by Heber, Reid, & Werner (2000) for only the unblended spectral lines in Feige 48 of $v \sin i \leq 10 km \cdot s^{-1}$, our inclination limit increases to $i \leq 25^{o}$.

Another solution would be to fit a model with one of the other configurations described above; namely assume the observed pulsations are a subset of an ℓ=2 quintuplet. However none of our evolutionary models, within the physical constraints of log g and T_{eff} came close to matching the ℓ=2 mode for any combination of m (i.e. none had an ℓ=2 mode between 344 and 352 seconds).

Table 5.4 Comparison of observed stellar parameters with models for Feige 48.

	Mass	He shell mass	$T_{\rm eff}$	$\log g$
Spectroscopy			29500 ± 300K	5.50 ± 0.05
Model	0.4725	0.0025	29635	5.518

5.4 PG1336

The original goal of observing PG 1336 with the WET (Xcov17) was to identify pulsation modes by finding rotationally split non-radial modes in the temporal spectrum. We know where in frequency to look for such modes because it is assumed that PG 1336 is tidally locked in synchronous rotation with its companion. However, as is evident in Figures 4.11 and 4.13, because of the reduction procedure, gaps are produced in the data due to the eclipses which create aliases separated from the true pulsations by half integer multiples of the orbital period. It is important to understand how the modes would separate themselves from these aliases. Typical splitting coefficients ($C_{n\ell}$), derived from evolutionary models, for low order modes typical for sdBV stars range from 3% to <0.08%. It would take ~3.4 days to resolve splittings with $C_{n\ell}$ of 3% from the orbital alias and over 126 days to resolve splittings with $C_{n\ell}$ <0.08%. For small splitting coefficients, this makes it extremely difficult to separate real, rotationally split modes from aliases caused by the extracted eclipses. We refer back to our "rule of thumb" given in §2.1.3: "never trust a peak that resides on another peak's alias, unless there is a very compelling reason to do so." In this case, that compelling reason is that we expect to see *real* pulsations at the same place as the orbital aliases. Still, we will not completely trust these reductions unless those peaks are sufficiently larger in amplitude than we expect the orbital alias to be.

From Table 4.11, we note that PG 1336 is observed to pulsate in at least 22 modes. With so many observed modes in such a small frequency domain, it would be easy to create a model that matches four or five random modes (especially allowing for $m = \pm 1$ modes from the model) and claim success. However, that model would probably not represent a unique fit to the real star.

Table 5.5 Comparison of Model to Observations in PG 1336.

Period [s]		Mode		
Star	Model	n	ℓ	m
186.2	185.9	1	2	+1
	182.2	1	2	0
179.0	178.5	1	2	-1
173.7	174.3	1	0	0

	Observed	Model
$\log g$	5.7 ± 0.1	5.726
T_{eff}	33,000±1000	31,200

5.4.1 Xcov 17

Out of the 15 modes observed in the Xcov 17 data, the most likely rotationally split modes are $f1$-$f7$, where the amplitudes are sufficiently large to rule out aliasing and the splitting is far enough away from half the orbital period ($\sim$13μHz) that it is unlikely to be an orbital alias. We begin by assuming that the three largest amplitude modes are real (they are the most obvious modes in the temporal spectrum), that $f1$ and $f7$ are rotationally split $m = \pm 1$ modes, and that $f8$ is a radial mode, as it shows no splitting. Then the goal is simplified: Create a model that has a non-radial mode ($m = 0$) centered between $f2$ and $f7$ (at 182.6 seconds) and a radial mode at $f8$ and simultaneously match (to within 2σ) the $\log g$ and T_{eff} constraints.

The model that most closely matched these constraints is given in Table 5.5. To match our pulsation criteria, the model is outside the 1σ error in T_{eff}. Another flaw is that the non-radial mode that matches our observations is an ℓ=2 mode, for which (as will be shown in section 6.1.2) the $m = \pm 1$ splittings should not be observed outside of eclipse at an inclination of 81°. Fortunately, PG 1336 is a unique system that may allow another means of mode identification as will be discussed in Chapter 8.

5.4.2 Xcov 21

Analysis of the temporal spectrum determined from the Xcov 21 data reveals complications that we did not recognize from Xcov 17. We now believe PG 1336's pulsation axis may be aligned toward its companion and therefore changing its orientation with respect to us. This will be explored further in Chapter 8.

Table 5.6 Observed periods (from Xcov21) of PG 1336 split by an integer number of rotation frequencies.

Modes split by $\sim 1 f_{orb}$

Modes	Δf-114.59 μHz	f_{center} μHz
$f2, g6$	0.19±0.02	NA

Modes split by $\sim 2 f_{orb}$

Modes	Δf-229.17	f_{center}
$g1, g2$	-3.16±0.03	4998.10
$g3, f5$	-3.92±0.02	5376.67
$g4, f7$	0.04±0.02	5471.03
$f1, f7$	-12.89±0.01	5477.51
$f1, g7$	-0.03±0.01	5483.96

Modes split by $\sim 3 f_{orb}$

Modes	Δf-343.77	f_{center}
$f13, f15$	4.36±0.04	~7715 or ~7830

Modes split by $\sim 4 f_{orb}$

Modes	Δf-458.36	f_{center}
$f3, f10$	-0.13±0.02	5662.46

Since we found several additional pulsation frequencies in the Xcov 21 data that we did not in the Xcov 17 data, we again looked for those spaced at integer numbers of the orbital frequency. Table 5.6 lists 7 such frequency pairs. Column 1 lists the pairs from Table 4.11. Column 2 provides the difference between the orbital splitting and the splitting observed, while column 3 lists possible centers (m=0) for the splittings. Splittings of 3–4 f_{orb} are not expected from simple nonradial pulsation theory; their origin will be explained in Chapter 8.

5.5 Conclusion

In this chapter, we applied a standard tool of asteroseismology to the sdBV stars in this thesis Our results will be summarized on a star by star basis.

PB 8783

- The data for PB 8783 shows tantalizing evidence for rotationally splitting despite very small pulsation amplitudes. PB 8783 needs to be observed with larger telescopes to increase the signal to noise and reduce the noise in the temporal spectrum.

- PB 8783 hints to a rotation period of 12.3 days, but a longer data set is required (see above point concerning data quality) to resolve other rotationally split modes in the temporal spectrum.

- Although PB 8783 has the most massive companion detected so far, the temporal spectrum does not show signs of orbital effects. This challenges the admittedly weak upper limit to an orbital period as described by Jeffery & Pollacco (2000). Such an orbital period (unless at a very low inclination) would be detected in the temporal spectrum of O'Donoghue *et al.* (1998).

PG 1605

- We reviewed the model fit by Kawaler (1999) and noticed that two other modes in the temporal spectrum fit his model.

- Kawaler's (1999) model predicts a rotation velocity of 130 $km \cdot s^{-1}$. With $v \sin i = 39 km \cdot s^{-1}$ from Heber, Reid, & Werner (1999), this indicates an inclination, $i = 17°$.

Feige 48

- Of the 5 pulsation modes detected, two appear split by $\sim 13\mu$Hz and three are split by $\sim 27\mu$Hz.

- Our model fits the pulsations to better than 0.2 seconds for all but one low amplitude mode.

- The model is nearly a perfect match for measured values of log g and T_{eff}.

- Constraints on rotation velocity by Heber, Reid, & Werner (2000) would require an inclination of $i = 12°$ (or 25° using $v \sin i \leq 10 km \cdot s^{-1}$ from the unblended lines).

PG 1336

- Using only the 3 highest amplitude modes, a model was fit to the data.

- Unfortunately, the model would require observing modes that are not likely to be observed at the known inclination of81°.

- PG 1336 presents a rich and complex temporal spectrum that requires new tools for analysis. Those tools will be developed and applied in Chapter 8.

CHAPTER 6. STABILITY AND EVOLUTION OF PULSATIONS

In Chapter 5, we applied *pattern matching techniques* to the pulsation periods listed in Chapter 4. In this chapter, we apply a second tool (described in §2.4.4 with an example in §2.5.4), $O - C$ analysis. This technique examines the phases of pulsations as a means to constrain evolutionary changes in the star or detect binary companions. To determine the phases and amplitudes for the observed pulsations as a function of time, we first reduce the data as described in Chapter 2 to find the best period using all of the available data. Then using the best period as a fixed parameter, the phases and amplitudes for subsets of the entire data set are determined using LSQ. As described in §2.4.4, for this method to be successful, it is important to have long lived (temporally stable) modes that are sufficiently separated from neighboring peaks to allow unambiguous phase determination in relatively short subsets of the data.

If a star meets the above criteria, then it is observed over many seasons [perhaps even decades (Kepler *et al* 2000), though no stars in this thesis have yet been observed for so long]. Typically many adjacent runs are combined together to increase the accuracy of the phase, and the phases are plotted in the $O - C$ diagram. Linear trends are removed (such trends are due to small errors in the period determination) and the phases are fit to determine what changes (if any) have occurred over the duration of the observations. Phase differences are then compared to evolutionary changes in models (which provide the theoretical value for evolutionary changes).

We follow the same order as the last two chapters in that we begin with PB 8783; the subject of a multisite campaign in 1996. We analyze the multisite campaign in search of stable modes for the possibility of following PB 8783 over several seasons. Additionally, since PB 8783

is a known binary, we will examine the data for signs of the binary period.

Next we examine data acquired for PG 1605. We have both the multisite campaign and two seasons of follow-up observations. Since PG 1605 is the most evolved sdBV star, it is also the most likely to show signs of evolutionary changes in its $O-C$ diagram.

For Feige 48, we have obtained nearly 3 years of observations from which to assemble an $O-C$ diagram. Feige 48 is the coolest sdBV star and lies midway between PG 1605 and the majority of the class in log g. As such, we expect that Feige 48 is also an excellent candidate to examine for evolutionary changes as it is nearing the end of the core helium burning phase.

PG 1336 is typical of sdBV stars in T_{eff} and log g, but with a close M-type companion. The orbital light crossing time is estimated at <2 seconds, which will put a limit on the accuracy possible in the $O-C$ diagram. We will examine differences between the two multisite campaigns.

6.1 PB8783

Eleven different pulsation periods were detected in PB 8783 by O'Donoghue *et al.* (1998) spanning a range of 43 seconds (from 94 to 137 seconds). The largest amplitude modes span 12 seconds in period. Within this range, there are two modes that are reasonably well separated, the 127.06 (7870.32) and 123.58 (8092.08) second (μHz) periods (frequencies). Their separation of $\sim$220μHz mean that they can be resolved in a single night (1.5 hours). However, as noted by O'Donoghue *et al.* (1998), there is considerable amplitude variability in PB 8783. Therefore we must first determine if modes exist that are stable enough.

We processed the data of O'Donoghue *et al.* (1998) as outlined in Chapter 2. We applied our least squares fitting (LSQ) program to the 7 highest amplitude pulsations detected. Our results are displayed in Figure 6.1. Though PB 8783 has variable amplitude modes, it is clear in Figure 6.1 that the two well separated modes, $f4$ and $f5$, appear to be stable in amplitude. As expected, it is impossible to resolve each member of the observed 122 second triplet ($f3$, $f1$, and $f6$) within the multisite campaign and errors dominate the calculated amplitude.

We calculated the phases for the 7 highest amplitude modes. Our results are shown in

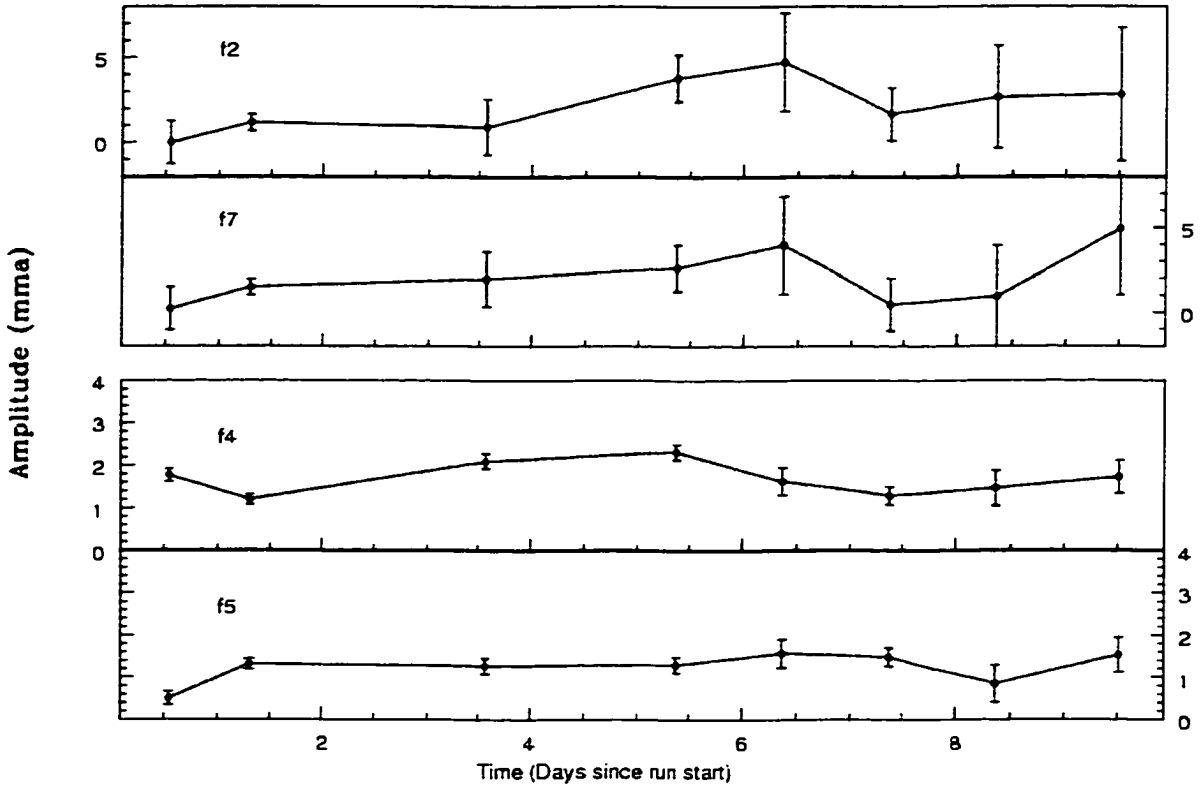

Figure 6.1 The amplitudes of the 4 best resolved modes (as labeled according to Table 4.2) for each day during the multisite campaign on PB 8783. Note that the top and bottom panes have different ordinants.

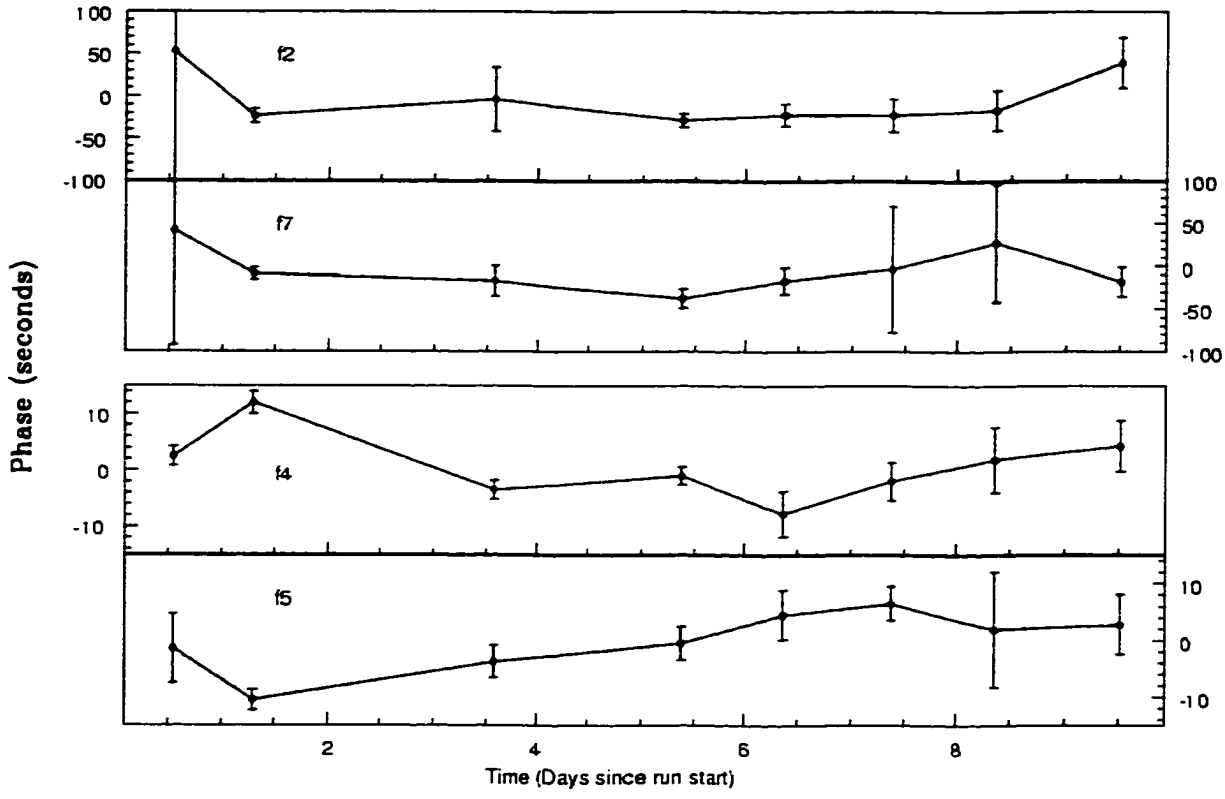

Figure 6.2 The phases of the 4 best resolved modes (as labeled according to Table 4.2) for each day during the multisite campaign on PB 8783. Note that top and bottom panels have different ordinants.

Figure 6.2 and again show that $f4$ and $f5$ are stable modes. The length of the entire run (14 days) just covers one beat period (12 days) of the three modes, so the $f1$, $f3$, $f6$ triplet is just barely resolved and their individual phases and amplitudes are not well determined for the shorter chunks of data.

Some of the modes in PB 8783 meet the requirements outlined at the beginning of the chapter; it is in a known binary, which may introduce a periodic signal in the $O-C$. If the orbital period is less than a few days (which seems doubtful after Chapter 5's conclusions), then it will create an additionally uncertainty in each phase point. If the period is longer than a few months, then $O-C$ measurements are actually a good way to determine the orbital period, but over a longer period of time than spanned by these observations. Additionally, since PB 8783

has the largest log g if any sdBV star to date, it is expected that it is close to the ZAHeMS, so it will be one of the slowest evolving. Models suggest a time scale for period change of $\sim 10^8$ years. With this value for $P/\dot{P}$, equation 2.13 tells us that an accumulated phase change of 10 seconds will take nearly 4 years. Given the importance of such a measurement, a concerted effort would be worthwhile.

Given the data already in hand, we can address the question of short period binarity. Figure 6.3 shows the $O - C$ values for the two stable modes in the top two panels. The two modes appear to have trends in opposite directions. Since all modes should be affected in the same way by orbital effects, we averaged the two modes together (adding the errors in quadrature) as shown in the bottom panel by the errorbars. Obviously, the simplest conclusion is that our results are consistent with *no change* in phase over the nine day period of this data. We use this to place some limits on companions to PB 8783 at orbital periods between 1 and 12 days The maximum orbital light crossing time allowed by the data is a mere 10 seconds at the 1 σ level. This eliminates at the 5σ level the 57 seconds required to match the parameters of Jeffery & Pollacco (2000) for a three day orbit. This clearly rules out a binary orbit at the long end (i.e. $\sim$3 days) of the constraints of Jeffery & Pollacco (2000), in good agreement with what we found in Chapter 5. As the inclination increases, the constraints imposed by Jeffery & Pollacco (2000) move to shorter orbital period. For an orbital period of 1.5 days (the short period blue curve in the bottom panel of Figure 6.3), the inclination would need to be less than 23° for the F-type companion to fit within our constraints. This is consistent with Jeffery & Pollacco (2000), as an upper limit. Our data also rule out any periods longer than three days, and up to 12 days for the F-type companion (at high inclinations). The red curve in the bottom panel of Figure 6.3 is the best fit for a 3 week orbital period and follows the natural trend of the data.

6.2 PG1605

PG 1605 is the senior citizen of the pulsating sdB stars. Evolutionary models indicate that core He burning has ceased and helium burning is now proceeding through a shell; a phase

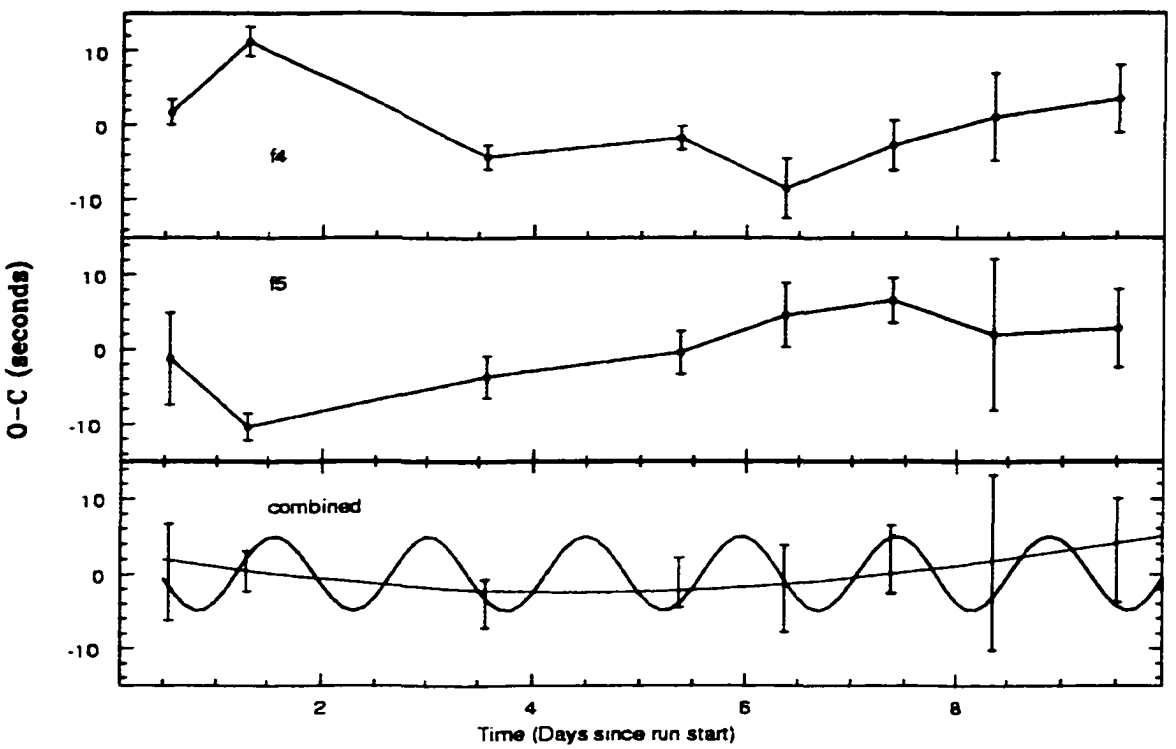

Figure 6.3 $O-C$ of the two stable modes found in PB 8783. The ordinant shows departure from the mean $(O-C)$ through the run. Bottom panel: A combination of the two modes, with a sine curve appropriate for 1.5 (blue) and 12 day (red) orbits fit within the errors.

which is predicted to last only $\sim 10^7$ years (Saffer *et al.* 1994). During shell helium burning, PG 1605 is expanding as the core heats up and He burning proceeds closer to the surface.

In the spring of 1999, I initiated a project with Dave Kilkenny at SAAO to monitor PG 1605 over several seasons to search for phase changes in its dominant modes. Table 4.4 listed the observations we obtained over the 1999 and 2000 observing seasons. I was able to obtain over 81 hours of data between Fick and McDonald observatories while Dave Kilkenny (with collaborators at SAAO) obtained 41 hours of data from South Africa. Including the multisite campaign and discovery data (kindly provided by Chris Koen and Darragh O'Donoghue), we have data spanning over four years.

From evolutionary models, we expect that the $\dot{P}/P$ will be $3 \cdot 10^{-15} s^{-1}$ for radial modes. Over the 4.3 years of data we have, this $\dot{P}$ would result in a phase change of 28 seconds for a 364 second mode. This provides a lower limit to the expected $\dot{P}$ as trapped modes (which is the case in PG 1605) can be more sensitive to changes in radius (Kawaler & Bradley, 1994).

To look for small changes in phase, the mode amplitude must be stable. Figure 6.4 shows the evolution of two regions of power over the duration of our data.The left panel shows the main region of power, which switches from 2075 to 2102 μHz during this interval. We were unable to use this highest amplitude region because the mode density is high and obvious amplitude modulation occurred throughout our data set. The right panel shows a region near the mode at 2742 μHz. This is the fourth highest amplitude mode and seems separated from all but the lowest amplitude modes, making it favorable for our phase analysis. This mode appears to be stable, although the amplitude starts to diminish in the JD 2451757-62 data set (Group VI).

In determining the pulsation phases for different groups, the data for each group are combined. For PG 1605, our combined data sets are listed in Table 6.1. A least squares solution is determined for the amplitude and phase of each observed pulsation period listed in Table 4.3 for each group in Table 6.1 (with the frequency fixed at the best value for the entire data set).

The results of the LSQ fit are plotted in Figure 6.5. The top panel shows our $O - C$ results while the bottom panel indicates the pulsation amplitude determined at each phase

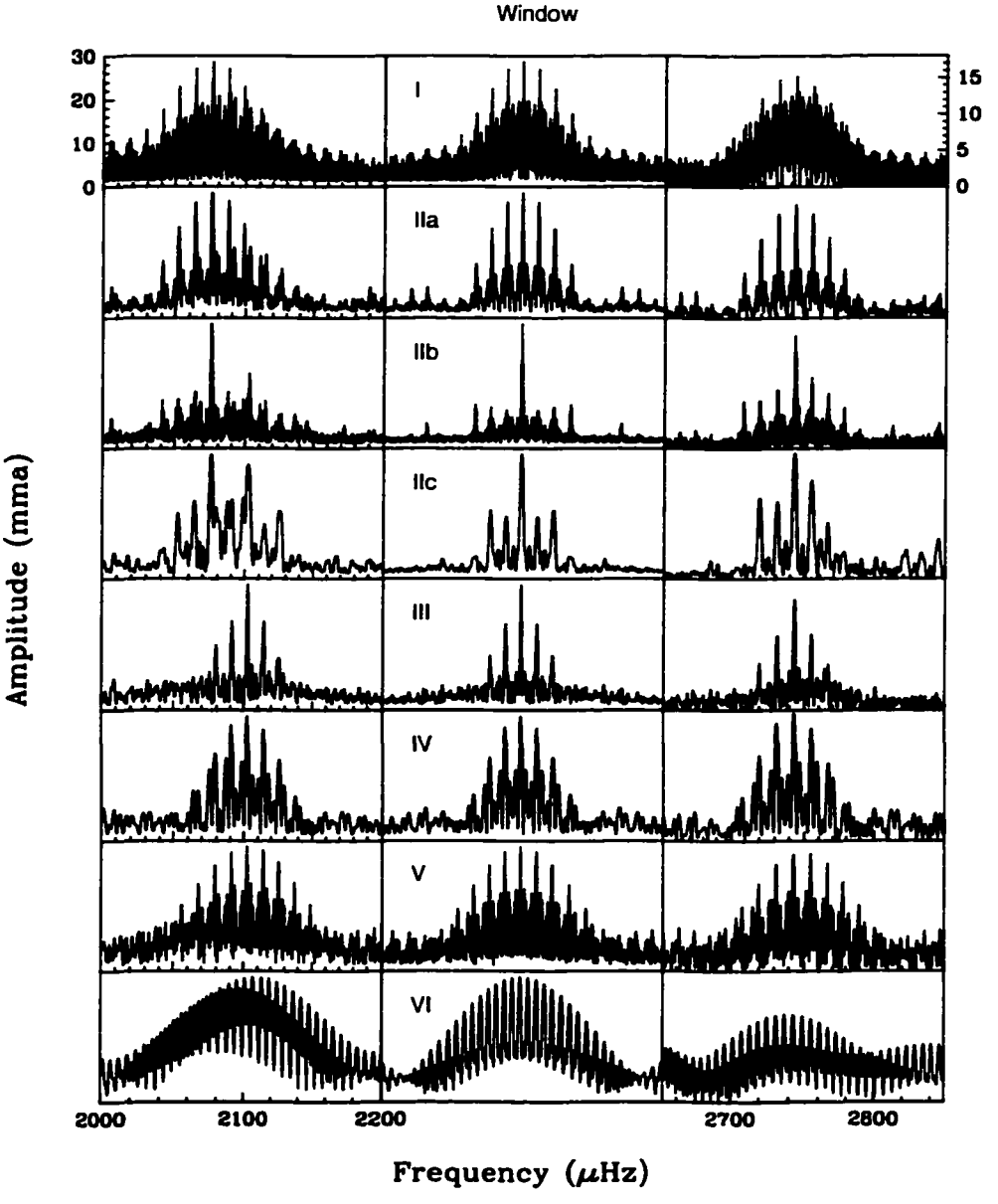

Figure 6.4 Stability of pulsation modes of PG 1605. Left panel: Region of largest power. Right panel: Region around 2742 μHz. Middle panel: Spectra windows with labels for Groups provided in Table 6.1.

Table 6.1 Groupings used for phase calculations of PG 1605. Note that the multisite data contains subgroups used in Figure 6.4.

Group	Inclusive dates	JD 2450000+
I	Discovery data (1996)	195-334
II	Multi-site run (1997)	547-581
IIa		547-558
IIb		566-575
IIc		576-581
III	5/12-5/24, 1999	1310-1323
IV	6/14-6/18, 1999	1342-1347
V	7/20-8/1, 1999	1379-1391
VI	8/1-8/5, 2000	1757-1762

Table 6.2 Least squares determined frequencies, in μHz, near 2742μHz by year for PG 1605. Amplitudes (in mma) are in parenthesis.

f_1	f_2	f_3	Year	JD 2450000+
2742.895 (13.9)		2751.274 (7.1)	1996	195-334
2742.665 (16.4)	2742.340 (8.1)	2754.039 (4.8)	1997	547-581
2742.617 (13.4)		2754.932 (7.6)	1999	1310-1391
2743.086 (6.6)			2000	1757-1762

point for the 2742μHz mode.. The phase zero point is arbitrarily defined to be the time of first maximum during the multisite campaign (Kilkenny *et a.*, 1999). As is obvious in the plot, the phase varies widely, including over 200 seconds in the 1999 data alone. This compelled me to look further into this region of power. I combined the data for each year together and re-calculated the least-squares solutions given in Table 6.2.

The multisite data hints at what may be the problem. There is another mode $\sim 0.3\mu$Hz away from the 2742.6μHz mode at 2742.34μHz. This new mode only appears in the multisite data, but with half the amplitude of the 2742.6μHz mode. This new, 2742.340μHz, mode would remain unresolved in the other data sets as they have poorer temporal resolution. This means the 2742.340μHz mode will not be useful for future phase calculations. This is unfortunate as it leaves no modes, stable in phase, to be used as a gauge of the evolution of PG 1605.

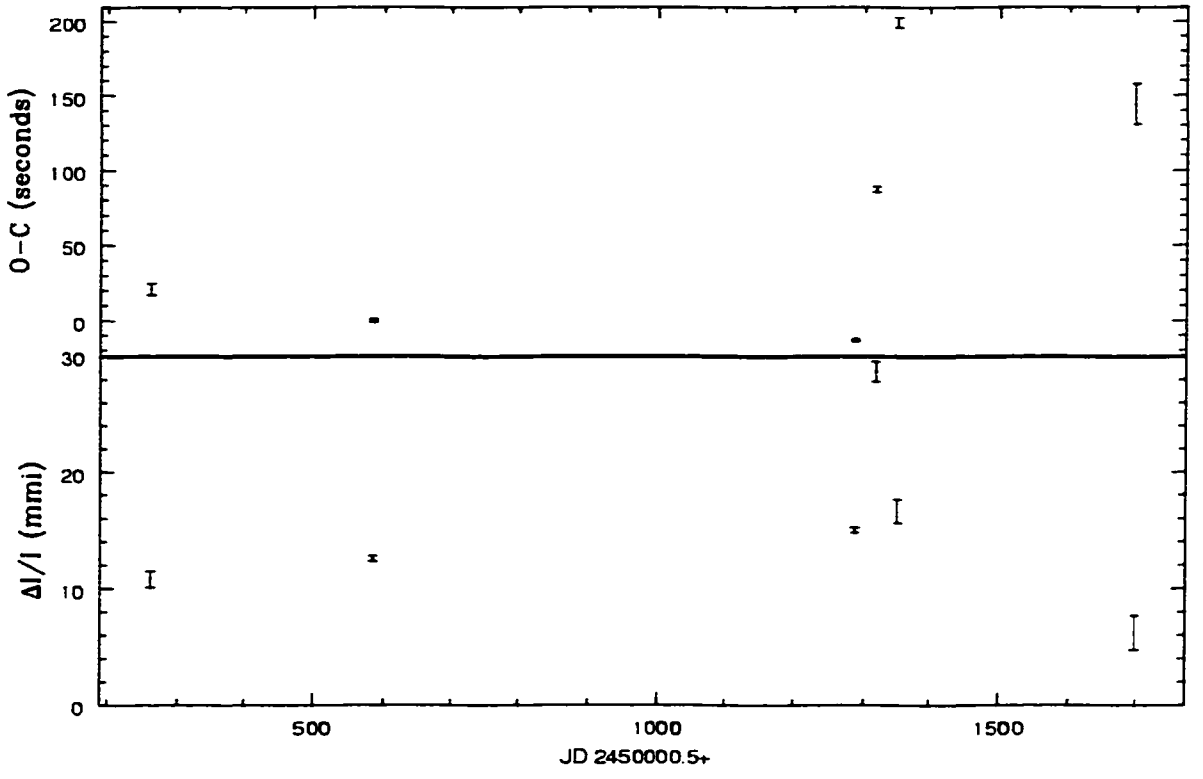

Figure 6.5 LSQ results for the 2742μHz mode in PG 1605

6.3 Feige 48

Feige 48 is the coolest sdBV star and intermediate between PG 1605 and most other sdBV stars in log g. As such, we would expect Feige 48 to have a $\dot{P}$ smaller than PG 1605, yet larger than all other stars in the class. Our best fit model (see §5.3) has a $\dot{P}=1.714 \cdot 10^{-5}$ seconds per year. With ~3 years of usable data, Equation 2.13 indicates the phase of a 350 second period should change by ~14 seconds in that time.

We were able to detect consistent and stable modes in our data (see Table 4.5 for a list of data runs). As in §6.2, we combined temporally adjacent observing runs to increase the accuracy of the calculated phase. A single phase was calculated for each observed pulsation mode in Table 4.8 for each data group in Table 4.6 (Note that Groups III and V were divided into two subgroups each due to the length of the runs). The resulting $O-C$ diagram is shown

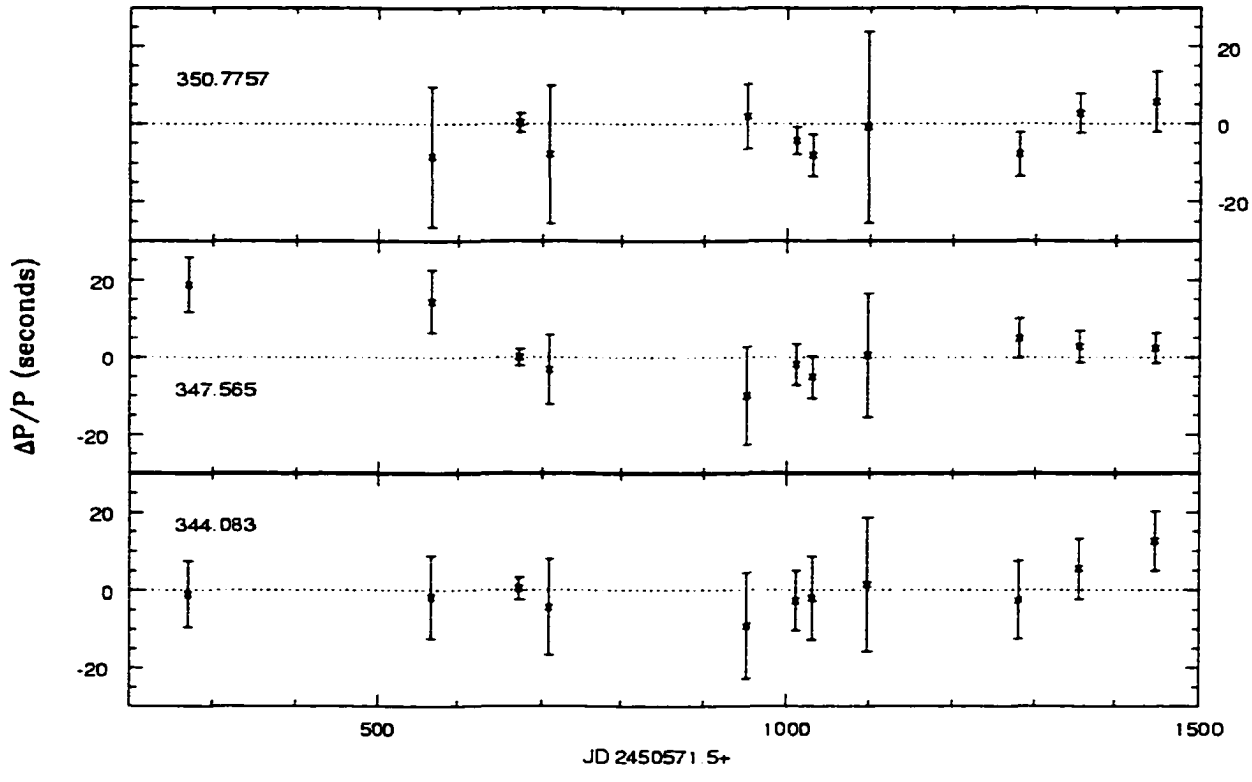

Figure 6.6 $O-C$ diagram for Feige 48 for 3 modes with the period listed.

in Figure 6.6 for the three highest amplitude modes (with the period indicated in each panel). The phase zero point is defined to be the phase at our best data set from March 1999. The combined $O-C$ data of the three highest amplitude modes has $\dot{P}/P=4.9\times10^{-16}\pm5.3\times10^{-16}$, which provides a lower limit on an evolutionary timescale of 3.1×10^{7} years.

A phase change of ~14 seconds is near our detection limit with our current data set. However over a slightly longer time period, say 4 years, the same theoretical $\dot{P}$ (1.714×10^{-5} seconds per year) would have a phase change of ~25 seconds; a noticeable shift. The key here is patience. We have shown that Feige 48 is an excellent candidate for an evolutionary analysis using $O-C$ techniques; the modes are phase stable and our limit on $\dot{P}$ is within that predicted by theory. We just have to continue collecting data for a few more years and we should be able to measure $\dot{P}$.

What we do not need patience for is to place useful limits on a companion to Feige 48. Any

companion must create a phase change less than 5.35 seconds (to fit within the 1 σ errors) over the scale of years[1]. Figure 6.7 graphically presents our sensitivity to companions. The X-axis is continuous across both panels, though the scale changes, while the Y-axis is discontinuous in that we re-scale from solar masses to Jupiter masses. According to the left panel, we can rule out stellar size companions with periods close to a month or more at a 1σ level. The right panel indicates that even planets not much larger than Jupiter would be detected in our data for orbital periods of 2 to 3 years at a the 1σ level. In the short period case (periods under a few months), the constraint is the limit imposed by the errors of the data; in the long period case it is the flatness of the $O - C$.

Recall that Feige 48 is a horizontal branch star that has lost considerable mass between the red giant branch and its current evolutionary state. Any companion separated by more than $\sim$1 AU is too distant to become a common envelope binary (or vaporized as the case would be for planets) and would have its semimajor axis approximately doubled as Feige 48 loses approximately half its mass during the red giant phase. As discussed in §3.1.3, if a companion is too close, it will produce a short period binary (periods on order of weeks or less) after a common envelope phase. If the companion is distant enough to avoid a common envelope phase (or vaporization), then its orbital period should be on the order of a few years or more.

Our data are sensitive to the extra solar "warm Jupiter" type planets being detected[2] at a distance of 1-3.3 AU. Orbital separations less than $\sim$1 AU would not survive the red giant phase. Of course as we continue to observe Feige 48, we will become more sensitive to longer period orbits. However, our data do not rule out a companion in a short period binary or at low inclination.

The results of our analysis yields that Feige 48 is consistent with *not* being in a binary (within the limits stated above), but is consistent with our evolutionary models (and also consistent with *no* evolution as well). It also indicates that using the $O - C$ diagram to detect planets around evolved stars is possible, though in this case we did not detect any within the limits of our data. The next few years should prove very exciting for Feige 48.

[1] We assume we could detect an orbital period up to twice our observed timebase.

[2] A complete list of extra solar planets is maintained at http://www.obspm.fr/encycl/catalog.html.

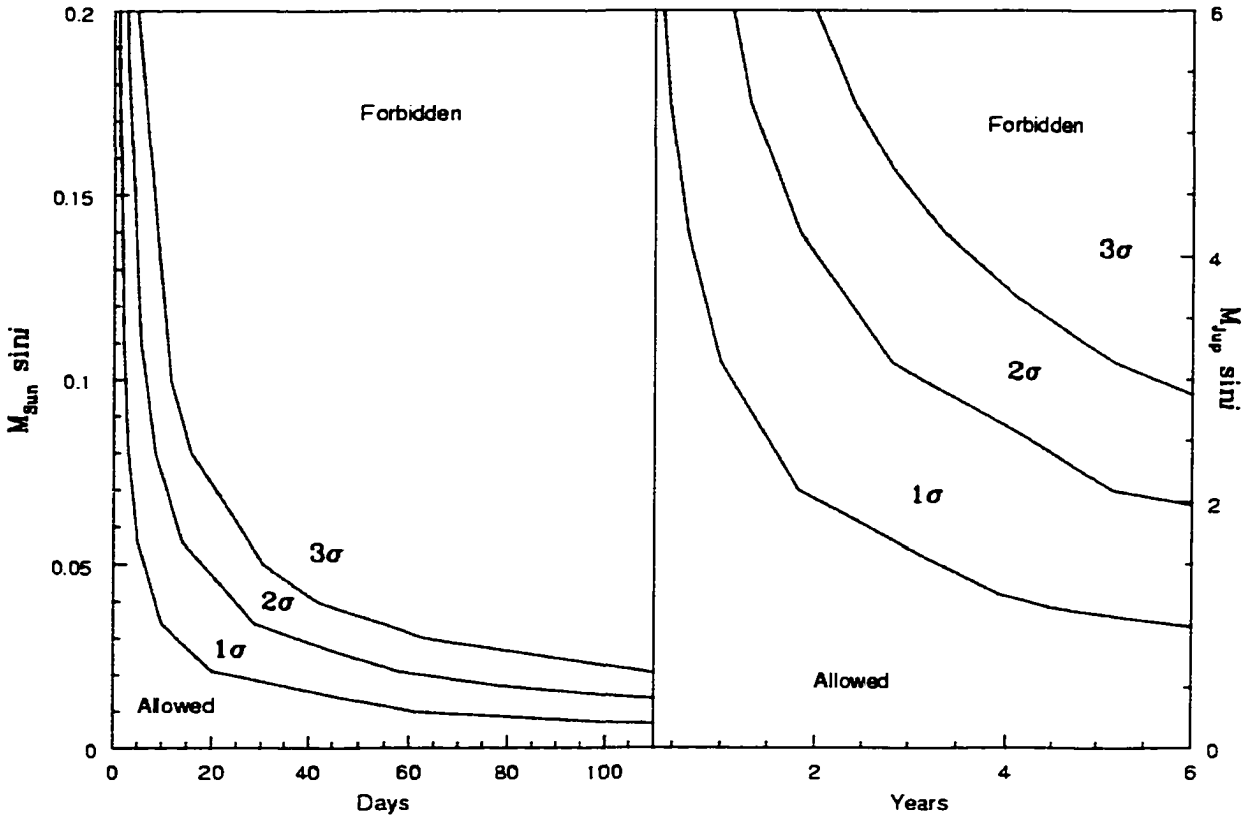

Figure 6.7 1σ, 2σ, and 3σ limits on any companions to Feige 48. The time axis is continuous between panels, but changes scale from days to years. The mass axis is discontinuous between panels as the left panel is in solar masses and the right panel has units of Jupiter masses.

6.4 PG1336

For PG 1336, we have extremely good two epoch data. However, the two epochs are too far apart to be able to determine whether the pulsation phases are consistent or not. Also, like PB 8783, PG 1336 has a comparatively large log g, which means a longer evolutionary timescale, and therefore small $\dot{P}$. However, we can examine the pulsation modes and determine if the modes appear to be temporally stable.

Comparing Table 4.9 to Table 4.11, we clearly see that all modes with amplitudes larger than 1 mma are recovered. In fact, of the 15 modes detected in the Xcov 17 data, only $f6$ and

$f14$ are missing from the Xcov 21 data.

6.5 Conclusions

In this chapter, we examined the feasibility of applying phase analysis techniques to the four stars studied in this work. We determined that three of the four stars appear to have modes stable enough to warrant $O-C$ studies. For the star most likely to evolve the fastest (PG 1605), we have not found any pulsation modes stable enough for an $O-C$ analysis.

We find that:

- Though PB 8783 was known to have variable amplitude modes, it has two modes that appear to be stable over the span of the multisite data used in our analysis.
- Our PB 8783 $O-C$ analysis rules out (at the 1σ level) an orbital period between 1.5 and 12 days; in good agreement with our findings in Chapter 5.
- PG 1605 does not have long-term stable modes in the main region of power.
- The apparently stable 2742μHz mode in PG 1605 has another mode only $\sim 0.3\mu$Hz away and at up to half the amplitude. This makes the phase of the 2742μHz mode unstable over the timescale of years, and thus unusable for $O-C$ analysis.
- The pulsation modes in Feige 48 appear to have stable phases over the length of our data ($\sim$2.5 years).
- $|\dot{P}/P|$ for Feige 48 is $< 5.3\times10^{-16}$ based on our $\sim$3 years of data and provides a 1σ lower limit on the timescale for evolutionary change of 3.1×10^{7} years.
- The timescale limit for Feige 48 is consistent with that predicted by evolutionary models.
- We also determined that Feige 48 is an excellent candidate for future $\dot{P}$ measurements which could be achieved within the next two to three years.

- We conclude that Feige 48 is not a binary star within interesting limits; any companion would necessarily need to be in a short period binary (a period of a week or less) or at a low inclination, i.
- Our Feige 48 data are also sensitive to the detection of Jupiter-sized planets in our $O-C$ diagram for periods under $\sim$6 years (with a dependence on inclination i).
- PG 1336 has modes stable in period over the course of the two years for which we have data.

CHAPTER 7. STUDIES OF THE ENTIRE GROUP

In Chapter 5, we applied the first of our asteroseismological tools, *pattern matching*, to our four sdBV stars, and were rewarded with one good model match. In Chapter 6, we applied a second asteroseismological tool, $O-C$ analysis, and again were rewarded with nice constraints for one star, with at least one other remaining as a candidate for further $O-C$ studies. In this chapter, we will apply the third previously identified tool of asteroseismology, *ensemble analysis*, to the first 13 sdBV stars for which we have the best data available.

In applying this tool, we want to examine the class of pulsating sdB stars as a whole. We begin by trying to correlate the pulsations with observables (such as T_{eff} or $\log g$). Once we can identify the main dependence of pulsations on stellar parameters, we can correct the periods appropriately, examine the pulsation structure of the class, and look for groups of pulsations (as was done by Clemens, 1994b) as indicators of pulsation mode.

7.1 The Pulsation Dependence Across the HR Diagram

Figure 4.1 shows evolutionary tracks appropriate for the four stars in this work. As expected by Equation 2.1, radial and nonradial p-mode pulsation periods roughly scale with the sound crossing time of the star. Therefore, as we look across the HR diagram, we can quickly get an idea of how the pulsation periods should vary. Along the ZAEHB (solid line in Figure 4.1), $\log g$ increases with decreasing mass in the hydrogen envelope. So we should expect ZAEHB stars with thicker hydrogen envelopes to have longer periods. As sdB stars evolve away from the ZAEHB, their $\log g$ decreases (due to an increasing radius) for a while, and thus their periods would increase (because of a decreasing density). When core helium fusion ceases, the star goes through a period of contraction. During this time, $\log g$ is increasing as the star draws its

energy from gravitational contraction. Once sdBV stars are burning helium in a shell rather than the core, they quickly evolve to larger radius, which makes the periods longer.

Overall, we expect the pulsation period (for any given mode) to increase toward the top and right (increasing size) and decrease toward the bottom and left (decreasing size) of the HR diagram. Therefore, the first order of business it to organize the periods of the sdBV stars by T_{eff} and log g and see if any such trends exist. If sdB stars that lie in various regions of the HR diagram pulsate in different modes, no clear correlations will emerge.

Figures 7.1 and 7.2 show the pulsation periods observed for the 13 sdBV stars studied (indicated on the left) arranged by $\log g$ and T_{eff}. Also on the plot are the radial fundamental (blue arrows) and first overtone periods (green arrows) calculated from our evolutionary models. These model periods serve as a guide to indicate how p modes of the same n, ℓ, and m would change with T_{eff} and log g. As suspected from Equation 2.1, $\log g$ has the clearest effect on the pulsation periods, with the lowest gravity stars having the longest periods. Additionally, the longest pulsation period for each star roughly follows the fundamental radial mode (blue arrow) in Figure 7.2. At the bottom of each figure are all the periods, overlayed onto a single row. In neither figure are there any obvious groupings which might be used to identify pulsation modes. The properties of the individual stars vary much more than in the case of pulsating white dwarf stars (in the Clemens 1994b work).

7.2 Scaling with Surface Gravity and Radius

We now turn to scaling the pulsation periods with log g amongst the class members. From Equation 2.1, we know that radial and p mode periods scale as the inverse of the square root of the mean density. If we assume a constant mass (a good approximation as the mass only changes by ~5% across the HR diagram for sdB stars) we can recast Equation 2.1 to include g.

$$P \propto \frac{1}{\sqrt{G\bar{\rho}}} = \frac{1}{\sqrt{\frac{GM}{R^3}}} = \frac{1}{\sqrt{\frac{g}{R}}} \tag{7.1}$$

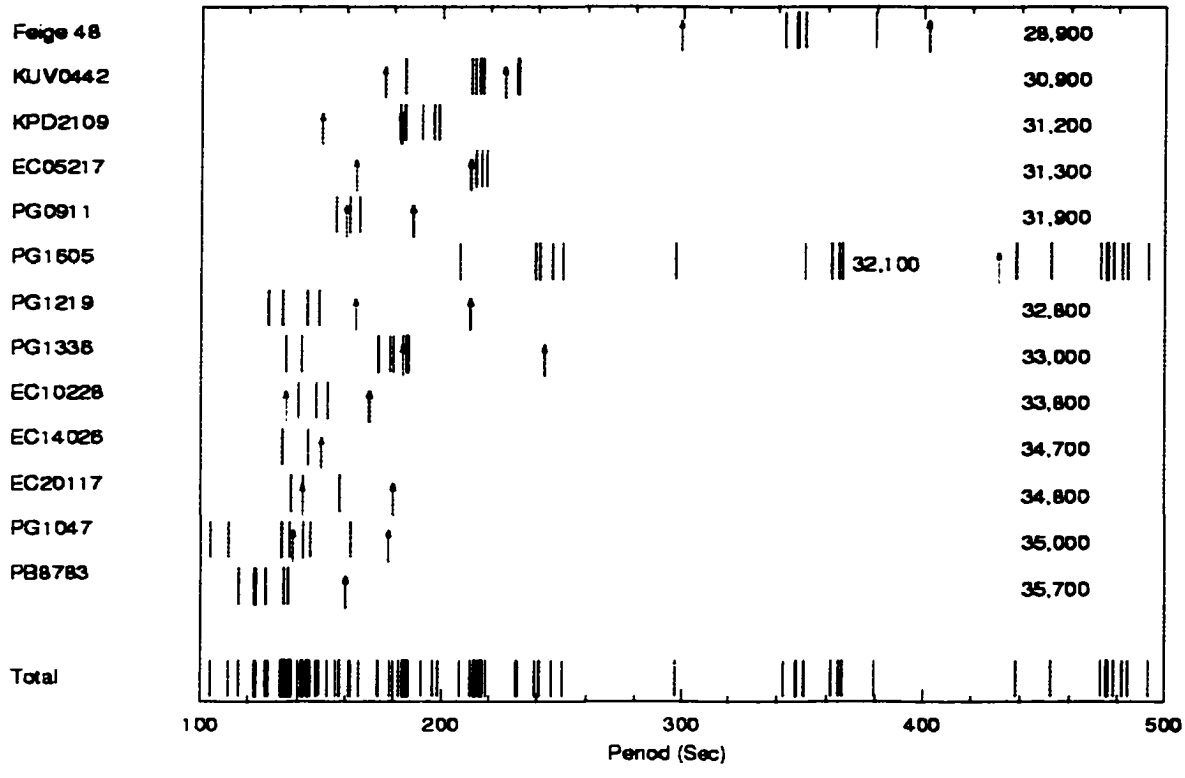

Figure 7.1 Periods observed in pulsating sdB stars, arranged by effective temperature (given in Kelvin at the right, but not to scale). Blue arrows indicate the theoretical fundamental radial period, while green arrows represent the first overtone.

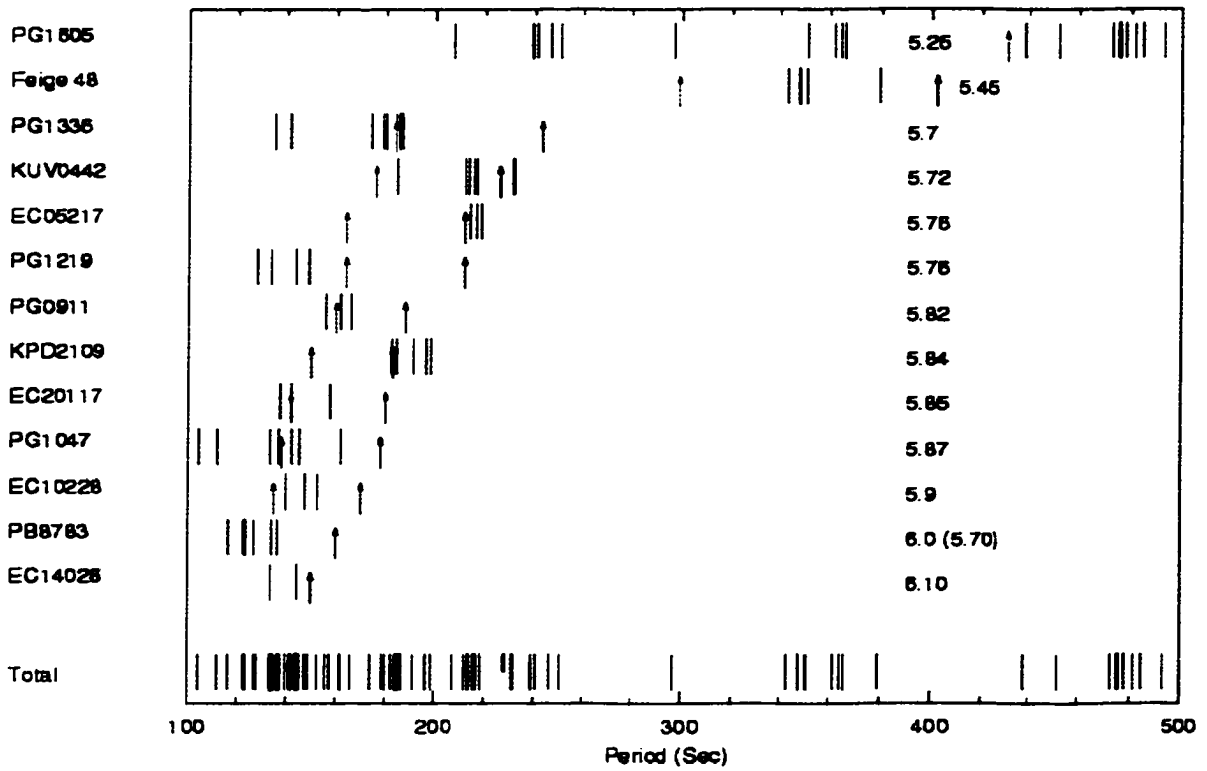

Figure 7.2 Same as Figure 7.1 except arranged by $\log g$ (given at the right). Blue arrows indicate the theoretical fundamental radial period, while green arrows are the first overtone.

Equation 7.1 is the form we desire, yet we have an extra variable, R. We can eliminate R as it is proportional to $1/\sqrt{g}$ (for fixed mass), which provides the equation we are after:

$$P \propto \frac{1}{g^{0.75}}. \tag{7.2}$$

We converted the periods to essentially dimensionless periods by multiplying by $g^{0.75}$. (We assumed that $\log g$=6.0 for PB 8783 as in O'Donoghue *et al* 1999.) The results are plotted in Figure 7.3. The arrow indicates how a 100 second period would change if the log g used to convert to dimensionless period were changed by 0.1. As such, it is representative of the error associated with each period in the figure.

If the pulsation modes in these stars were p-modes or radial modes of similar order, once corrected for differences in log g, the summed periods (bottom row) should fall into distinct

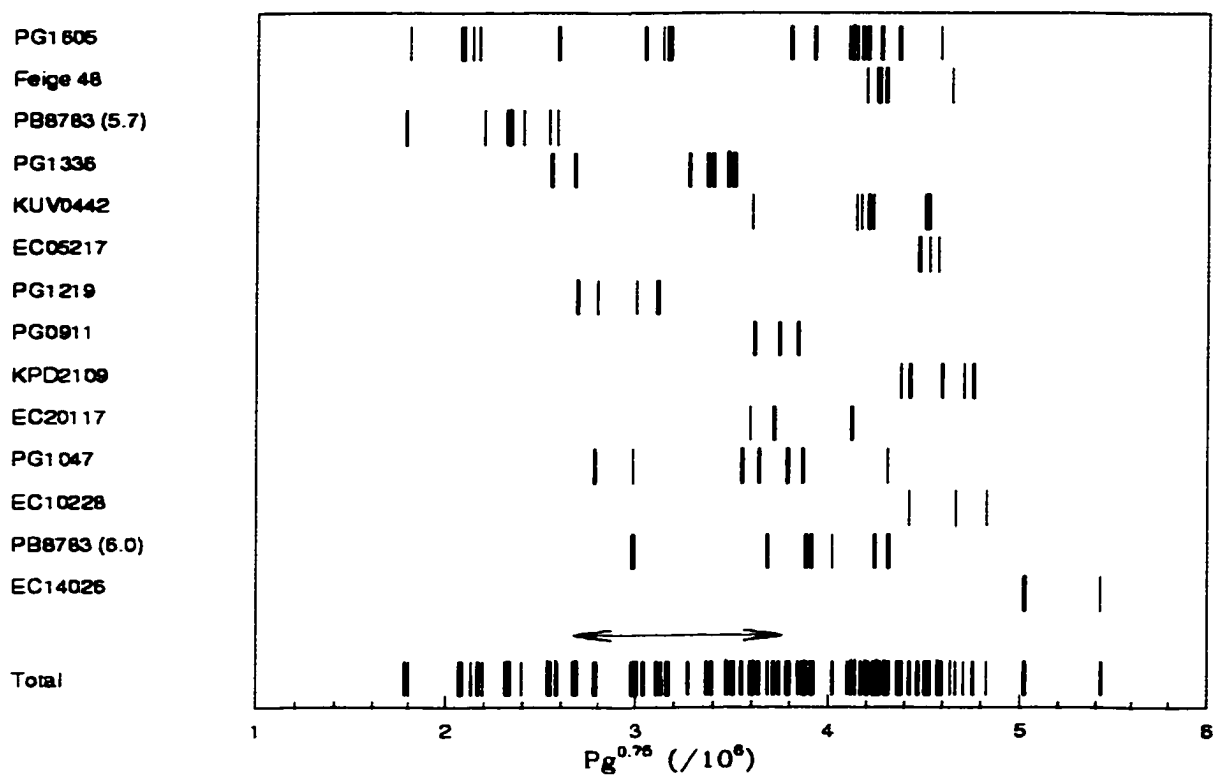

Figure 7.3 Same as Figure 7.2 except the periods have been converted to dimensionless periods by scaling as $g^{0.75}$. PB 8783 appears twice, with log g indicated in parentheses. The blue arrow indicates an error of ± 0.1 in $\log g$ for a 100 second period.

groupings. Such groupings might then be used to determine pulsation modes and how pulsations vary with age. This is not the case. The scatter is still as large as it was in Figures 7.2 (though the scales have changed). The reason may be from the large scatter the uncertainty in $\log g$ creates, as indicated by the blue line. Even if there were underlying groups, the scatter introduced by the uncertainty in $\log g$ would be enough wash it out. However, at this point the error associated with $\log g$ is based on atmospheric models and spectroscopy. To improve the results, the models need to improve. If spectroscopists can decrease the uncertainty in $\log g$, it would be worth it to rework this analysis.

It is certainly possible that an additional parameter, whether it be age, metallicity, or mass is needed to explain the variations within the group. This would not be surprising since, as indicated in Figure 1.2, both pulsators and non-pulsators inhabit the same region of the HR diagram. Additionally, it is possible that sdBV stars are structurally different from one another. More intriguing, the variations may result from differences in origin. Subdwarf B stars may be a more heterogeneous class of stars than we think (certainly more than the DAV stars used by Clemens, 1994b).

7.3 Conclusions

In §2.5.3, wee discussed how Clemens (1994b) inverted his ensemble analysis of DAV stars to determine properties (chiefly mass) of individual stars. In this chapter, we have attempted to do the same for sdB stars. At this point, looking for global similarities does not reveal any trends in the group properties of sdBV stars. What it does indicate is that this is more than a two parameter problem. Nearly every other type of variable star has a region in the HR diagram where only variable stars exist. That is not the case with sdB stars, so we should not be surprised that simply correcting for one of those parameters ($\log g$) did not simplify the pulsation periods. As noted in Chapter 5, we see *more* periods than our models can produce. These mysteries suggest that theorists may need to consider new classes of modes or unexpected structural details for the sdBV stars.

CHAPTER 8. NEW TOOLS FOR ASTEROSEISMOLOGY

In the last three chapters, we applied asteroseismological tools that have been successfully used in the past on other types of pulsating stars. The first two were used with some success while the last tool, *ensemble analysis* points out that effective temperature and log g alone do not determine the pulsation periods of sdBV stars. Additional parameters are needed.

In this chapter we will depart from standard tools and develop new tools which may be useful for identifying modes in close binaries. With few exceptions (usually dealing with cataclysmic variables) pulsation analysis has been performed on single stars, or stars in long period binaries where the companion has no effect on the pulsations. We will now examine what happens when a companion directly influences the observed pulsations.

As alluded to in previous chapters, our analysis will center on PG 1336. PG 1336 is an sdBV star with an ~M5 companion in a 2.4 hour eclipsing binary (Kilkenny *et al.*, 1998). During primary eclipse, the companion covers about half of the pulsator. Since pulsations manifest themselves as alternating hot and cool regions on the star's surface, changes in the visible surface area during eclipse should change the observed pulsation amplitudes in a predictable way.

8.1 Using Eclipses to Identify Pulsation Modes

8.1.1 Eclipse modeling

To determine what effect the eclipse will have on the pulsation modes of PG 1336, we simulated the binary system using orbital parameters determined by Kilkenny et al (1998). We ignored limb darkening (a small effect in sdB stars), assumed the secondary contributes no light to the system (very reasonable since $L \propto T^4$ and the companion is an order of magnitude

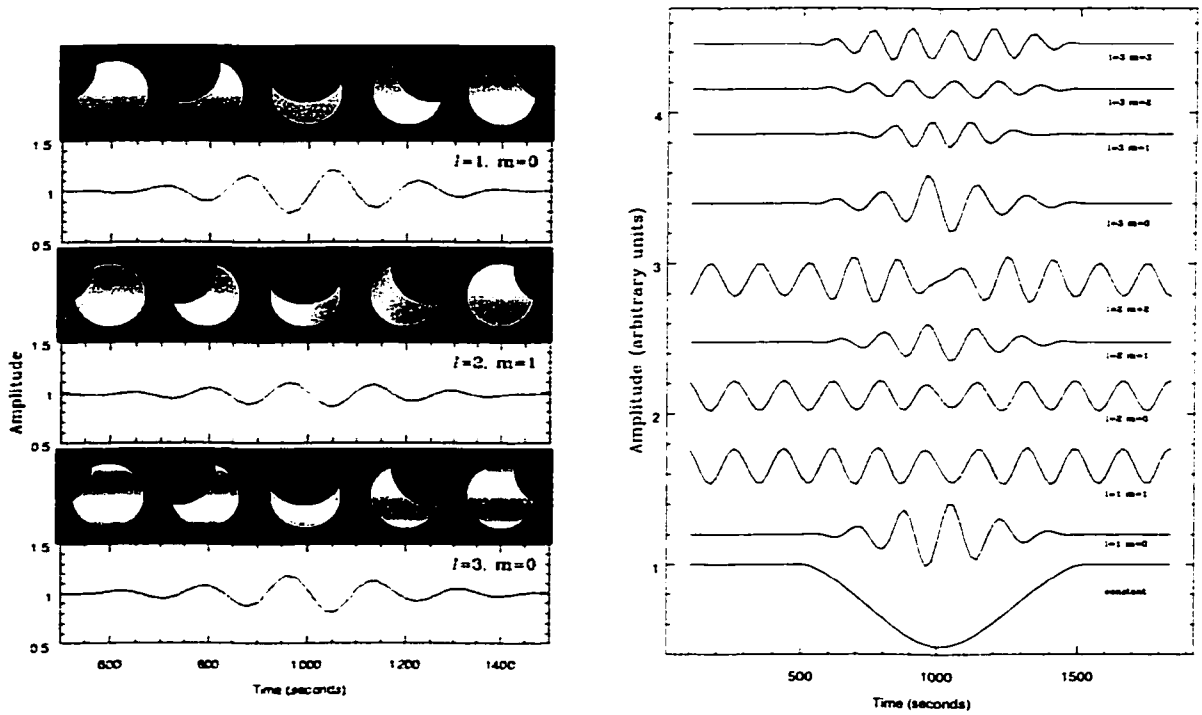

Figure 8.1 Left: Sample model images (at 200 second intervals) and light curves for simulations of PG 1336. Right: Light curves from simulations of non-radial pulsations. The lightcurves have been corrected by the constant curve at bottom.

cooler), and used a single pulsation period of 175 seconds (in the range of periods detected for PG 1336). By simulating the eclipse for one frequency, we can determine how the eclipse will affect individual modes of given ℓ and m. Representative simulations are shown in Figure 8.1 with results listed in Table 8.1.

As hoped, they indicate that the visibility of several modes will vary during eclipse. Ideally, any ℓ=1, $m = \pm 1$ modes observed outside of eclipse would have a corresponding ℓ=1, m=0 mode seen only in eclipse, and any ℓ=2 pulsations would have $m = \pm 1$ components showing

Table 8.1 Pulsation modes detected in simulations.

Visible *only* outside of eclipse:	$\ell = 2$, $m = \pm 2$
Visible *only* during eclipse:	$\ell = 1$, $m = 0$; $\ell = 2$, $m = \pm 1$; all $\ell = 3$ modes.
Always visible	$\ell = 1$, $m = \pm 1$; $\ell = 2$, $m = 0$; all radial modes

up only in eclipse. Thus by comparing observed pulsations during primary eclipse to those observed out of eclipse (OoE), we should be able to identify at least some pulsation modes.

8.1.2 Eclipse Data

Figure 8.2 shows the lightcurve through primary eclipse and the results of extracting the "DC component". We coadded all data during primary eclipse to smooth out pulsational variation and determine an average eclipse contour. We then used this average eclipse profile to remove the slowly changing background of individual eclipses. Variations in seeing and extinction at different sites were removed by dividing out a low order polynomial. We trimmed the data to the central 800 seconds of the ~900 second eclipse to maximize the effect the eclipse will have on observed pulsation amplitudes.

With only 800 seconds of data every 2.4 hours, each real oscillation frequency creates a large and complex assortment of alias peaks in the Fourier transform. As can be seen in Figure 8.3, the numerous aliases complicate finding the real modes in the temporal spectrum.

Even though adjacent alias peaks have nearly the same amplitude as the real peak (as determined from the data window), the window pattern is fairly clean. That is, prewhitening does a good job of removing the alias peaks. Even so, we would not presume to detect the correct periods (rather than aliases) without some additional evidence. We could use the OoE data as an initial template to try to identify true frequencies as many modes should be present at all phases (see Table 8.1). However, since data reduction is somewhat subjective, using OoE periods might bias the eclipse results, so we did not using any preconceptions about which peaks should be the "real" ones.

Detecting and fitting frequencies for the Xcov 21 eclipse data was much simpler than for the Xcov 17 data (which we will not reproduce here because of the much better quality of the Xcov 21 data). We proceeded essentially as outlined in §2.1: we *presumed* that the highest peak found in the FT was real and prewhitened by it. Next we simultaneously LSQ fit the next highest peak along with our first peak and prewhitened the lightcurve by two periods. Then we simultaneously LSQ fit the three highest peak and so on. As a check, we completely

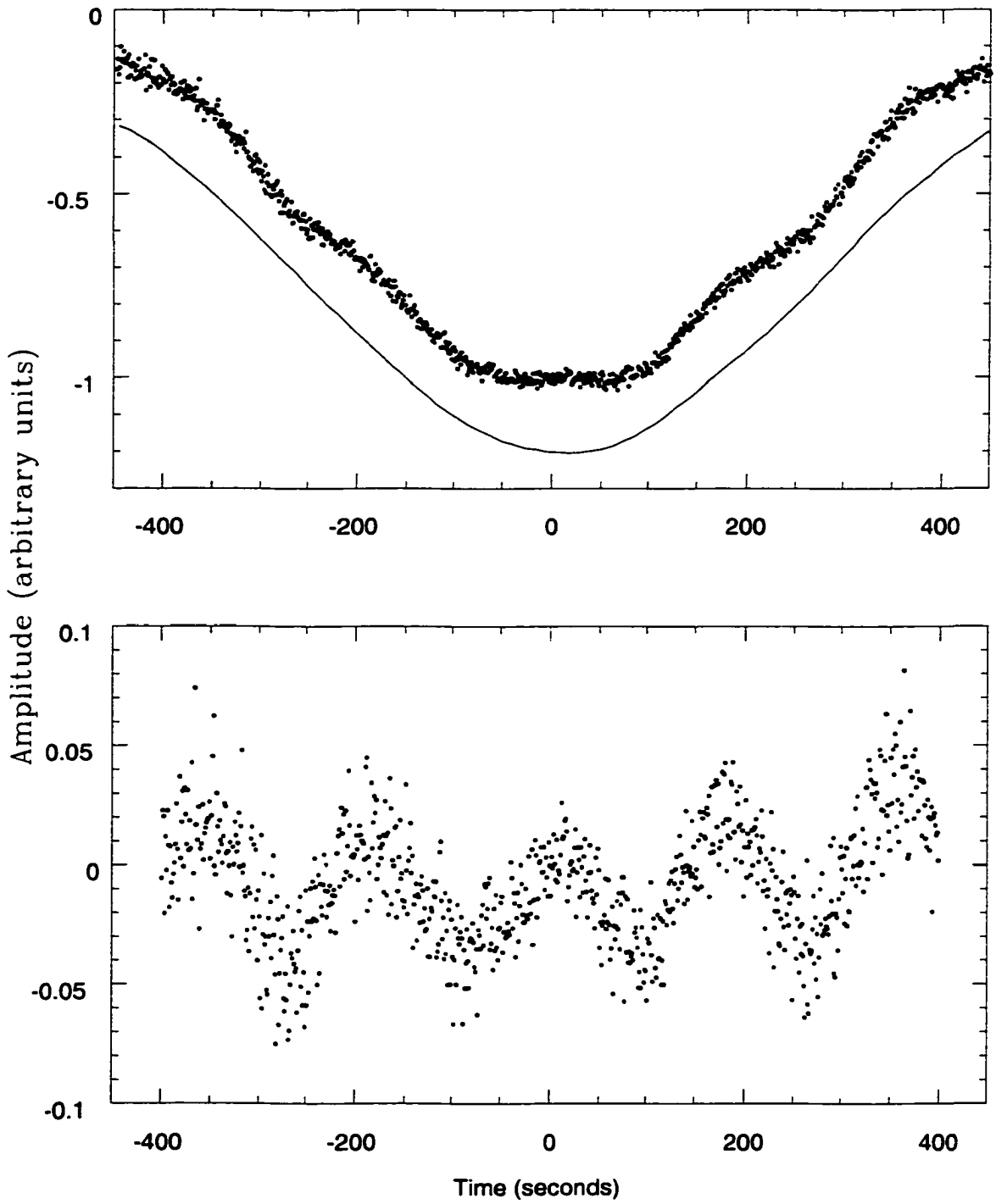

Figure 8.2 Top: A sample extracted eclipse data with correcting contour (line) offset by -0.2. Bottom: Corrected eclipse showing obvious pulsations.

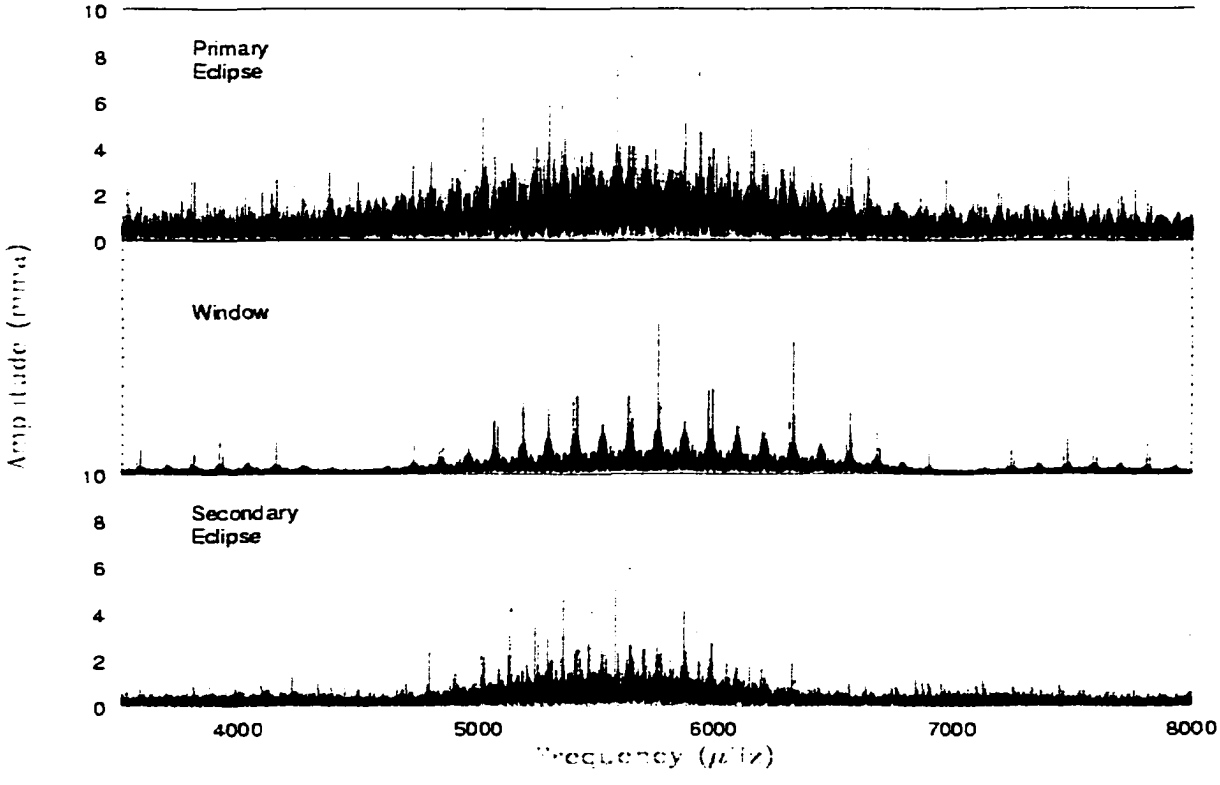

Figure 8.3 Top: Temporal spectrum of primary eclipse for Xcov 21 data. Middle: Data window. Bottom: Temporal spectrum of secondary eclipse for Xcov 21 data.

Table 8.2 Period List for PG 1336 from Xcov 21 for primary eclipse data. (Formal LSQ errors in parenthesis.)

Mode	Period (sec)	Frequency (μHz)	Amplitude (mmag)	Splittings	$\Delta f_i - nf_{orb}$ (μHz)
$e1$	145.35056(57)	6879.919(27)	1.89(13)	$g10\text{-}2f_{orb}$	0.00
$e2$	150.06631(50)	6663.721(22)	2.26(13)	$g10\text{-}4f_{orb} + f_d$	1.42
$e3$	150.83626(39)	6629.706(17)	3.42(15)	$g9\text{+}4f_{orb}$	7.49
$e4$	163.81136(85)	6104.583(32)	1.62(13)	$f8\text{+}3f_{orb}$	3.53
$f8$	173.69319(21)	5757.278(7)	8.72(15)		
$e5$	176.26144(78)	5673.390(25)	2.04(13)	$f5\text{+}2f_{orb}$	1.92
$f7$	179.03320(22)	5585.556(7)	8.38(15)		
$e6$	180.18542(66)	5549.838(21)	2.51(13)	$f4\text{+}f_{orb}$	-0.16
$e7$	181.22067(44)	5518.134(13)	4.29(15)	$g5\text{+}f_{orb}$	4.31
$e8$	186.39969(71)	5364.816(21)	2.57(14)	$g7\text{-}2f_{orb}$	-4.52
$e9$	187.48520(55)	5333.754(16)	3.71(15)	$f5\text{-}f_{orb}$, $g3\text{+}f_{orb}$	4.05, 0.12
$e10$	198.07106(76)	5048.693(19)	2.64(13)	$f2\text{-}3f_{orb}$, $g6\text{-}4f_{orb}$	0.46, -0.15
$e11$	199.30814(112)	5017.356(28)	1.85(13)	$f7\text{-}5f_{orb}$	4.66
$e12$	208.48621(76)	4796.480(17)	3.38(16)	$f1\text{-}5f_{orb}$	0.06
$e13$	228.79250(115)	4370.773(22)	2.63(15)		

Notes: f_{orb}=114.59μHz, f_d=11.57μHz

reduced the data several times, choosing peaks other than the highest at various stages. This provides a qualitative check in that if the wrong peak is chosen, prewhitening may leave behind many more aliases than if the proper peak was chosen. As it turns out, choosing the highest peak each time produced the cleanest prewhitened spectrum. These frequencies are listed in Table 8.2.

As mentioned in §8.1.1, we expect to observe several modes in both the OoE and primary eclipse data, as well as new, rotationally split modes in the primary eclipse data only. This was not the case (see Figure 8.9). Of the 15 modes detected during primary eclipse, only 2 were observed in the OoE data (the 2 with the largest amplitudes).

One possible explanation is that the primary eclipse data are too contaminated with aliases to be useful. To test this, we reduced and analyzed data from the secondary eclipse (shown in Figure 8.3) in the same fashion as from the primary eclipse. Sampling times (and therefore the window function) are parallel to the primary eclipse data, so the alias problem should be nearly identical. We readily detected and prewhitened 12 peaks in the temporal spectrum in

the same manner described for the primary eclipse data. Eleven of the twelve peaks coincided exactly (to within the errors) to those detected in the OoE data. This gives us confidence that our reductions revealed real differences between the pulsations during primary eclipse and OoE.

8.2 Tipped pulsation axis

While prewhitening was a major tool in the last section, we also need to consider pulsation phase. If the pulsation axis aligns with the rotation (and orbital) axis, phase will be preserved through the orbit. However, looking at the phase of the LSQ solutions for some modes showed that this was not the case. During Xcov21, headquarters staff first noticed this: some modes showed "phase flips" around the orbit. This could produce complications in the FT similar to what we see in Figure 8.3. The origin of such phase changes could be in orbital modulation of the orientation of the pulsation axis. This is similar to the rapidly oscillating Ap (roAp) stars, in which the pulsations are aligned with the magnetic field (which in turn is inclined to the rotation axis) (Baldry, Kurtz, and Bedding, 1998). For roAp stars, the magnetic force is stronger than the Coriolis force near the surface, forcing the pulsations into symmetry about the magnetic axis. This produces direct observational consequences that allow us to probe the magnetic field in these stars and has stimulated numerous theoretical challenges (Kurtz *et al.* 2001, Cunha 2001). For PG 1336, the tidal force could provide a larger perturbative affect than the Coriolis force, causing the pulsations to align with an axis that points to the secondary star.

To determine the effect of such an alignment, we created simulated light curves where the pulsation axis is tipped by 90 degrees (the inclination of the actual binary is 81 degrees) and always points toward the companion (eclipses were ignored). Our simulated light curves for various values of ℓ and m are shown in Figure 8.4 and the corresponding temporal spectra are shown in Figure 8.5. Pulsation modes are indicated on the left of each plot (as in $f\ell m$). For the light curves, phases (where a shift of 0.5 = 180°) are green lines, with scales on the right of the plot, and blue and magenta lines indicate orbital phases (PE=primary eclipse,

SE=secondary eclipse, T and A=quadrature when the star is moving toward and away from the observer, respectively). For the temporal spectra, the red line indicates the input frequency (corresponding to a pulsation period of 175 seconds), the blue lines are $1 \cdot f_{orb}$ away from the input signal and the green lines are $2 \cdot f_{orb}$ away from the input signal. As indicated in Figure 8.4, *every* non-radial mode undergoes at least two 180° shifts in phase during each orbital cycle. The position and frequency of the phase shifts determines where the peaks are located in the temporal spectra.

8.2.1 Determining the Mode Structure in Xcov Data- Simulations

Now that we know how data should look under such conditions, the next step is to reduce the real data in such a way to determine if this scenario matches what is going on in PG 1336. The method we will use is to break up the data by orbital phase. Figure 8.6 depicts how we divide the light curve into octants for analysis. Octants 1 and 5 are the primary and secondary eclipses, respectively, 2 to 4 are the octants where the primary is traveling toward us, and 6 to 8 are the octants where the primary is traveling away from us. The companion is not depicted in the figure. The pulsation represents a tipped ℓ=1, $m = \pm 1$ pulsation, frozen in phase, at four points in the orbit.

Using the simulation, we can reduce parts of the orbit where pulsations of a given mode will have a given phase. These are listed in Table 8.3. The table also gives the FT signature for these modes in the temporal spectrum of the combined data set. If the data are separated into data sets combined such that they either have 0° or 180° phase, then only the central (real) peak should appear in the temporal spectrum.

We combined our simulated data into sections of like phase according to Table 8.3 and then calculated new temporal spectra. The results are shown in Figure 8.7. As expected, the central (real) peak is now the largest. However, with less data, and orbital frequency gaps, the aliases are considerably worse than in our complete, non-divided data set.

Since we have two "independent" data sets that should differ only in orbital phase, we determined the phase of pulsation, using standard techniques outlined in Chapter 6, for the

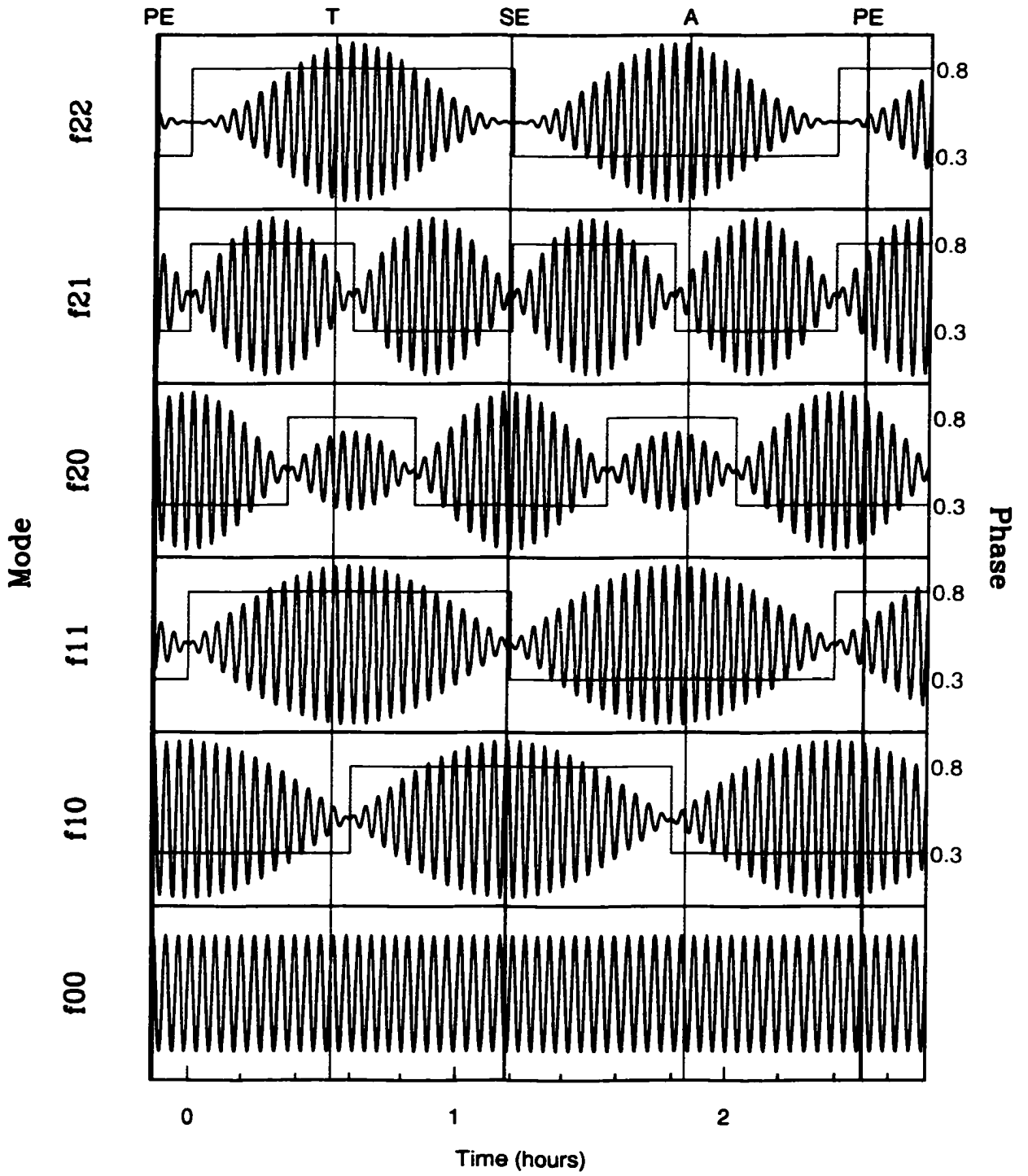

Figure 8.4 Light curves for simulated single mode (given as $f\ell m$) pulsation data with the pulsation axis tipped 90 degrees to the rotation axis and continuously pointing at the secondary star.

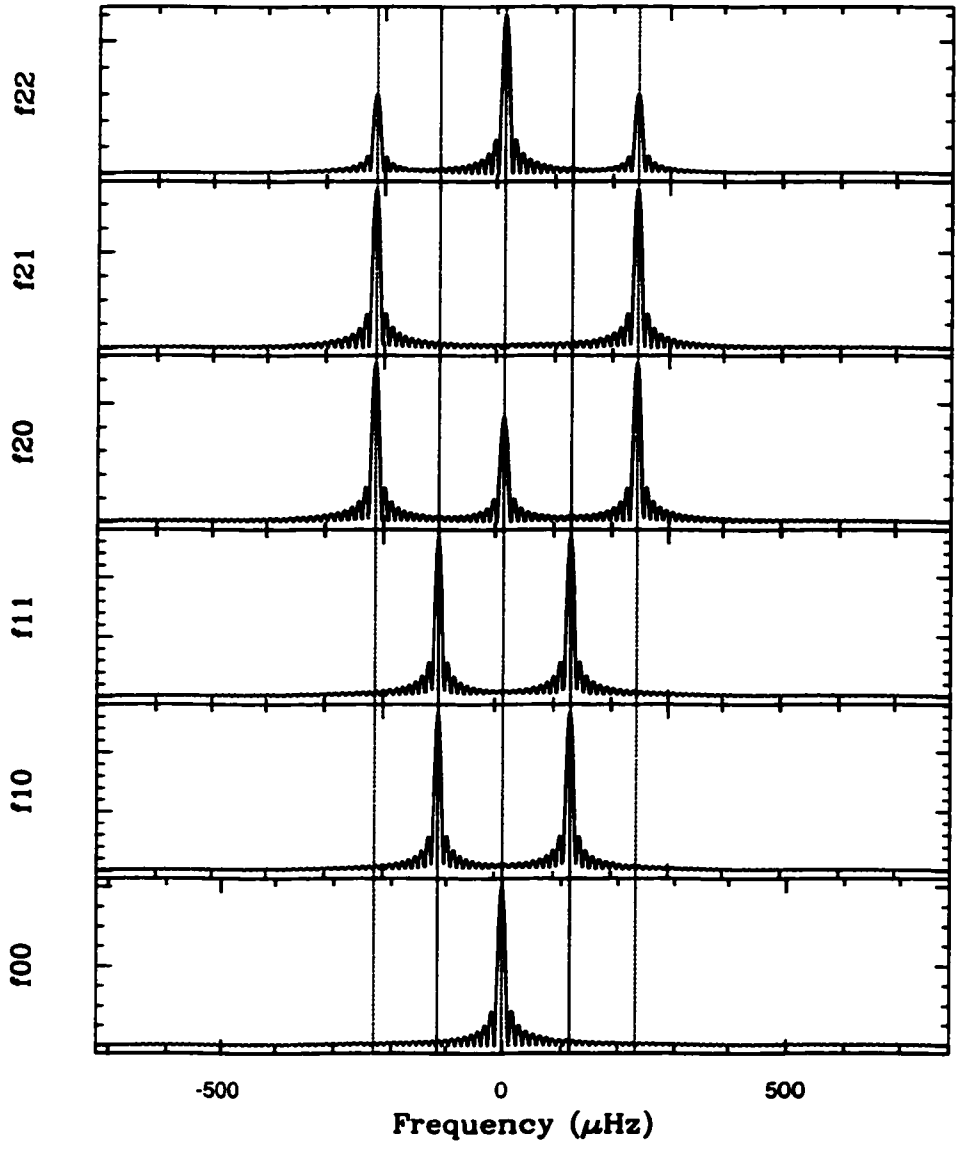

Figure 8.5 Temporal spectra for simulated light curves shown in Figure 8.4. Red line indicates the frequency of the input signal (the $f00$ mode is the same as the input signal), blue lines indicate frequencies $1/f_{orb}$ away from the input signal, and green lines indicate frequencies $2/f_{orb}$ away from the input signal.

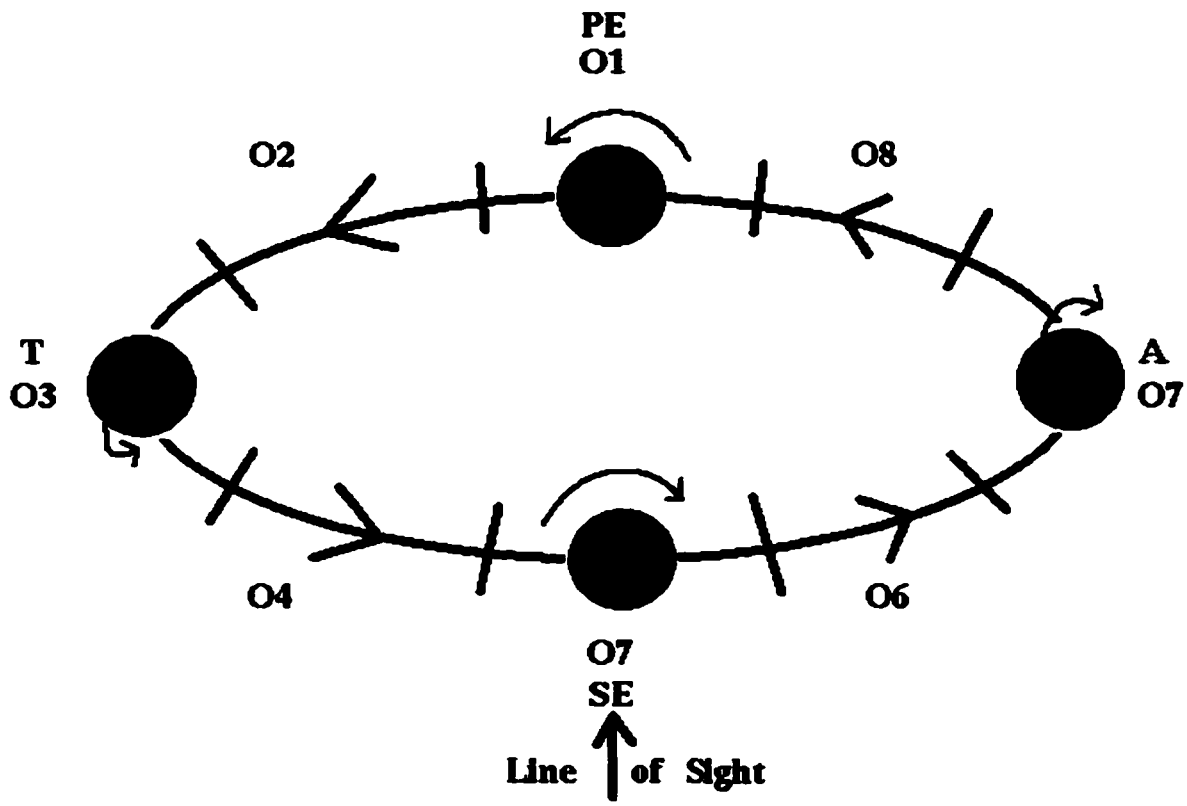

Figure 8.6 Schematic showing the octants used in the analysis. Octant 1 corresponds to primary eclipse and Octant 5 to secondary eclipse. Arrows show the direction of orbital motion and the motion of the ℓ=1, m=±1 pulsation pattern about the pulsation axis.

Table 8.3 Phases and FT signatures for individual pulsation modes in the case of a tipped pulsation axis.

Mode	Phase A	Phase B	Temporal Spectrum	
$f\ell m$	0°	180°	No. of Peaks	Separation
$f10$	O4, O5, O6	O8, O1, O2	2	$2f_{orb}$
$f11$	O2, O3, O4	O6, O7, O8	2	$2f_{orb}$
$f20$	O1, O5,	O3, O7	3	$2f_{orb}$
$f21$	O2, O6	O4, O8	2	$4f_{orb}$
$f22$	O2, O3, O4	O6, O7, O8	3	$2f_{orb}$

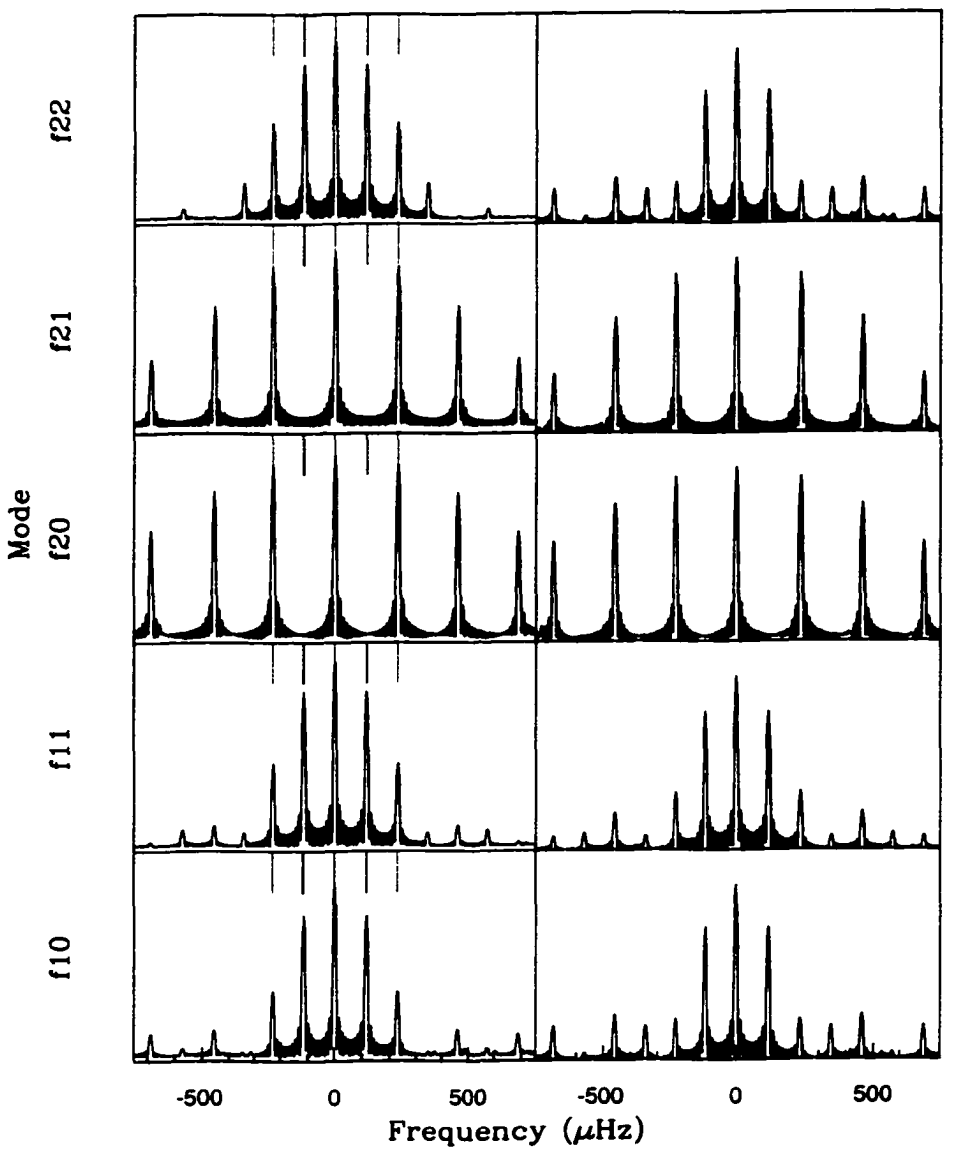

Figure 8.7 Temporal spectra of simulated single mode variations (indicated as $f\ell m$) for 'Phase A' data (Phase B data looks the same). Right panel are the spectral windows for each mode.

Table 8.4 Phases for pulsations in simulated 'A' and 'B' data sets. Phase goes from 0 to 1.

Mode $f\ell m$	Phase A	Phase B
$f10$	0.78	0.29
$f11$	0.29	0.78
$f20$	0.29	0.78
$f21$	0.29	0.78
$f22$	0.29	0.29

'Phase A' and 'Phase B' data sets. Our results are given in Table 8.4 and provide another piece of evidence when looking for tipped modes. All the modes, except for $f22$ (which will require further study to understand), should show phase changes during each orbital cycle.

Now we have three ways of exploring effects of a tipped axis:

- Radial modes will not be effected by a tipped pulsation axis.
- ℓ=1, m=0 ($f10$) and ℓ=1, $m = \pm 1$ ($f11$) modes will each appear in the temporal spectrum of the total data set as two modes separated by $2f_{orb}$, with a missing central peak. When divided into two appropriate phase groups, the central peak will appear, and the phases between the groups will differ by 180°.
- ℓ=2, m=0 ($f20$) modes will appear as triplets with peaks separated by $2f_{orb}$ in the temporal spectrum of the total data set with the central peak (probably) having the lowest amplitude. When divided into appropriate phase groups, the central peak will become the highest amplitude peak and the phases between the groups will differ by 180°.
- ℓ=2, $m = \pm 1$ ($f21$) modes will appear as two modes separated by $4f_{orb}$ in the combined data set. When separated into appropriate phase groups, the central peak appears and the phases between the two groups will differ by 180°.
- ℓ=2, $m = \pm 2$ ($f22$) modes will appear as triplets with peaks separated by $2f_{orb}$ in the combined data set. When separated into appropriate phase groups, $f22$ modes appear as

single peaks with a normal window pattern (that is aliases separated by nf_{orb}). However, the phase does not change, making this mode difficult to detect (and still a mystery to understand).

8.2.2 Xcov 21 Data

The data obtained during Xcov 21 will be the first used to determine the orientation of the pulsation axis. However, these data were obtained in April of this year, and will require substantial time to complete an in-depth analysis. In such a large data set, there is some redundancy in data and several data combinations need to be tested to determine which combination of runs is best for this analysis. However, preliminary results can test our assumptions. We separated our lightcurve data into the simplest bins possible; those appropriate for detecting $f11$ modes. This combination breaks up the data into two sets, each with the most continuous data without incorporating any eclipse data (which has its own complexities) in Table 8.3. The Phase A data set corresponds to when the primary is moving toward us (octants 2 to 4) and the Phase B data set corresponds to when the primary is moving away from us (octants 6 to 8). These two data sets were subsequently reduced in the usual manner, with the top twelve modes detected. Of these twelve modes, eleven were common between the two data sets and are listed in Table 8.5. Phases were calculated for each period in both data sets and are listed in columns 3 and 4 of Table 8.5.

Two new peaks at 5254.793 and 5483.940μHz (designated $\nu1$ and $\nu2$ respectively),in each appear that are not seen in the combined data set. Each shows 180° phase difference between the two data sets. Both modes show up when the data are divided, and the phase changes appropriately. The last line of evidence will be to determine if there corresponding peaks in the combined data set (the OoE data in this case) split by $1f_{orb}$.

In the Xcov 21 temporal spectrum (Figure 4.13) there are two, comparatively high amplitude peaks ($f1$ and $g7$ in Table 5.6) separated by $2f_{orb}$; $\nu2$ falls exactly where it should, halfway between $f1$ and $g7$. This provides strong evidence that $\nu2$ is a real $f11$ mode of a tipped pulsation axis with $f1$ and $g7$ as its sidebands.

Table 8.5 Phases (formal LSQ errors in parentheses) for pulsations in Phase A and B data sets appropriate for detecting $f11$ modes in Table 8.3. Designations are as in Table 4.11 with new modes designated by νn.

Mode	Frequency (μHz)	Amplitude (mma)	Phase A	Phase B	ΔPhase
$\nu 1$	5254.793*	1.94	0.922(9)	0.441(8)	0.481(12)
$f3$	5433.238	1.47	0.483(10)	0.428(9)	0.055(13)
$f4$	5435.410	1.46	0.229(11)	0.239(11)	0.010(15)
$f5$	5444.296	1.92	0.075(8)	0.078(8)	0.003(11)
$\nu 2$	5483.940*	4.97	0.325(3)	0.816(4)	0.491(5)
$f7$	5585.651	3.65	0.946(4)	0.951(4)	0.005(6)
$f8$	5757.288	7.18	0.196(2)	0.187(2)	0.009(3)
$f9$	5760.764	1.62	0.731(10)	0.682(9)	0.049(13)
$f11$	7071.182	0.68	0.530(15)	0.505(19)	0.025(24)
$g10$	7109.090	1.16	0.705(18)	0.670(19)	0.035(26)
$g13$	8353.912	0.70	0.704(18)	0.669(16)	0.035(24)
$g14$	9220.048	0.72	0.445(16)	0.488(19)	0.033(25)

The case is not nearly as strong for $\nu 1$. As it turns out, $\nu 1$ is precisely $2f_{orb}$ away from $\nu 2$, and thus they would share $f1$ as a common alias. However, $\nu 2$ has a significantly lower amplitude, so its aliases are less likely to be detected in the combined data set. Also, it is entirely possible that $\nu 1$ is simply an alias of $\nu 2$

Once the Xcov 21 data is fully reduced, future plans include a similar analysis for other octant groupings that optimize detection of other modes given by Table 8.3. However, all other modes do not have as contiguous data sets as the ℓ=1, $m = \pm 1$ modes, or need to include octants during eclipses. This adds an additional set of complexity to the lightcurves. As such, our preliminary data set is not beneficial for such analysis.

8.3 Tipped eclipses

Since we have found *some* evidence for a tipped pulsation axis, it becomes appropriate to determine if the primary eclipse is still a good indicator of pulsation mode. We modified our simulations from §8.1.1 to have the pulsation axis pointing toward the companion as it eclipses the primary. Again, we produced light curves for individual pulsation modes, which are shown

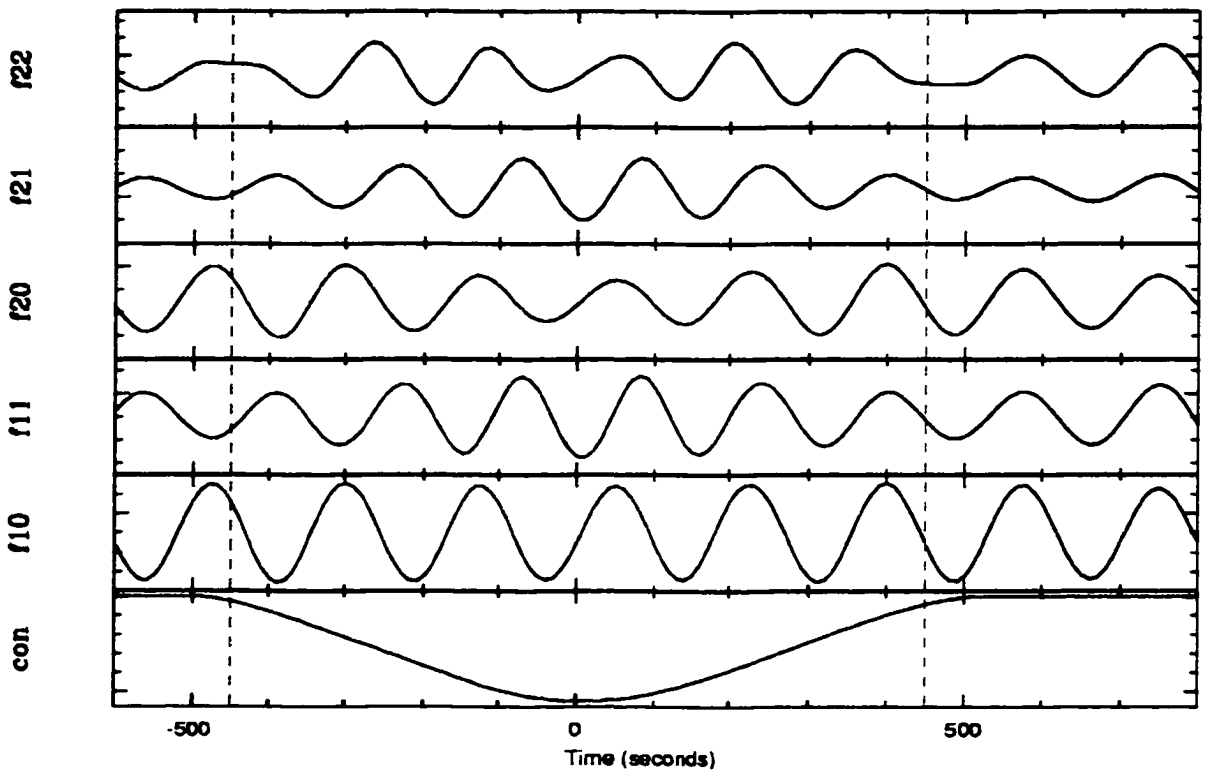

Figure 8.8 Simulated light curves through eclipse with a 90° tipped pulsation axis. The bottom panel has been divided out of the other lightcurves.

in Figure 8.8.

As the figure shows, only the $f22$ mode has any discernible amplitude (and phase) change during eclipse. In fact, pulsations that would normally have a change in phase during primary eclipse (all $m \neq 0$ modes) do not. As such, the changing geometry offered by primary eclipse is no longer useful for mode identifications.

8.4 Results

Figure 8.9 shows, schematically, pulsations detected with various reductions of the Xcov 21 data for PG 1336 from the Xcov 21 WET run. More than 20 individual pulsations are detected in the combined data set, most of which are detected in other data sets restricted by phase.

The primary eclipse temporal spectrum is the most unusual, with only 2 modes detected in other temporal spectra. Many of the remaining modes are orbital separations away from modes detected in the OoE spectrum, yet are likely not artifacts of the data, but real pulsations. The temporal spectra at eclipse and quadrature provide good indications that the pulsation axis of PG 1336 is not aligned with the rotation axis, but rather (at least somewhat) with the tidal force from the companion for some modes.

The tools used in our ongoing analysis of PG 1336 will be needed for other stars. A sizable fraction of known sdBV stars are in binaries (Green, Liebert, & Saffer, 2001), so it is probable that other pulsators also have pulsation axes which align with the tidal force of their companions. An important example is KPD 1930. It is an sdBV star in a 2.1 hour binary with a $0.9M_{\odot}$ white dwarf companion (Maxted *et al.*, 2000; Billéres *et al.*, 2000). It also shows ellipsoidal light variations, showing that the sdB component experiences severe tidal distortions. With a more massive companion and shorter orbital period than PG 1336, KPD 1930 should show more extreme tidal effects on its pulsations. This Chapter provides the tools to investigate such possibilities.

Highlights of this chapter:

- Determined how pulsations vary when the partial eclipse alters viewing geometry, assuming the pulsation axis is aligned with the rotation axis.
- Indicated that partial eclipses can be an excellent way to identify pulsation modes if the pulsation axis is aligned with the rotation axis. Explained characteristics to look for to provide unique mode identifications for eclipsing binaries.
- Described a method for correcting light curves for eclipses, making data during eclipses useful for asteroseismological studies.
- Examined effects of aligning the pulsation axis with the tidal forces.
- Determined 3 unique signatures that can used to determine if a pulsation axis is pointing along the tidal axis and showed how to use these signatures to identify uniquely pulsation modes.

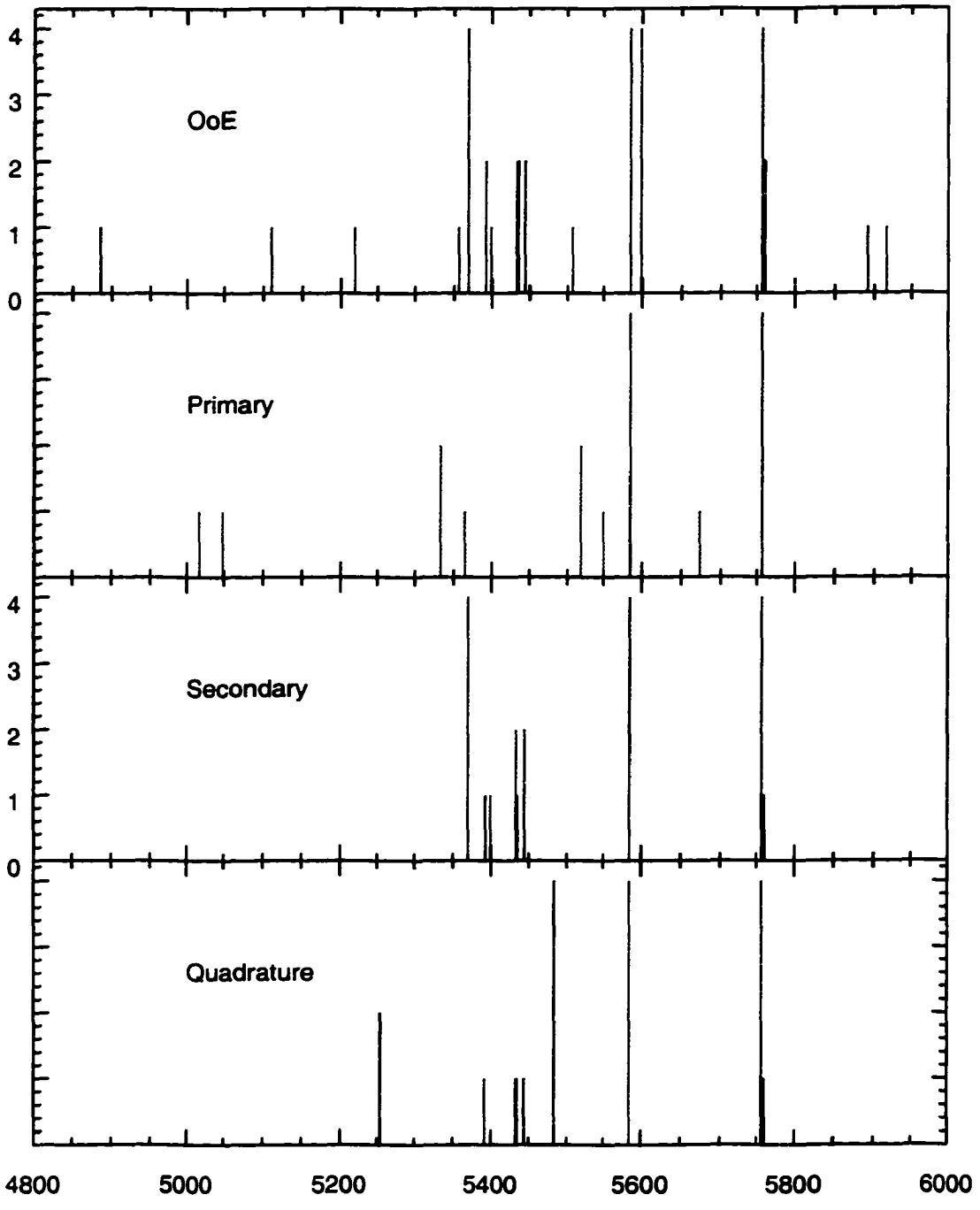

Figure 8.9 Pulsations detected in various data sets. Peaks binned in amplitude for clarity.

- Described how to reduce data for close binaries such that pulsation modes may be identified.
- Determined how pulsations vary through partial eclipse if the pulsation axis is aligned with the tidal force.
- Applied (preliminary and limited) analysis to PG 1336 to search for signatures of a tipped pulsation axis.
- Found one pulsation mode in PG 1336 that provides strong evidence for a pulsation axis that points toward its companion. We also found a second mode that follows two of three characteristics, but is not nearly as secure.
- Should further reductions and tests confirm our analysis, we will have uniquely identified a pulsation mode in PG 1336 (and eliminated two additional peaks from the temporal spectrum) which may be used to constrain pulsation models.

CHAPTER 9. CONCLUSIONS

This work was begun with the goal determining the general internal structure of sdB stars using the tools of asteroseismology. Of course, if this problem were simple, it would have been solved soon after pulsating sdB stars were discovered. A series of discovery papers (Kilkenny *et al.* 1997a and 1997b; Koen *et al.*, 1997, 1998a, and 1998b; O'Donoghue *et al*, 1998; and references therein) quickly indicated that sdBV stars show a wide range of pulsation properties.

As my thesis work progressed, it became obvious that there would be no "magic bullet" that would lay out the structure of sdB stars. However, this work has taken some large steps towards a more complete understanding of sdBV stars and suggests ways for further investigation. In this concluding chapter, we review the results.

9.1 Results from this Work

9.1.1 Observations

The first step in the process of applying asteroseismology to sdBV stars is to resolve the temporal spectra of the variations. Seldom does discovery data accomplish that. Therefore, one primary mission of this thesis was to observe sdBV stars with particular emphasis on trying to obtain sufficient data to resolve the temporal spectrum. To this end, I have spent hundreds of hours observing sdBV stars. Included in this thesis are results from over 125 hours of observations on PG 1605, nearly 300 hours of data on Feige 48, and over 650 hours of data on PG 1336. Data was obtained from two site runs for PG 1605 as well as multisite data for Feige 48 and two Whole Earth Telescope runs for PG 1336. Of course I was not working alone. During this time, there were also multisite campaigns on PG 1605 (Kilkenny *et al.*, 1999) and PB 8783 (O'Donoghue *et al.*, 1998).

In this thesis, we concentrated on four stars with resolved temporal spectra. For PB 8783, that data were contributed by Darragh O'Donoghue from a multisite campaign. For PG 1605, we acquired two seasons of follow up data to accompany multisite data contributed by Dave Kilkenny. For Feige 48, we obtained data over two seasons, which when combined with Chris Koen's (1998b) discovery data, totaled more than three years of coverage. PG 1336 was the target of two Whole Earth Telescope campaigns, two years apart. Both runs resolved the temporal spectrum, with the second campaign optimized to study pulsations through the primary eclipse.

9.1.2 Applying the Tools of Asteroseismology

As with every new discovery (in this case a new class of variable stars), the first thing to do is to apply what we already know. In this case we started with previously developed tools of asteroseismology (outlined in Chapter 2). In most cases, the old tools will need to be supplemented (or replaced entirely) with new ways of analyzing the data in order to make progress in mining the sdBV stars. Here we review results of our analysis of the four stars of this work.

PB 8783

For PB 8783, our *pattern matching* analysis revealed that:

- The data show evidence of a rotationally split triplet with a frequency spacing of $\sim 0.94\mu$Hz.
- The data include a pair of modes separated by $\sim 1.9\mu$Hz, or twice the $\sim 0.94\mu$Hz, which could also be a triplet, with an unobserved central peak.
- PB 8783 is a low amplitude pulsator. Before any definitive mode identifications can be made, better quality data will have to be obtained.

We analyzed the temporal stability of modes in PB 8783 and determined that:

- Though PB 8783 has low amplitude variability, two modes had stable amplitudes and phases during the multisite campaign.
- Our $O-C$ is consistent with no phase change over the course of the multisite campaign and rules out an orbital period for the binary between 1.5 and 12 days.

Since PB 8783 is a known binary, we looked for effects of the binary (as developed in Chapter 3) and found that:

- The temporal spectrum of PB 8783 does not show alias peaks which would be expected for a binary period between 1 (for $i \leq 10°$) and 12 days (with $i \leq 80°$).

PG 1605

For PG 1605, our *pattern matching* analysis confirmed that:

- Kawaler's (1999) model is a good fit to the five highest amplitude modes.
- Kawaler's (1999) model requires a large rotation velocity (130 $km \cdot s^{-1}$), which was verified by spectroscopic observations obtained by Heber, Reid, & Werner (1999).
- We found two other modes in the temporal spectrum match Kawaler's (1999) model, raising the total of modes fit by the model to seven.

Our $O-C$ analysis of PG 1605 revealed that:

- PG 1605 does not have pulsations stable enough in phase to perform a $\dot{P}$ measurement.

Feige 48

We applied *pattern matching techniques* to our large data set on Feige 48 and found that:

- Koen's (1998b) discovery data did not fully resolve the temporal spectrum; his period identifications for two pulsations were off by a daily alias.
- When properly identified in our larger data set, there are two modes separated by $\sim 13\mu$Hz and three separated by $\sim 27\mu$Hz; suggesting rotationally split modes.

- We calculated a standard sdB model that matched the observed pulsations to better than 0.2 seconds for all but the lowest amplitude mode. The best model has M=0.4725$M_\odot$ of which 0.0025$M_\odot$ is the hydrogen envelope, T_{eff}=29635, and log g=5.518.
- Our model matches the observed T_{eff} and log g well within 1 σ of the spectroscopic uncertainties.
- The frequency splitting implies a rotation period of ~10 hours, which is within the spectroscopic constraints of Heber, Reid, & Werner (2000) for inclinations less than 12°.
- This is the best sdBV model fit to date.

Temporal analysis of the phases of pulsation for Feige 48 revealed that:

- The phases of the pulsations in Feige 48 are stable over the timescale of our data (2.5 years).
- We determined an initial $|\dot{P}/P|$ for Feige 48 of $< 5.3 \times 10^{-16}\, s^{-1}$, giving an evolutionary timescale $> 3.1 \times 10^7$ years.
- Our $O - C$ analysis for Feige 48 is consistent with the our best fit evolutionary model in terms of rate of period change.
- We placed strict limits on any companions to Feige 48, including planets, and concluded that to within these limits, Feige 48 is not a binary.

PG 1336

With two full WET campaigns on PG 1336, we found over fifteen well established pulsation periods. In this temporal spectrum we found that:

- With such a crowded temporal spectrum, we attempted a model fit to the three largest amplitude variations; two of which are split by nearly twice the orbital frequency (a possible triplet with a missing central peak). However the model was not a realistic fit.

- The only model fit that could be obtained was near the 1σ limits of uncertainty in T_{eff} and log g and included pulsation modes that are geometrically unfavored at the known inclination (81°) of PG 1336.
- We deduced that PG 1336 has a complex temporal spectrum that requires additional parameters to explain, such as periodic variations in the projected pulsation axis.

Our $O - C$ analysis of PG 1336 indicates that:

- The periods in PG 1336 are stable over the two years between our WET campaigns.

We were also able to apply new tools of asteroseismology (developed in Chapter 8) to a preliminary reduction of PG 1336 Xcov 21 data to find that:

- Eclipse observations are not what would be expected for a pulsation axis aligned with the rotation axis.
- One mode (5483μHz) provides strong evidence for a pulsation axis that points toward its companion.
- A second mode (5254μHz) that adds evidence for the "tipped" pulsation model, but is not as secure as the 5483μHz mode.

Group Analysis

The third tool of asteroseismology we applied to the first 13 sdBV stars discovered. Our *ensemble analysis* determined that log g (as expected) has a much larger effect on sdBV stars than does T_{eff}. With this knowledge, we removed the log g dependence of the pulsation periods and compared the temporal spectra of the 13 sdBV stars. From this analysis we determined that:

- No obvious groupings of scaled periods appeared in the combined temporal spectrum.
- The uncertainty in log g (the largest contribution of which comes from atmospheric models) is large enough to mask underlying groupings within the range of log g encompassed by sdBV stars.

- At least one additional parameter (perhaps age or composition) needs to be accounted for before we can fully understand the pulsation periods in the majority of the class.
- Subdwarf B stars are not as homogeneous a group as the DAV stars, for which ensemble analysis was successful (Clemens, 1994b).

9.1.3 Developing New Tools

At this point in our work, we had exhausted the applicable set of asteroseismological tools. Our first thought was to determine what effects binarity could have on pulsations. We examined the Doppler effect, and realized that unless the binary was of long period, and with a fairly massive companion (to provide sufficient velocity), no appreciable Doppler shift would be observed. We also realized that as a star moves about its orbit, its distance from the observer varies with time. This change in distance means a periodic variation of arrival time of the light signals the star is sending (and we are receiving as pulsations). It is analogous to adding a periodic variation in the phase of pulsation.

We simulated data over a grid of orbital separations and companion masses provided by Ron Taam (private communication) appropriate for common envelope binaries that ended up producing an sdB star. Temporal spectra of the simulations did indeed show that for certain separations and companion masses, observed under usual conditions, extra peaks appeared in the temporal spectrum at multiples of the orbital frequency. Certainly if the star was not known to be in a binary, these would *appear* as rotationally split multiplets, which could lead to an incorrect ℓ identification. Thus we devised a simple scheme for correcting the pulsation phase due to light travel time across an orbit. If not known by other means (i.e. from radial velocity variations), the difficult part is determining the orbital parameters for the correction process.

The second new tool we used in our analysis involves the changing surface visibility offered by a partial eclipse. We simulated the primary eclipse for PG 1336 (where slightly more than half the sdBV star is covered at maximum primary eclipse) and discovered that modes not detectable outside of eclipse (due to the 81° inclination) are observable during eclipse. Modes

that can be seen outside of eclipse are generally also observable during eclipse. This becomes a wonderful new tool for asteroseismology that can uniquely identify pulsation modes in eclipsing systems.

Assuming the rotation axis is aligned with the orbital axis, and that the stars are tidally locked (this is normal for short period eclipsing binaries), the rotation period is known if the orbital period is known. This means that we know where to look in the temporal spectrum for rotational splittings. New peaks should appear in the eclipse temporal spectrum at integer orbital frequency spacings away from modes detected both during and out of eclipse. The appearance of the new modes should allow unique mode identifications to be made. We applied this to PG 1336. However, PG 1336 did not follow the predicted pattern.

This led us to the third new approach; working with close binaries. If the tidal force caused by the companion is stronger than the Coriolis force, then the pulsations axis is likely to point toward the companion. For PG 1336, this tips the pulsation axis nearly 90° compared to the rotation axis. As the pulsation axis follows the secondary around the orbit, our viewing angle changes. By changing the viewing angle, observability of some modes of pulsation changes. Certain modes experience cancellation when viewed from the pulsation poles, while others suffer cancellation effects when viewed from the pulsation equator. Also, nonradial modes will have phase changes during each orbital cycle, the number of which depends on the mode. There are three characteristics of a tipped pulsation axis, the combination of which can give us the identity of the mode of pulsation. They are: the peaks that appear in the combined temporal spectrum, peaks that appear when the data is separated into regions of like phase, and 180^o changes in pulsation phase around the orbit.

Though our PG 1336 data will take some time to fully reduce and analyze, we were able to perform at least one test with this method. We split the data into regions of like phase appropriate for an ℓ=1, $m = \pm 1$ mode and analyzed the temporal spectra. We detected two possible ℓ=1, $m = \pm 1$ modes, one of which fit all three of the characteristics, and another that only fit two of the characteristics of a tipped pulsation axis. Though preliminary, this result provides reasonable evidence to believe that the pulsation axis of PG 1336 is aligned with the

tidal force raised by the companion.

9.2 Ramifications of this Work

Our study of these four stars (and sdBV stars as an ensemble), relying on standard stellar models and asteroseismology tools, has produced some new results and revealed wide gaps in our understanding of these stars. The successes involve "standard" sdB models with model periods that match observation, indications of rotational splitting, and mode identifications. On the other hand, some objects show pulsations that are not fit with standard pulsation theory, with dense pulsation spectra where the models have few modes. With this work, the initial exuberance that accompanied the discovery of these stars now yields to the recognition that they are more complicated than we expected.

In Chapter 5, we calculated a model fit for Feige 48. This is only the *second* time a model fit has been made for an sdBV star that has succeeded without appealing to higher ℓ modes. This was possible despite our use of mostly single site data. No multiple site data were required to determine the pulsation periods (though some was acquired later on which nicely confirmed our determined periods). This tells us that although many sdBV stars may not show the anticipated signatures of p-mode pulsation, some will and that single-site data can be useful. As we observe more and more sdBV stars, some, at least, will be matched by standard models Using these stars, we may be able to then begin to understand the ones that do not show expected behavior.

Another important aspect of our model match on Feige 48 is that it tells us that the models contain appropriate physics to describe sdB stars. As more pulsation modes are identified in other stars and evolutionary models created to fit them, a detailed picture will be built up of the interior of at least some sdB stars. This is aligned with the original goal when this thesis work began.

In Chapter 6, we showed that an sdBV star (again Feige 48) has stable pulsation phases and amplitudes, yet is removed enough from the ZAEHB that only a few additional seasons of observations will be required to constrain its evolutionary timescale In fact, our work already

provides a constraint that says that Feige 48 is not evolving at some wild pace (which would produce a very different $\dot{P}$), but is consistent with what models tell us it should be. In just a few more years, measuring $\dot{P}$ in Feige 48 will place useful limits on helium fusion reactions, which control the rate of evolution of this star. We also determined that two modes in PB 8783 appear to have stable phases (at least over the limited timescale that we have data for). Though the predicted timescale for change is much longer for PB 8783 than for Feige 48, eventually we may measure $\dot{P}$s for it and other "young" sdBV stars, to compare with that measured in Feige 48.

In Chapter 7, we noted that pulsation periods scale with log g in sdBV stars. However, when we scaled by log g and aligned the temporal spectra of various group members, we did not find any groupings of pulsation periods (as was done for the hot DAV stars by Clemens, 1994). This lack of groupings could result from the uncertainties in log g and/or extra parameters (such as age or composition) that affect the periods. For spectroscopists, this is a signal that we need to focus on examining the atmospheres of sdB stars for new clues about their metallicity characteristics. If indeed composition is relevant, then spectroscopy will be a vital clue.

In Chapters 3 and 8, we developed new tools for use in asteroseismology. Though some of these tools were developed for a special case (PG 1336), they are completely general and can be applied to a variety of pulsating components of binary stars. This may be of special importance since it is believed that a significant fraction (probably 40% or more) of sdB stars are in close binaries.

Perhaps the most unanticipated contribution is the third new tool we provided for asteroseismology: the analysis of pulsation when the pulsation axis aligns with the tidal axis. Not only is this tool useful for sdBV stars (for which a substantial fraction are in short period binaries), but for cataclysmic variables (a white dwarf with a red giant companion) and any other variable star in a close binary (i.e. Fitch & Wisniewski, 1979). This tool is not only a good indicator of whether the pulsation axis is tipped, but can uniquely identify the pulsation mode for nonradial pulsations.

9.3 Where to go for answers

Even in conclusion, we wish to continue striving toward our initial goal, the understanding of the interiors of sdB stars. There are several lines of work that are striving toward this goal, but most of them involve one solution: *Observe more!*

In six years, over 20 sdBV stars have been discovered. Only a handful of these have received follow-up observations sufficient to resolve the temporal spectrum. Of these, 3 have yielded positive results (PG 1605, Feige 48, and PG 1336). Those stars that remain unproductive are telling us something important: that the pulsations we see are *not* normal nonradial oscillation modes of standard sdB stars as we imagine them. Either new modes are present, or the interiors of these stars are not what we expect. Through detailed spectroscopic work, population studies, time-resolved spectroscopy, or other ways, we need to develop better models for these pulsations.

New and unique methods may also be used to try to identify pulsation modes. Examining short period binaries is one obvious method that has just been developed in this thesis, yet is applicable to other stars. KPD 1930+2752 is an sdBV star in a 2.1 hour orbit with a massive white dwarf (Maxted, Marsh, & North, 2000). If any sdBV star is going to have a tipped pulsation axis, KPD 1930+2752 will. This prediction should be tested.

Other new tools being developed involve time resolved spectroscopy to study the pulsations as radial velocity variations in absorption lines (O'Toole *et al.*, 2000). By observing the pulsations in velocity rather than brightness, different modes may be preferentially observed. Such information may be used in conjunction with photometric data to understand the pulsation spectrum (a combined spectroscopic and photometric multisite campaign on PG 1605 will take place in May, 2002)

Normal nonradial pulsation theory can make definite predictions about the relative phases and amplitudes of p- and g-modes that those observations can test. Results from this combined spectroscopy and photometry campaign should be very instructive, as earlier work in this area (O'Toole *et al.*, 2000) shows that radial velocity measurements of pulsations can compliment photometry.

Another recent innovation that was developed for white dwarf stars (Kepler *et al.* 2000b; Clemens, van Kerkwijk, & Wu 2000) is comparing pulsation amplitudes in various wavelengths-especially UV. Just as eclipses change the observed surface geometry, so can limb darkening which increases at shorter wavelengths. By comparing UV variations to optical variations, it is theoretically possible to identify pulsation modes (Kepler, Robinson & Nather, 1995). This method preferentially works on hot stars, meaning that sdBV stars should be excellent subjects for such study.

Finally, observed pulsation periods have been in the range of a few minutes, where (for most stars) p-modes are relevant. Models by Charpinet, Fontaine, & Brassard (1996), suggested that g-modes, with much longer periods (hours) may also be present. These could be high-order g modes, which, if found open another window into the interior of sdB stars.

9.4 Conclusion

Studies of sdB stars represent a rapidly progressing field in stellar astronomy. Through sdB stars, we may hope to constrain nuclear physics by understanding helium fusion. We may obtain a better understanding of other horizontal branch stars, such as RR Lyrae stars, which are used as standard candles. Such an understanding will filter down through stellar evolution in an increased understanding of giant branch and white dwarf stars. Subdwarf B stars themselves will place constraints on white dwarf evolution as they will evolve to a distinctly lower mass white dwarfs than average.

Subdwarf B star observations will be used to constrain models on such issues as binarity and helium fusion rates from $O-C$ analysis, semiconvection, radiative levitation and gravitational settling by constraining composition changes through mode trapping and excitation effects. This knowledge may then renew interest in studies of opacities, mass transfer and Roche lobe overflow. Such work will benefit the astronomical community as whole.

From being one of the least understood type of stars, to the most observed in the PG and EC surveys, to the discovery of pulsations, and preliminary speculation on their evolution, sdB studies have blossomed.

APPENDIX A. SEARCHING FOR COMPANIONS TO SUBDWARF B STARS USING INFRARED COLORS

One currently popular scenario for producing sdB stars is through mass exchange in a binary system (Sandquist, Taam, & Burkert, 2000). In such a case, the sdB star is able to shed its outer envelope of hydrogen, leaving just a thin layer surrounding the helium core; as is observed. Binarity can also strongly affect not only the way we analyze the pulsations (see Chapters 2 and 3), but the pulsations themselves (see Chapter 8).

In this Appendix, we outline work that we did to determine the fraction of sdB stars with main sequence companions. We briefly outline the advantages of the infrared excess method of detection and review previous work in the literature. Next we use models to determine the range of main sequence companions to which this method is sensitive and then present the study itself.

Using Infrared Photometry to Detect Companions

Perhaps the easiest method for detecting late-type main sequence companions to sdB stars is in infrared wavelengths. Cool companions can be detected in the infrared that are too faint to be detected as members of composite spectrum binaries in optical wavelengths. Binaries can also be detected in the infrared where the binary period is long, or the orbital inclination low, making them difficult to detect via radial velocity variations. Another benefit is that they can be detected by a single set of photometric measurements (through multiple filters, of course). Radial velocity binaries require repeated observations from large (two to six meter) telescopes.

This method does have a drawback. Since $L \propto T^4$, the energy output of the sdB star, at >30 000 K, far outshines the cooler (few thousand Kelvin) companion at many wavelengths.

Fortunately significant portions of this energy are emitted in the UV or blue wavelength regions, so we are only observing the tail of the Plank function at infrared wavelengths. This can be used to some advantage: by comparing infrared magnitudes with at least one blue magnitude (in this case we use the Harris B filter bandpass), the color excess from red companions can be maximized.

A Review of Previous Studies

In 1994, Ulla & Thejll (1998 and references therein) began an IR search for companions to sdB stars. They selected sdB stars from the survey of Kilkenny *et al.* (1988), some of which were previously known to have a companion. After observing 88 subdwarf stars in J, H & K filters, they report that 39 stars (or 44%) have MS companions including spectral types from A to early M. They claim their sample (within Kilkenny *et al.*, 1988) is complete to $K = 13.5$. This result is in agreement with the derived binary fraction of Ferguson, Green & Liebert (1984), but not with Maxted, Marsh, & North (2000).

To provide additional constraints, Jeffery & Pollacco (1998) obtained medium resolution infrared spectra of 40 sdB stars selected from the work of Ferguson, Green, & Liebert (1984) and Allard *et al.* (1994). Several stars in their sample have previously been indicated as binaries. They report detection of Ca T absorption lines in 7 systems, all of which also showed an IR excess in other surveys. Unfortunately, their spectra are of too low a resolution to distinguish the binary properties. They claim that using Ca T line measurements (from medium resolution infrared spectroscopy) is the "only likely means of detecting (MS) M-type companions..." . Their 7 detections (from a sample where the majority of the stars are previously *known* to have companions), represent the smallest fraction of binary sdB stars (18%) of any work to date.

Model Colors

Before we examine observational data, we want to determine what spectral range of MS companions should be visible through infrared color excess. Using Kurucz (1993) models[1] we

[1]Obtained via FTP from stsci.edu.

synthesized magnitudes using the method from Reed, Kawaler & O'Brien (2000) and summarized as follows: We selected sdB models from the Kurucz grid with $\log g = 5.0$ and ranging in $T_{\rm eff}$ from 25 000 K to 45 000 K. We also selected main sequence models for spectral types[2] ranging from A0 through M5. We then convolved the Kurucz model spectra with the 2MASS filter bandpasses[3] and Harris B filter, linearly interpolating the flux between wavelength points, to produce synthesized integrated fluxes. After multiplying by appropriate stellar surface area[4], we convert the fluxes to magnitudes, using filter zero points from Bessell and Brett (1988).

Figures A.1 and A.2 show color-color diagrams for the results of Kurucz models convolved with 2MASS J, H, or K_s or Harris B filter bandpasses. The green line is for single sdB stars ranging from 25,000 to 45,000K, the red line is for Kurucz MS models, the black line is for Bessell & Brett (1988) magnitudes for single MS stars ranging from A0 to M5 (B magnitudes from Lange, 1991), and the magenta line is for a convolution of a 35 000K sdB star with MS companions varying from A0 to M5. Note that points on a color-color diagram are ratios of fluxes. As such, we do not expect to be able to add up two lines to make a third (i.e. the sdB+MS line is not the sum of the MS and sdB lines). As indicated in the figures the Kurucz models are quite good for the early MS, but depart from the Bessel & Brett (1988) colors for later MS types; especially for the M dwarfs. This mismatch presents only a small concern as M dwarfs do not emit enough flux in the infrared to change the infrared colors of sdB stars.

As expected, the single sdB stars inhabit a small area in blue colors while MS stars spread across the figure. The sdB+MS combinations for early main sequence stars (A0 in this case) show up best in the $(J-K)$ - $(B-K)$ and $(J-H)$ - $(J-K)$ planes, with the largest separation between single sdB stars and combination sdB+MS is for a K5 companion. Subdwarf B stars with late M-type companions appear close to the single sdB stars, as expected. This will likely make them indistinguishable from single sdB stars in our analysis.

[2]As referenced at *http : //www.stsci.edu/instruments/observatory/cdbs/k93models.html*.
[3]The 2MASS filter bandpasses are provided at http://spider.ipac.caltech.edu/staff/waw/2mass/opt_cal/.
[4]Radii used are 0.15 $R_\odot$ for all the sdB stars, main sequence radii from Cox (2000).

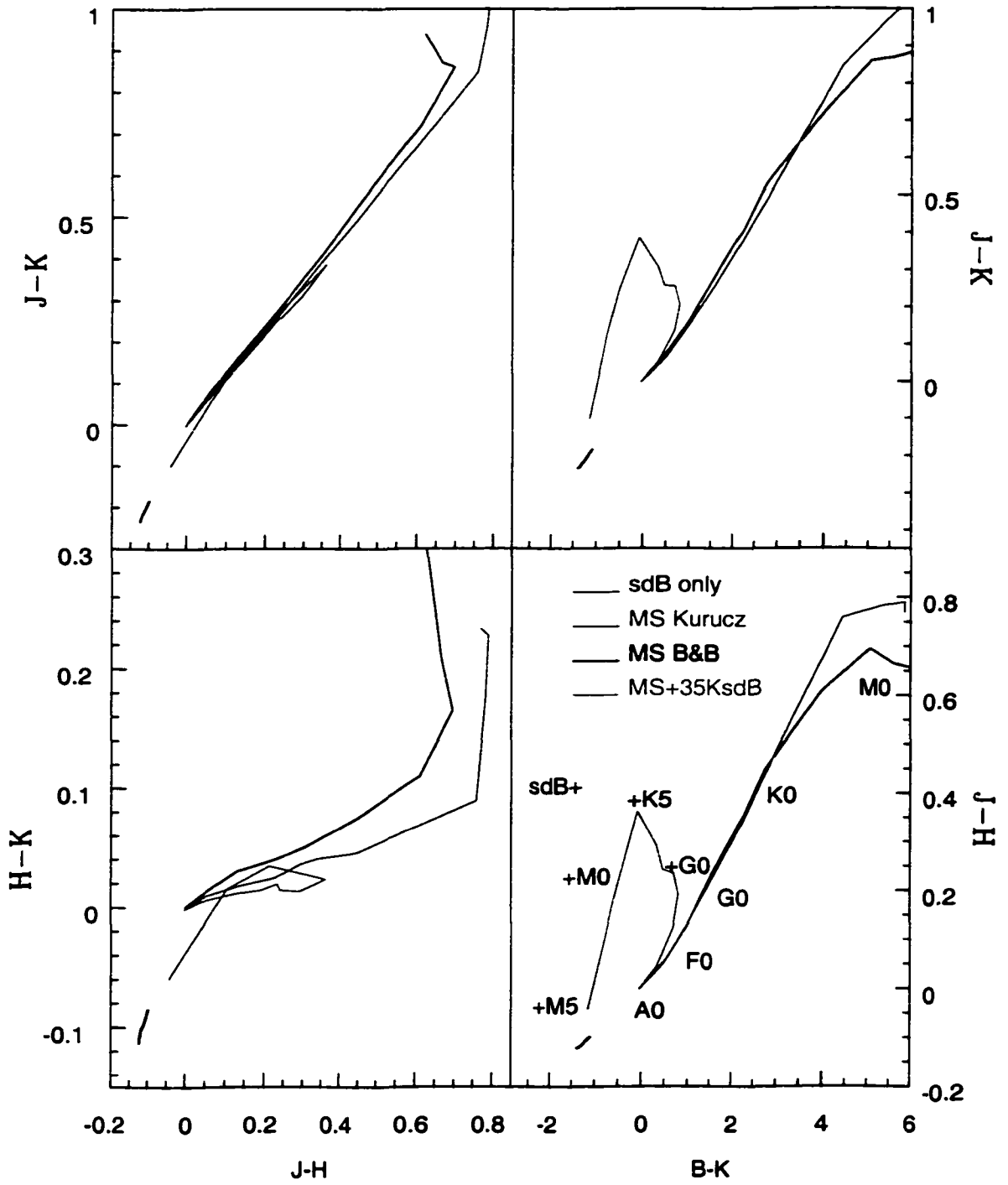

Figure A.1 Relative fluxes (in magnitudes) of Kurucz models convolved with various filter combinations.

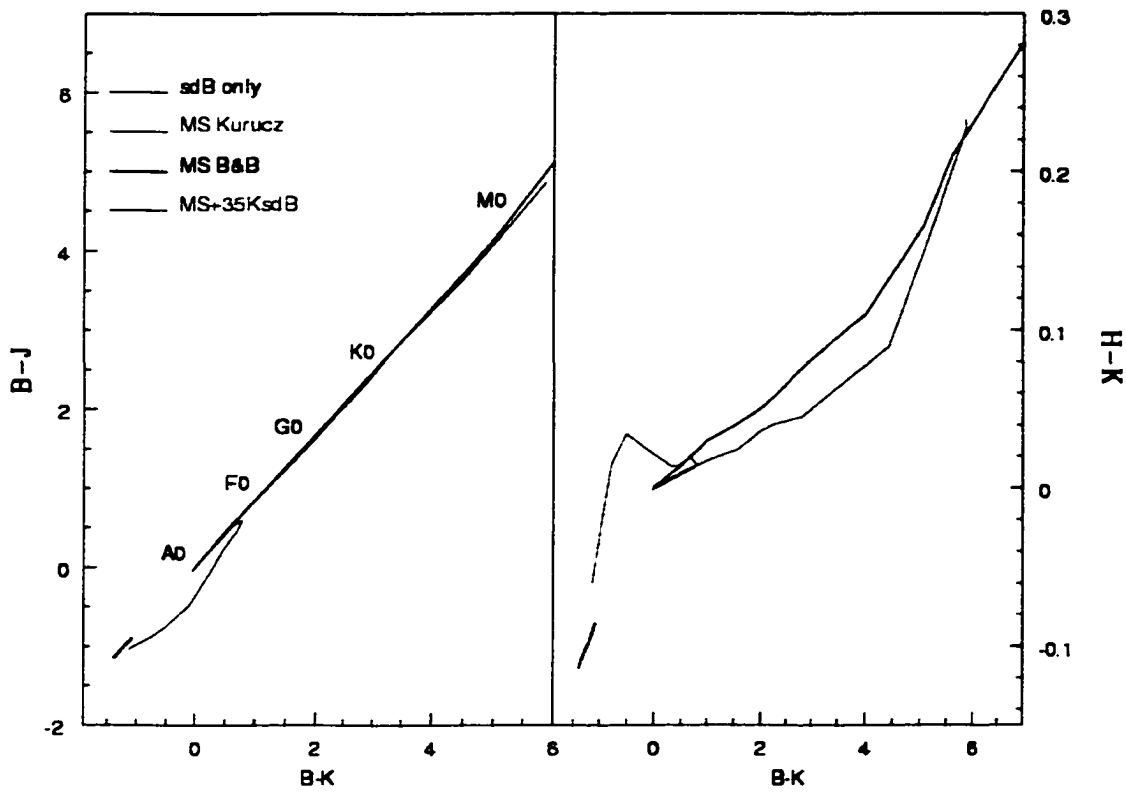

Figure A.2 Color-color diagrams of model results

2MASS results

Though sky surveys date back as far as the birth of astronomy (Hipparchus' creation of the magnitude system circa 150 B.C.), at no time in astronomical history has such a large volume of all-sky survey data been available to the astronomical community. One such survey (the EC survey) uncovered the first member of the class of pulsating stars examined in this thesis (Kilkenny *et al*, 1997a). Newly released data from another survey provides a different way to answer the question posed by this Appendix: how many sdB stars are in binaries?

The *Two Micron All Sky Survey* (2MASS) has completed its mission of covering the entire sky in J, H, and K_s bands. As of the Second Incremental Release (March, 2000), 47% of the sky is currently available, though we were able to access the *entire* survey[5]. We wish to obtain

[5]Thanks to Rae Steining at University of Massachusetts, Amherst.

J, H, and K_s magnitudes for *every* sdB star available (the sample is magnitude limited at ~16.5). The goal is to create color-color diagrams that effectively identifies companions to sdB stars earlier than main sequence M stars.

The 2MASS survey is a single-epoch all-sky survey in the J, H, and K_s bands with a limiting magnitudes ~16.5. Availability of targets and observed magnitudes are retrieved via a web-based form[6] which allows user input coordinates or object name. The positional accuracy of the survey is < 0.2" (Cutri *et al.*, 2000) and Groenewegen (2000) determined that the absolute photometric calibration is < 0.02 magnitudes. Bright (saturated) sources were removed and upper limits are noted as such.

We created 2MASS coordinate lists for *every* sdB star available from the EC (Kilkenny *et al.* 1998)(259 stars), PG (Green, Schmidt, & Liebert 1986)(569 stars), HS (Heber 2000, *private communication*) (119 stars), and KPD (Downes 1984)(42 stars) surveys as well as a few Feige and BD stars (from Ulla & Thejll, 1998 and references therein). To date we have retrieved 1282 2MASS observations (a small number of which are multiple observations of stars and some stars are included in multiple surveys) and are currently culling the observations for accurate magnitudes. So far we have examined the observations from the northern hemisphere for 338 stars with an absolute error on the photometry (rather than upper limits) in all filters. We have an additional 154 stars in the southern hemisphere from the EC survey, for a total of 492 stars.

Table A.1 compares our results with published infrared observations from Ulla & Thejll (1998) for stars common to both. The two samples are consistent within the errors, though it is obvious that the 2MASS magnitudes are larger, implying a small systematic offset. There are also a few cases where the 2MASS magnitudes are systematically different in all bands for a star (Feige 108, PB 8555, and PG 0856+121). We have no explanation for this discrepancy. However, the 2MASS magnitudes have consistently smaller uncertainties than Ulla & Thejll (1998) and considering the uniformity of the 2MASS images and reductions techniques, we have confidence in conclusions based exclusively on the 2MASS results.

[6]The 2MASS web address is http://www.ipac.caltech.edu/2mass/index.html.

Table A.1 Comparison of magnitudes for sdB stars from 2MASS with Ulla & Thejll (1998: UT98). Photometric errors in parenthesis. Difference from published values are (this work)-(UT98).

Star	J	H	K_s	ΔJ	ΔH	ΔK
BD-3 5357	7.356(0.014)	6.786(0.024)	6.604(0.010)	0.076	0.046	0.014
BD-7 5977	9.017(0.021)	8.526(0.043)	8.448(0.029)	0.047	0.046	0.068
BD-11 162	10.882(0.027)	10.696(0.027)	10.595(0.027)	0.072	0.056	-0.0 15
Feige 34	11.645(0.031)	11.550(0.027)	11.537(0.036)	.041	.045	.048
Feige 65	12.630(0.034)	12.716(0.032)	12.837(0.040)	0.150	0.066	0.147
Feige 80	11.101(0.029)	10.870(0.053)	10.826(0.033)	.06	.062	.044
Feige 108	13.871(0.024)	13.396(0.031)	13.371(0.045)	0.241	0.386	0.491
HD 21635	10.385(0.021)	10.437(0.026)	10.500(0.025)	0.095	0.027	0.040
KPD 2109+4401	13.653(0.024)	13.289(0.034)	13.257(0.040)	.042	.052	.047
PB8555	11.843(0.025)	11.722(0.036)	11.684(0.027)	0.543	0.652	0.744
PG 0215+183	13.664(0.032)	13.711(0.040)	13.751(0.052)	0.164	0.006	-0.369
PG 0242+132	13.482(0.027)	13.628(0.033)	13.614(0.045)	-0.038	0.148	0.144
PG 0856+121	13.931(0.038)	14.034(0.050)	14.137(0.076)	0.512	0.444	0.297
PG 1219	13.926(0.030)	14.023(0.044)	14.089(0.072)	.053	.084	.078
PG 1338+481	14.174(0.034)	14.208(0.050)	14.305(0.092)	.06	.105	.098
PG 2118+126	13.040(0.025)	12.836(0.032)	12.800(0.029)	.041	.043	.038

Figure A.3 shows our color-color diagram for observed sdB stars plotted over the model results from Figures A.1 and A.2. Though there are many interlopers, the sdB stars divide into two 'clumps'. The bluer 'clump' lies directly over the model results for single sdB stars and are most likely sdB stars which either do not have a main sequence companion or have one that is extremely faint and red. The second 'clump' extends along the model results for sdB+MS stars. To determine if the two 'clumps' are meaningful, we examined sdB stars in known or suspected binaries from other techniques in the literature.

Table A.2 lists the previously known binary sdB stars, which are plotted in Figure A.4. In all but one case, the stars in the bluer 'clump' are those with white dwarf companions, which should appear like single sdB stars (since white dwarfs have $\sim 0.1 R_{sdB}$ or $\sim 0.01 L_{sdB}$ and contribute little flux in either filter). All the stars (again, except for one) that have MS companions (other than M-type) are in the redder 'clump'. The only sdB+MS star that is in the blue group has a designation by Ulla & Thejll (1998) of "very early", which means it is bluer than A0. The M-type companions give ambiguous results with two appearing slightly too

blue and two that are significantly reddened. However, the plot confirms that the red 'clump' is almost certainly sdB stars which have a main sequence companion between A0 and K5.

We also note that the $(J-H)$-$(J-K)$ index separates the two cases somewhat better than the others. At this stage, this may be due to inaccurate B magnitudes from IPAC (via the web form). In the future, the B magnitudes will have to be retrieved from the individual surveys and compared to those from IPAC, which we already know can vary from the survey work by at least a magnitude. To make full use of the 2MASS survey we still need to cull the results for 2MASS magnitudes that only provide an upper limit in at least one filter. For the majority of these, the J and H filters have limits, with only the K_s filter having an upper limit. This will nearly double the number of stars in Figure A.3.

Our preliminary results indicate that 40% ±4 of the sdB stars in our data set have main sequence companions between A0 and M0. This result is very similar to that of Ulla & Thejll (1998), and the predicted number of main sequence companions by Ferguson, Green, & Liebert (1984), but nearly twice that observed by Maxted, Marsh, & North (2000).

Conclusions

In this appendix, we convolved Kurucz (1993) model atmospheres appropriate for a range of sdB and main sequence stars with the 2MASS filter set. We used these model colors to determine that the infrared excess method is viable for finding companions to sdB stars for main sequence stars between A0 and ~M0.

We then obtained 2MASS magnitudes for *every* sdB available from the literature (near 1300 observations), from which we used a subset of 492 stars with strict limits on their errors. From this sample, we determined that 40±4% of sdB stars in our sample have a main sequence companion between A0 and M0. This is in agreement with the work of Ferguson, Green, & Liebert (1984) and Ulla & Thejll (1998), though our sample is by far the largest; nearly an order of magnitude larger than that of Ulla & Thejll (1998).

Radial velocity studies have inferred that 45% (Green, Liebert, & Saffer, 2000; where *no* inclination effects have been accounted for) to at least 60% (Maxted, Marsh, & North, 2000) of

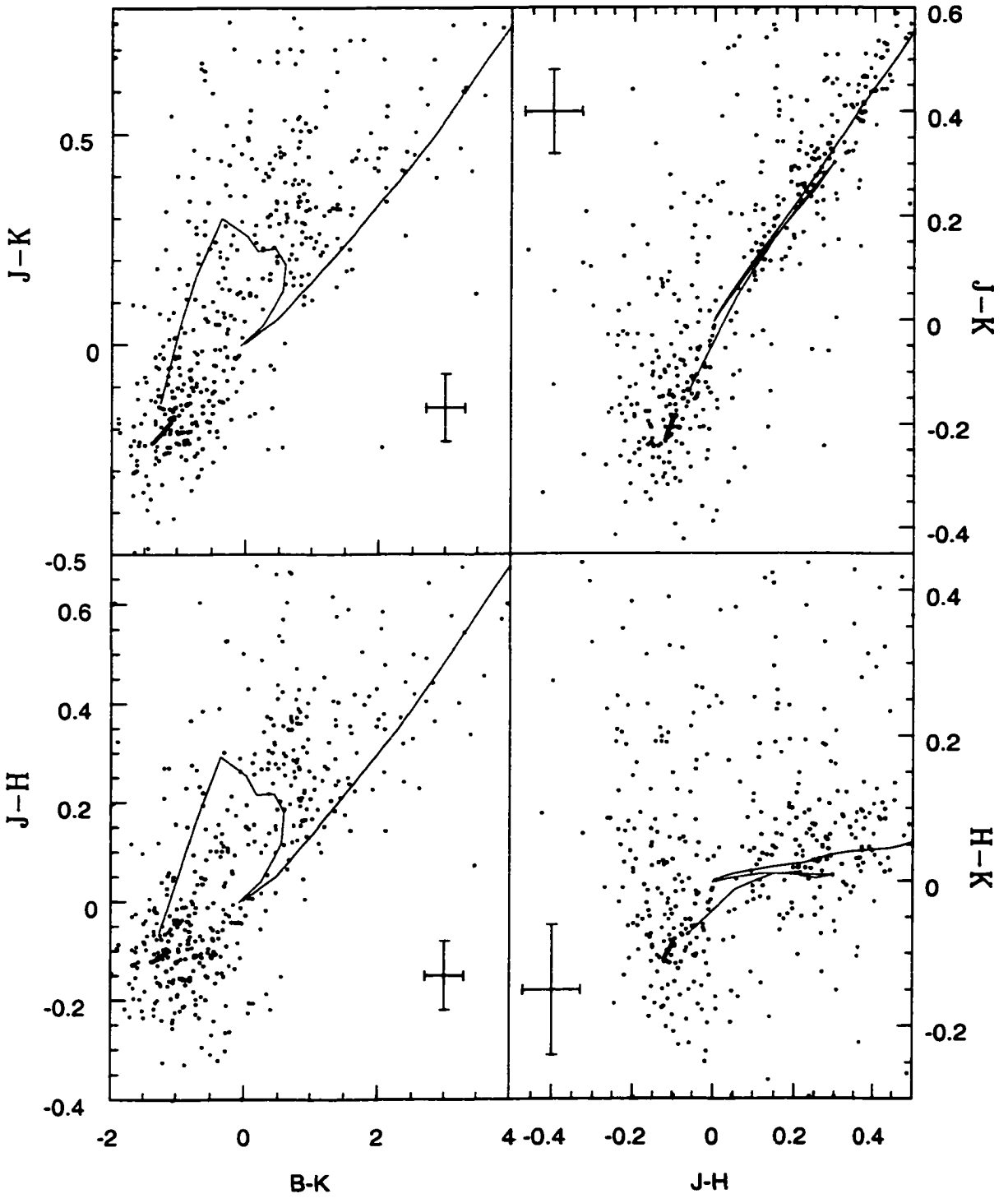

Figure A.3 Color-color diagrams of stars from 2MASS plotted over model results. Errorbars denote the most likely error.

Table A.2 A list of known or suspected sdB stars in binaries.

No.	Name	Companion	Type	Source
1	BD-3 5357	K3	Infrared Photometry	6
2	BD-7 5977	K1-2	Infrared Photometry	6
3	BD-11 162	F4-G0	Infrared Photometry	6
4	EC 10228-0905	G0	Composite Spectrum Binary	5
5	Feige 34	K3+	Infrared Photometry	6
6	HD 21635	ve	Infrared Photometry	6
7	KPD 1930+2752	WD	Spectroscopic Binary	2
8	PB 8555	F8-G1	Infrared Photometry	6
9	PB 8783	F3	Composite Spectrum Binary	5
10	PG 0101+039	WD	Spectroscopic Binary	3
11	PG 0110+262	~G9	Multi-color Photometry	1
12	PG 0856+121	~M1	Multi-color Photometry	1
13	PG 1040+234	K3.5	Composite Spectrum Binary	3
14	PG 1049+013	K4	Multi-color Photometry	1
15	PG 1432+159	WD	Spectroscopic Binary	3
16	PG 1629+081	~M0	Multi-color Photometry	1
17	PG 1631+267	G	Composite Spectrum Binary	3
18	PG 1647+056	K8	Composite Spectrum Binary	3
19	PG 1701+359	K6.5	Composite Spectrum Binary	3
20	PG 1718+519	~G0	Multi-color Photometry	1
21	PG 2118+126	F3+	Infrared Photometry	6
22	PG 2135+045	~K5	Multi-color Photometry	1
23	PG 2226+094	~M0	Multi-color Photometry	1
24	PG 2345+318	WD	Eclipsing Binary	3

1) Aznar Cuadrado & Jeffery, 2001 A&A, 368, 994: Type inferred from $T_{\rm eff}$ only.
2) Maxted *et al.*, 2000, MNRAS, 317, 41
3) Maxted *et al.* 2001, MNRAS, *in press*
4) O'Donoghue *et al.* 1998, MNRAS, 296, 296
5) O'Donoghue *et al.* 1999, ASP Conf. Ser.
6) Ulla & Thejll, 1998, A&A Supp. 132, 1: ve=earlier than Bessel & Brett table (1988)

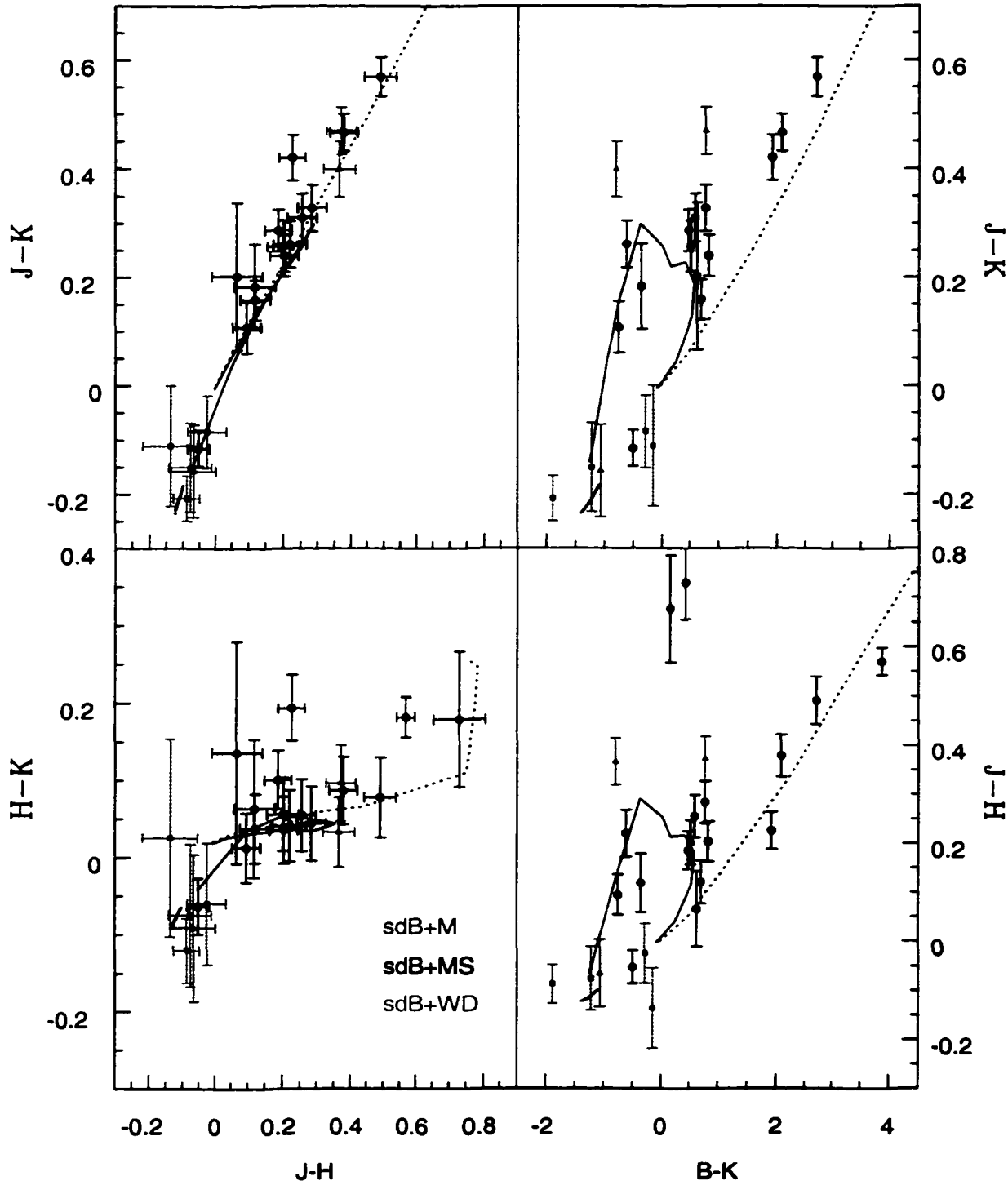

Figure A.4 Color-color diagrams of stars in known or suspected binaries

sdB stars are in short period binaries ($P_{orb} \leq 10$ days). Nearly all of the short period binaries show no indication of their companion (inferring that the companion is a white dwarf or main sequence star later than ~M0). Radial velocity work also indicates that an additional 20% of sdB stars are long period binaries with MS companions (Green, Liebert, & Saffer, 2000).

Combining the spectroscopic binary results with those from our work indicates that 85 to 100% of all sdB stars are in binaries. With such a large percentage of sdB stars in binaries, even a casual observer would have to conclude that it is a *requirement* for producing them. However, we expect that a small percent of sdB stars should be single as they could have formed from mergers of low mass white dwarfs (maybe 5%; Iben & Tutokov, 1986b). It is also interesting to note that thus far, there have been *no* observations of main sequence pairs in close binaries for main sequence stars earlier than M5. This almost certainly speaks to how sdB stars are formed from red giant stars and seems to confirm the hypothesis of Green, Liebert, & Saffer (2000).

BIBLIOGRAPHY

[1] Allard, F., Wesemael, F., Fontaine, G., Bergeron, P., and Lamontagne, R. 1994, *AJ, 107*, 1565

[2] Aznar Cuadrado, R., Jeffery, C. S. 2001, *A&A, 368*, 994

[3] Baldry, I.K., Kurtz, D.W., and Bedding, T.R. 1998, *MNRAS, 300*, 39

[4] Berger J., Fringant A.-M., 1984, *A&As, 58*, 565

[5] Bessell, M.S., and Brett, J.M. 1988, *PASP, 100*, 1134

[6] Billéres, M., Fontaine, G., Brassard, P., Charpinet, S., Liebert, J., and Saffer, R.A. 2000, *ApJ, 530*, 441

[7] Bond, H. *et al.* 1996, *AJ, 112*, 2699.

[8] Böhm-Vitense, Erika 1991, *Introduction to Stellar Astrophysics*, (Cambridge: Cambridge University Press)

[9] Bradley, P.A., and Winget, D.E. 1994, *ApJ, 430*, 850

[10] Bradley, P.A. 1994. *PhD thesis*, Univ. Texas at Austin

[11] Brassard, P., Fontaine, G., Wesemael, F., Kawaler, S.D., & Tassoul, M. 1991, *ApJ 367*, 601

[12] Brown, Thomas M., Bowers, Charles W., Kimble, Randy A., Sweigart, Allen V., Ferguson, Henry C. 2000, *ApJ, 532*, 308

[13] Caloi, V. 1989, *A&A, 20,* 357

[14] Charpinet, S., Fontaine, G., and Brassard, P. 2001, *PASP, 113,* 775

[15] Charpinet S., Fontaine G., Brassard P., Dorman B., 1996, *ApJ, 471,* L103

[16] Christensen-Dalsgaard, J. & Dziembowski, W.A. 2000, in *Variable Stars as Essential Astrophysical Tools*, eds. C. Ibanoğlu, (Dordrecht: Kluwer Academic Press) p1

[17] Clayton, Donald. D. 1983, *Principles of Stellar Evolution and Nucleosynthesis* (Chicago: The University of Chicago Press.)

[18] Clemens, J.C., van Kerkwijk, M.H., & Wu, Y. 2000, *MNRAS, 314,* 200

[19] Clemens, J.C. 1994a, *PASP, 106,* 1322

[20] Clemens, J.C. 1994b, *PhD thesis*, Univ. Texas at Austin

[21] Cox, J.P. 1974, *Reports on Progress in Physics, vol. 37,* #5, 563

[22] Cox, J.P. 1980, *Theory of Stellar Pulsation*, (Princeton: Princeton Univ. Press)

[23] Cunha, Margarida, S. 2001, *MNRAS, 325,* 373

[24] Cutri R.M, *et al.* (the 2MASS team) 2000, *Explanatory Supplement to the 2MASS Second Incremental Data Release.*

[25] D'Cruz, N.L., Dorman, B., Rood, T., & O'Connell, R.W. 1996, *ApJ, 466,* 359

[26] Dehner, B.T & Kawaler, S.D. 1995, *ApJ, 445,* L141

[27] Dehner, B.T. 1996, *PhD thesis*, Iowa State University.

[28] Dorman, B., O'Connell, R.W., & Rood, R.T, 1995, *ApJ, 442,* 105

[29] Downes, R.A. 1986, *ApJS, 61,* 569

[30] Dziembowski, W 1977, *Acta Ast., Vol 27,* 203

[31] Feige, J. 1958, *ApJ., 128,* 267

[32] Ferguson, D.H., Green, R.F., & Liebert, J. 1984, *ApJ, 287*, 320

[33] Fitch, W.S. and Wisniewski, W.Z. 1979, *ApJ. 231*, 808

[34] Green, E.M., Liebert, J., & Saffer, R.A. 2000, *ASP Conf. Ser., Vol 226,* 192

[35] Green, R.F., Schmidt, M., & Liebert, J. 1986, *ApJS, 61*, 305

[36] Greenstein, Jesse L. 1966, *ApJ, 144*, 496

[37] Groenewegen, M.A.T. 2000, *LANL preprint: 0010298*

[38] Hansen, Carl J. & Kawaler, Steven D. 1994, *Stellar Interiors.* (New York: Springer-Verlag)

[39] Heber, U., Reid, I. N., & Werner, K. 1999, *A&A, 363*, 198

[40] Heber, U., Reid, I. N., & Werner, K. 1999, *A&A, 348*, 25

[41] Iben, I., Jr., & Tutokov, A.V. 1986a, *ApJ, 311*, 742

[42] Iben, I., Jr., & Tutokov, A.V. 1986b, *ApJ, 311*, 753

[45] Jeffery, C.S., & Pollacco, D.L. 2000, *MNRAS, 318*, 974

[44] Jeffery, C.S., & Pollacco, D.L. 1998, *MNRAS, 298*, 179

[45] Jeffery, C.S., & Pollacco, D.L. 2000, *MNRAS, 318*, 974

[46] Kawaler, S.D., Winget, D.E., and Hansen, C.J. 1985, *ApJ, 298*, 752

[47] Kawaler, S.D. & Weiss, P 1990, in *Progress of Seismology of the Sun and Stars*, eds. A.G.D. Philip, D.S. Hayes, & J. Liebert, (Schenectady: Davis) p297

[48] Kawaler, S.D., & Bradley, P.A. 1994, *ApJ, 427*, 415

[49] Kawaler, S.D. 1999, *ASP Conf. Ser., Vol 169,*

[50] Kepler, S.O., Mukadam, A., Winget, D.E., Nather, R.E., Metcalfe, T.S., Reed, M.D., Kawaler, S.D., and Bradley, P.A. 2000a, *ApJL, 534*, 185

[51] Kepler, S.O., Robinson, E.L., Koester, D., Clemens, J.C., Nather, R.E., and Jiang, X.J 2000b, *ApJ, 539*, 379

[52] Kepler, S.O., Robinson, E.L., & Nather, R.E. 1995, *BaltA, 4*, 302

[53] Kilkenny, D., Marang, F., Menzies, J.W. 1994, *MNRAS, 267*, 535

[54] Kilkenny, D., Koen, C., O'Donoghue, D., and Stobie, R.S. 1997a, *MNRAS, 285*, 640

[55] Kilkenny, D., O'Donoghue, D., Koen, C., Lynas-Gray, A.E., & van Wyk, F. 1998, *MNRAS, 296*, 329

[56] Kilkenny, D., O'Donoghue, D., Koen, C., Stobie, R.S., and Chen, A. 1997b, *MNRAS, 287*, 867

[57] Kilkenny, D., Koen, C., O'Donoghue, D, Wyk, F. Van, Larson, K. A., Shobbrook, R, Sullivan, D. J., Burleigh, M. R., Dobbie, P. D, and awaler, S. D. 1999, *MNRAS, 303*, 525

[58] Kilkenny, D., Heber, U., Drilling, J., 1988, *SAAO Circ. No. 12*, and later electronic versions therof distributed by the authors.

[59] Kleinman, S.J., *et al.* 1998, *ApJ, 495*, 424

[60] Kleinman, S.J., Nather, R. E., & Phillips, T 1996, *PASP, 108*, 356

[61] Koen, C., O'Donoghue, D., Kilkeny, D., Lynas-Gray, A.E., Marang, F., and vanWyk, F. 1998, *MNRAS, 296*, 317

[62] Koen, C., O'Donoghue, D., Pollacco, D. L., Nitta, A. 1998, *MNRAS, 300*, 1105

[63] Koen, C., Kilkenny, D., O'donoghue, D., Van Wyk, F., and Stobie, R.S. 1997, *MNRAS, 285*, 645

[64] Kurtz, D.W., *et al.* (the Xcov 20 team), 2001, *MNRAS, in press*

[65] Kurtz, D. W., Matthews, J. M., Martinez, P., Seeman, J., Cropper, M., Clemens, J. C., Kreidl, T. J., Sterken, C., Schneider, H., Weiss, W. W., Kawaler, S. D., and Kepler, S. O. 1989, *MNRAS, 240*, 881

[66] Kurucz, R. 1993, CD-ROM #13 available via FTP from stsci.edu

[67] Landsman, W, Bohlin, R. Neff, S.G., O'Connell, R.W., Morton, S.R., Smith, A.M., and Stecher, T.P. 1998, *A.J., 116*, 789

[68] Lange, K.R. 1991, *Astrophysical Data: Planets and Stars*, (New York: Springer-Verlag)

[69] Ledoux, P, and Walraven, Th. 1958, *Variable Stars*, (Berlin: Springer-Verlag)

[70] Liebert, J., Saffer, R.A., & Green, E.M. 1994, *AJ*, 107, 1408

[71] Maxted, P.F.L. 2000, *ASP Conf. Ser., Vol 226*, 187

[72] Maxted, P.F.L., Marsh, T.R., & North, R.C. 2000, *MNRAS, 317*, 41

[73] Moehler, S.; Sweigart, A. V.; Landsman, W. B.; Heber, U. 2000, *A&A*, 360, 120

[74] Nather, R.E., Winget, D.E., Clemens, J.C., Hansen, C.J., Hine B.P. 1990, *ApJ, 361*, 309

[75] O'Brien, M.S., Clemens, J.C., Kawaler, S.D., & Dehner, B.T. 1996, *ApJ, 467*, 397

[76] O'Brien, M.S. 1998, *PhD thesis*, Iowa State University

[77] O'Donoghue, D., *et al.* 1998, *MNRAS, 296*, 296

[78] O'Donoghue, D., Koen, C., Kilkenny, D., Stobie, R.S., Lynas-Gray, A.E. 1999, *ASP Conf. Ser., Vol. 169*,

[79] O'Toole S, *et al.* 2000, *ApJ, 537*, 530

[80] Reed, M.D., and Steining, R. 2001, *in preparation*

[81] Reed, M.D., *et al.* (the WET consortium) 2001, *in preparation*

[82] Reed, M.D., *et al.* (the WET consortium) 2000, *BaltA, 9*, 183

[83] Reed, M.D., Kawaler, S.D. & Kleinman, S.J 2000, *ASP Conf. Ser., Vol 203*, 503

[84] Reed, M.D., Kawaler, Steven, D., and O'Brien, M. Sean 2000, *ApJ, 545*, 429

[85] Robinson, E.L., Kepler, S.O. & Nather, R.E. 1982, *ApJ, 259*, 219

[86] Saffer, Rex A., Bergeron, P., Koester, D., and Liebert, James 1994, *ApJ, 432*, 351–366.

[87] Sandquist, E.L., Taam, R.E., and Burkert, A. 2000, *ApJ, 533*, 984

[88] Smeyers, P., and Tassoul, M 1987, *ApJ, 65*, 429

[89] Thompson, Ian B., Kaluzny, Janusz, Pych, Wojtek, Krzeminski, Wojtek 1999, *AJ, 118*, 462

[90] Ulla, A., and Thejll, P. 1998, *A&AS, 132*, 1

[91] Unno, W., Osaki, Y., Ando, H., Saio, H., and Shibahashi, H. 1989, *Nonradial Oscillations of Stars*. (Tokyo: University of Tokyo Press)

[92] Winget, D.E., *et al.* 1991, *ApJ, 378*, 326

[93] Yong, H. Demarque, P. and Yi, S. 2000, *ApJ, 539,* 928